Title

The Interplay of Structure, Magnetism and Superconductivity in CaRE112 and 10-3-8 Fe-Pnictide Superconducting Families

Author

Jiang, Shan

Publication Date

2017

Peer reviewed|Thesis/dissertation

UNIVERSITY OF CALIFORNIA

Los Angeles

The Interplay of Structure, Magnetism and Superconductivity in CaRE112 and 10-3-8 Fe-Pnictide Superconducting Families

A dissertation submitted in partial satisfaction
of the requirements for the degree
Doctor of Philosophy in Physics

by

Shan Jiang

2017

ABSTRACT OF THE DISSERTATION

The Interplay of Structure, Magnetism and Superconductivity in CaRE112 and 10-3-8 Fe-Pnictide Superconducting Families

by

Shan Jiang
Doctor of Philosophy in Physics
University of California, Los Angeles, 2017
Professor Ni Ni, Chair

Following the discovery of superconductivity in an Fe pnictide compound (LaFeAsO) in 2008, many other Fe-based superconductors were discovered with T_c as high as 56 K. Among them, the most extensive studies were carried out on the so called 122 system (AeFe$_2$As$_2$, Ae=Ba, Sr and Ca), because of the availability of large, high-quality single crystals. A recurring theme from these works is the rich interplay between antiferromagnetic and superconducting orders, and their relationship to structure and so-called electronic nematic instabilities. The research described here exploits two compounds with new and nontrivial crystal structures to open a new perspective on the important physics of the FBS.

Two newly discovered members of the FBS family, $Ca_{1-x}RE_xFeAs_2$ (CaRE112) and $Ca_{10}Pt_3As_8(Fe_2As_2)_5$ (10-3-8), possess intriguing structural characteristics and electronic band properties. As one of the most anisotropic FBSs, the critical temperature in the 10-3-8 family can be induced up to 35 K by appropriate doping/external pressure while the CaRE112 compound can be doped into superconductors up to 47 K. They possess nontrivial structural and chemical characteristics. Firstly, structurally, unlike the other intensively studied pnictides which crystalize in tetragonal structure, 10-3-8 crystallizes in a triclinic structure. However, the "magic" FeAs layer, which is proposed to play a crucial role in mediating superconductivity, still maintains the local C_4 rotational symmetry. On the other hand, CaRE112 has monoclinic structure at room temperature. However, owing to a unique

spacer layer consisting of zigzag As chains in the crystal structure, FeAs layer loses its local C_4 rotational symmetry even at room temperature, which is very unique in all FBSs. Secondly, the nature of the spacer layers in 10-3-8 and CaRE112 are quite different from each other. The 10-3-8 family has the skutterudite Pt_3As_8 layer as the spacer layer, which can be assigned with integer number of oxidization states, thus the spacer layer will not contribute density of states at the Fermi level. On the other hand, the CaRE112 family has the zigzag chains as its spacer layer, which can not be assigned with integer oxidization states and contributes significant amount of density of states at the Fermi level. The fact that these two systems have similar FeAs interlayer distance but quite distinct characteristics of their spacer layers make them great systems to study the effect of the interlayer coupling on competing orders in FBSs.

In this thesis, I present a systematic experimental study, from synthesis to characterization, for both materials. I make combined transport, thermodynamic, neutron scattering, and muon spin relaxation measurements to investigate the interplay of competing orders and elaborate the role of the interlayer coupling on these competing orders. It has been reported previously that $Ca_{10}Pt_3As_8(Fe_2As_2)_5$, the parent compound of the 10-3-8 family, shows structural/magnetic instabilities. By substituting Co on Fe sites in the 10-3-8 family, the structural/magnetic phase transitions are suppressed and superconductivity up to 13.5 K is stabilized in an extended dome-like region in the temperature–dopant concentration phase diagram. More importantly, we demonstrate that within our experimental resolution, no phase coexistence of antiferromagnetism and superconductivity exists in Co doped 10-3-8. Our research on the CaRE112 (RE = La, Ce, Pr, Nd) system is pioneering. Our refined synthesis recipes make us the first group to grow sizable CaRE112 single crystals with controlled doping. We identify the parent phase of the CaLa112 system, in which a monoclinic to triclinic structural phase transition and a paramagnetic to stripe-like antiferromagnetic phase transitions are clearly evidenced. In addition, the metallic nature of its spacer layers is demonstrated. By Co doping on the Fe sites in CaLa112, we suppress the structural/magnetic phase transitions and induce superconductivity up to 20 K in a dome

shaped region in the temperature-dopant concentration phase diagram. Our measurements of the superconducting and magnetic volume fractions show that these two phases coexist microscopically in the underdoped region, in contrast to the Co doped 10-3-8 compound, where coexistence is absent. Supported by model calculations, we discuss the differences in the phase diagrams of the 112 and 10-3-8 compounds in terms of the FeAs interlayer coupling, whose strength is affected by the character of the spacer layer, which is metallic in the 112 and insulating in the 10-3-8. Finally, we extend the discussion from CaLa112 to CaRE112 (RE = Ce, Pr, Nd). The structural and magnetic phase transitions of the FeAs layer are revealed in $Ca_{0.71}RE_{0.29}FeAs_2$ (RE = Ce, Pr, Nd). Using $Ca_{0.71}Ce_{0.29}FeAs_2$ as a representative, we demonstrate that an antiferromagentic ordering of Ce strongly entangled with the Fe moments develops at low temperatures. When Co is doped on the Fe sites in $Ca_{0.71}Ce_{0.29}FeAs_2$, we show although Co doping suppresses the magnetic/structural ordering of the FeAs layer, it has little effect on the Ce ordering. We argue the lack of bulk superconductivity in Co-doped $Ca_{0.71}Ce_{0.29}FeAs_2$ arises from the excess electron doping of FeAs layer.

The dissertation of Shan Jiang is approved.

Yu Huang

Stuart Brown

Ni Ni, Committee Chair

University of California, Los Angeles

2017

I would like to dedicate this thesis to my parents,
without whose love, support and encouragement I would not have been able to complete this Ph.D. degree.

Table of Contents

List of Figures

List of Tables

Acknowledgments

I would like to present my sincere gratitude to many people that have guided and helped me through the journey in pursuing my Ph.D. degree. The completion of my dissertation would have been impossible without their company and help.

First and foremost, I would like to express my gratitude to my advisor, Prof. Ni Ni for her endless support and encouragement. Ever since I joined Ni's group, Ni has always been very patient and knowledgeable in guiding me through various problems and constant difficulties. Her passionate and enthusiastic attitude is very infectious and greatly motivated me to think positively and independently. I benefited enormously from her research philosophy which is best summarized by "Think Before You Start and Double Check After You Finish". I would also like to express my deep appreciation for her support in allowing me to attend many conferences and trainings for user facilities in national labs. It has been a great pleasure to work with her.

It has also been a great honor to work with the fantastic members of our group. Costel Rotundu was the postdoctoral researcher at the time I joined Ni's group. He and Ni were my instructors and taught me everything starting from the basics. I gained a lot from his valuable experience and fun personality. Louis Yang joined our lab a bit later than me but I enjoyed the time that we worked together, especially through periods of time where we had heavy maintenance duties. Eve was another graduate student in our group who has always been very helpful and supportive. Besides sharing the lab burden with me, the discussion with her always gave me a chance to refresh my mind and reach further in my research. Ruby was an undergraduate student when we first met. She was also a great assistant and with her help my progress was accelerated remarkably. Another postdoc, Bing, who joined our group around my fourth year, truly helped me a lot. Also being my neighbor, I benefited both mentally and academically from chatting with him. I have enjoyed many conversations about physics with other group members as well: Jie Xing, Xu Liu, Alvin Garcia, Adam

Doorenbos. In addition, I would like to acknowledge Professor John Miao, Professor Stuart Brown and Professor Sudip Chakravarty for valuable lectures and many enlightening discussions.

I would also like to express my appreciation to our collaborators. Frank shared with me his detailed knowledge of the wavelength dispersive spectroscopy technique. Thanks to Jie Ma, Huibo Cao and Wei Tian for helping me out on elastic neutron scattering measurements, from the experimental design to data analysis. The delightful discussions with them gave me significant information on understanding the physical picture of my system, not to mention the follow-up discussions and paper writing that I frequently needed their help with. The collaborations with Prof. Graeme Luke's group and Prof. Yasutomo J. Uemura's group on muon spin relaxation were quite enjoyable and fruitful. Lian and Yipeng shared with me insights on every part of my experiment and taught me how to perform the refinement of the data step by step. Also, many thanks to Matthew J. Krogstad, Keith M. Taddei and Stephan Rosenkranz for collaborating with me on high resolution synchrotron X-ray measurements. I would additionally like to thank Keith for the kind and caring email after the shooting tragedy at UCLA. The theoretical support from Professor Gabriel Kotliar's group and Professor Rafael Fernandes are deeply appreciated. Finally, many thanks to Prof. Yu Huang, Prof. Stuart Brown and Prof. Rahul Roy for joining my thesis committee.

In addition, I am very lucky to have made many great friends at UCLA that enriched my life and graduate school experience in so many ways : Yi Li, Louis Yang, Michale Ip, Alden Fan, Hector Garcia, Andreea Georgescu, Garrett Reynolds, Li Wu, Yi Wang, Xueping Long, Zhiqiang Wang, Yunfeng Xi and Cheng Peng.

Finally, I would like to thank my parents for their constant encouragement and support through every situation. I shared my happiness and sense of accomplishment, but also my fears and hesitance with them. Always, their love and understanding are the feedback run-

ning from the other side of the earth to me. I could not have completed my degree without them.

Vita

2007—2011 B.S. (Physics), Peking University, Beijing, China

2011—2017 PhD Student (advanced to candidacy in 2014), Experimental Condensed Matter, Department of Physics and Astronomy, University of California, Los Angeles, USA.

Publications

Andrs Gyenis, Hiroyuki Inoue, Sangjun Jeon, Brian B Zhou, Benjamin E Feldman, Zhijun Wang, Jian Li, **Shan Jiang**, Quinn D Gibson, Satya K Kushwaha, Jason W Krizan, Ni Ni, Robert J Cava, B Andrei Bernevig, Ali Yazdani, Imaging electronic states on topological semimetals using scanning tunneling microscopy, New Journal of Physics **18**, 105003(2016)

Shan Jiang, Chang Liu, Huibo Cao, Turan Birol, Jared M. Allred, Wei Tian, Lian Liu, Kyuil Cho, Matthew M. Krogstad, Jie Ma, Keith Taddei, Makariy A. Tanatar, Ruslan prozorov, Stephan Rosenkranz, Yasutomo J. Uemura, Gabriel Kotliar and Ni Ni, Structural and magnetic phase transitions in $Ca_{0.73}La_{0.27}FeAs_2$ with electron-overdoped FeAs layers, Phys. Rev. B **93**, 054522(2016)

Hiroyuki Inoue, Andrs Gyenis, Zhijun Wang, Jian Li, Seong Woo Oh, **Shan Jiang**, Ni Ni, B. Andrei Bernevig and Ali Yazdani, Quasiparticle interference of the Fermi arcs and surface-bulk connectivity of a Weyl semimetal, Science, **351**, Issue 6278, pp. 1184-1187(2016)

J. W. Harter, H. Chu, **S. Jiang**, N. Ni, and D. Hsieh, Nonlinear and time-resolved optical study of the 112-type iron-based superconductor parent $Ca_{1-x}La_xFeAs_2$ across its structural

phase transition, Phys. Rev. B **93**, 104506(2016)

Yazhou Zhou, **Shan Jiang**, Qi Wu, Vladimir A. Sidorov, Jing Guo, Wei Yi, Shan Zhang, Zhe Wang, Honghong Wang, Shu Cai, Ke Yang, Sheng Jiang, Aiguo Li, Ni Ni, Guangming Zhang, Liling Sun and Zhongxian Zhao, Discovery of a bi-critical point between antiferromagnetic and superconducting phases in pressurized single crystal $Ca_{0.73}La_{0.27}FeAs_2$, submitted, arxiv:1603.05740(2016)

Shan Jiang, Lian Liu, Michael Schutt, Alannah M. Hallas, Bing Shen, Wei Tian, Eve Emmanouilidou, Aoshuang Shi, Graeme M. Luke, Yasutomo J. Uemura, Rafael. M. Fernandes, and Ni Ni, Effect of interlayer coupling on the coexistence of antiferromagnetism and superconductivity in Fe pnictide superconductors: A study of $Ca_{0.74(1)}La_{0.26(1)}(Fe_{1-x}Co_x)As_2$ single crystals, Phys. Rev. B **93**, 174513(2016)

Costel R. Rotundu, **Shan Jiang**, Xiaoyu Deng, Yiting Qian, Saeed Khan, David G. Hawthorn, Gabriel Kotliar and Ni Ni, Physical properties and electronic structure of a new barium titanate suboxide $Ba_{1+d}Ti_{13-d}O_{12}$ (d = 0.11), APL Mat. **3**, 041517 (2015)

Shan Zhang, Qi Wu, Leslie Schoop, Mazhar N Ali, Youguo Shi, Ni Ni, Quinn Gibson, **Shan Jiang**, Vladimir Sidorov, Wei Yi, Jing Guo, Yazhou Zhou, Desheng Wu, Peiwen Gao, Dachun Gu, Chao Zhang, Sheng Jiang, Ke Yang, Aiguo Li, Yanchun Li, Xiaodong Li, Jing Liu, Xi Dai, Zhong Fang, Robert J Cava, Liling Sun, Zhongxian Zhao, Breakdown of three-dimensional Dirac semimetal state in pressurized Cd_3As_2, Phys. Rev. B **91**, 165133 (2015)

CHAPTER 1

Introduction

Modern research of condensed matters devotes in understanding how properties of complex solids are determined by their structural and electronic degrees of freedom. In spite of the complexity of real materials where competing orders often exist, significant progress has been driven by the discovery and study on new materials with emergent ground states. From high temperature superconducting cuprates to colossal magnetoresistive manganites, from permanent ferromagnetic magnet to ferroelectric oxides, these discoveries not only lead to past and potential technology revolutions, but also bring revolutionary insights to our understanding of correlated matter.

1.1 Brief introduction to strongly correlated systems

Strongly correlated systems are among the most studied topics in condensed matter physics. Unlike most metal systems, which have much weaker Coulomb interaction energies than electron kinetic energies, indirect or direct electron-electron coupling plays an important role in tuning the physical properties of strongly correlated electron systems, such as unconventional superconductors, Mott insulators, heavy fermions, etc. However, the interacting particles need not be electrons; rather, more generally, the term of particles/quasiparticles could be extended to all possible degrees of freedom within a crystal, including but not limited to electrons, spins, charges, orbitals, and lattices. Those diverse types of interacting sources in turn create a wider range of combinations of interactions. Consequently, it is quite understandable that strongly correlated systems have very rich and exotic physical phases as their most profound feature.

For instance, multiferroics, defined as a special class of compounds that possess two or more ordered states (ferromagnetism, ferroelectricity, etc.), were understood by coupling among the electric field, electric polarization, applied mechanical stress, magnetic field, and magnetization of the compounds[Vop15]. These systems are usually realized in perovskite-structure transition metal oxides such as $BaTiO_3$ and $PbZr_{1-x}Ti_xO_3$-type compounds[Vop15]. Further, heavy fermions, another strongly correlated system, are commonly observed in compounds baring $4f$ or $5f$ electrons near the Fermi level, which demonstrate extraordinarily large specific heat (Sommerfeld) coefficients γ and exhibit Curie–Weiss-like behavior of the magnetic susceptibility. This enhancement of the effective electron mass is widely believed to be attributed to the interactions between conduction electrons and f electrons according to the theory of the Kondo effect and Kondo lattice model[Ste84, WTM15]. Furthermore, the heavy fermion compounds CeM_2X_2 (M = Ni, Cu, Rh, Pd; X = Si, Ge) and $CeMIn_5$ (M = Co, Rh, Ir; so-called 115 systems) are extensively studied because of the emergence of superconductivity at temperatures up to a few kelvins under pressure. As evidence that the large jump in the heat capacity is on the order of γT_c, Cooper pairs are believed to be formed from the heavy quasiparticles[SAB79] as an example of unconventional Type-II superconductivity. Superconductivity, on the other hand, could itself be explained as representing another independent, typical strongly correlated system by immense experimental and theoretical effort across a vast range of materials such as oxides, magnetic compounds, organic compounds, making this subfield one of the most challenging yet to be understood.

Superconductivity was first observed in high-purity mercury in April, 1911[Onn11] as a sudden drop in the electrical resistance to zero at 4.2 K. A series of elemental superconductors, followed by a few binary superconductors, with T_c values up to 23.2 K[Gav73] were subsequently found. It was not until 1986 that the discovery of $La_{1-x}Ba_xCuO_4$ with a T_c of 30 K[BM86] sparked continuous intensive research on high-temperature superconductivity. The discovery of superconducting (SC) cuprates greatly stimulated experimental work on

the synthesis and characterization of related compounds and theoretical exploration of the area beyond the Bardeen–Cooper–Schrieffer (BCS) theory. Within the next several decades, the discovery of materials such as $YBa_2Cu_3O_{7-\delta}$ (with T_c values up to 93 K[WAT87]), the $Tl_2Ba_2Ca_nCu_{n+1}O_{2n+6-\delta}$ series (with T_c values up to 120 K[SH88]), and $HgBa_2Ca_2Cu_3O_{8+x}$ (with T_c values up to 133 K[SCG93]) not only updated the critical temperature records, but also attracted attention to concepts such as the pseudogap, d-wave pairing, charge density waves, with support from rapidly developing probing techniques, such as angle-resolved photoemission spectroscopy (ARPES), scanning tunneling microscopy, etc., that enabled higher resolution and detection efficiency. However, the origin of high-temperature superconductivity remains elusive.

1.2 Brief introduction to Fe-based superconductors

It has been a long time that the cuprates served as the only known "high temperature" superconductors for the physicists to understand how high Tc superconductivity can be realized. Due to the lack of a second high T_c system as a comparison, the understanding of high Tc superconductivity is limited and the recipe for producing high T_c superconductivity is somehow misleading. The parent compound of the cuprates is a Mott insulator where the strong electron correlation splits the unfilled d band into an upper and lower Hubbard bands straddling the Fermi level and thus providing an insulating state. In cuprates, there is only one pocket at the Fermi level coming from the d_9 configuration of Cu^{2+}. Therefore, it has been thought high T_c superconductivity may only be found in quasi-two dimensional materials with S = 1/2 spin state and with strong electron correlations. Searching for new high T_c superconducting systems along this direction has not been fruitful—Sr_2RuO_4 is the only one which is superconducting, but at 1.5 K. Furthermore, although BCS theory has provided a microscopic theoretical frame to understand the origin of conventional superconductivity,

but the mechanism to glue Cooper pairs is still unclear. The symmetry of the superconducting order parameter, the role of the quasi-2D structure, spin fluctuation, nematic order and quantum critical point, are under extensive debate for unconventional superconductors and the search of new superconductors is still by chance rather than prediction. Therefore, as the second known high-temperature superconducting family to date, Fe-based superconductors (FBSs) have attracted extensive research effort, not only in the hope that technologically applicable superconductors may exist in this class due to their high critical current and low anisotropy, but also because of its multiband nature and rich interplays among the structure, antiferromagnetism and superconductivity. They provide a great avenue to study how structural and electronic degrees of freedom determine the physical properties and enrich our understanding of high T_c superconductivity.

The discovery of Fe-based superconductors (FBSs) with the observation of a critical temperature of 26 K for LaFeAsO by Prof. Hosono[KWH08] in 2008 marked the beginning of a new era. Intensive research has revealed two families: Fe pnictides (FePn, where Pn denotes As or P) and Fe chalcogenides (FeCh, where Ch includes S, Se, and Te). Considered as the second unconventional high-T_c superconductor family, the FBSs share a few features with cuprate superconductors, such as a layered crystal structure, relatively high T_c, superconductivity in the proximity of the magnetic phase that is induced by tuning parameters such as the chemical doping or pressure, and, especially, the strikingly similar temperature-concentration ($T - x$) phase diagram. Further, electronic conduction is widely believed to be associated with the FeAs/FeSe layers, whereas cuprates have delocalized charge carriers in the basal copper oxide planes[KHY08]. Nevertheless, the differences are significant:

- The superconductivity of cuprates is derived from doping a Mott insulator, but the parent compound of FBS is a poor metal owing to partial gapping around the Fermi surface (FS) at low temperature[QHB09], which does not initiate an insulating state.
- In the edge-sharing tetrahedron, the pnictogen anions are arranged above and below the Fe plane rather than at the same height, as in the copper oxide plane[PG10].

- The T_c of cuprate superconductors drops rapidly upon doping its two-dimensional (2D) copper oxide plane. However, FBSs are relatively insensitive to this effect[Ste11].

These discrepancies clearly show that our fundamental understanding of the origins of superconductivity needs significant improvement.

FBSs can generally be classified into several typical groups according to their crystal structure and chemical formula: the 1111 system, RFeAsO (R = La, Ce, Pr, Nd, Sm etc.)[TIA08a, CLW08, RYL08a, RYL08b, TIA08b, KZK09]; the 122 system, $AeFe_2As_2$ (Ae = Ca, Sr, Ba)[RTJ08, CLD08, SJM08, LLW09, NTY08]; the 111 system, AFeAs (A = Li, Na)[TTL08, WLL08, CCG09, PPB09, RAA14]; the 11 system, $A_xFe_{2-y}Se_2$ (A = K, Rb etc.)[HLY08, SKB11, MTM08, DFW13, WYY11, Wen12]; the 10-n-8 system, $Ca_{10}(Pt_nAs_8)(Fe_2As_2)_5$ (A = Pt, Pd, Ir; n = 3,4)[KKN11, LST11, SSJ16, NAC11, KSS14]; and the 112 system, $Ca_{1-x}A_xFeAs_2$ (A = La, Ce, Pr, Nd etc.)[KKO13, RA16, CSF16, PMY16, YXD16, XZZ16, HYL15, ZXZ15, YOS15b, NNM15, YOS15a, RGM15, KMM15, SYO14, OOY14]. Over these groups, a few hundred compounds have reportedly been obtained by varying the concentration of various dopants and the pressurization. Here I borrow a figure from [Ste11] to illustrate the progress on the 122 family. Although the induction of superconductivity in the 122 family seems to be common, it is worth noting that the doping element, doping site, dopant type, and tuning of the lattice constant by isovalent doping all affect the critical temperature. Notably, it has been reported that a few 1111 family members have T_c values as high as 55–58 K, which is recognized as the current T_c record for FBSs[WLC08, RCD08, HMM11, FDO13].

Like in Cuprates, superconductivity in FBSs appears near the magnetic instability, magnetism is then generally believed to be important in the pairing mechanism of high T_c superconductivity[Sca12]. Long-range collinear stripe-like antiferromagnetism has been discovered in the parent compounds of the 1111, 122, and NaFeAs, except for LiFeAs and FeSe, where LiFeAs is self-doped due to the chemical complicity of Li and FeSe shows magnetic ordering under pressure. The moment is aligned along the a axis of the low-

temperature orthorhombic phase (Figure 1.7). Other types of AFM configuration are bi-collinear (as found in FeTe[LCH09]) and incommensurate helical magnetic ordering ($Fe_{1+x}Te$ when $x > 12\%$[RSS13]).

TABLE II. T_c versus composition in $M_{1-x}A_xFe_{2-y}TM_yAs_{2-z}P_z$ T_cs given are the maxima versus composition. Only one site is doped at a time.

Material	M-site dopant	T_c (K) vs x, $y = z = 0$	Ref.	Fe-site dopant	T_c (K) vs y, $x = z = 0$	Ref.	As-site dopant	T_c (K) vs z, $x = y = 0$	Ref.
$BaFe_2As_2$	K	38/0.4	Rotter, Tegel, and Johrendt (2008)	Co	22/0.2	Sefat *et al.* (2008b)	P	30/0.7	Kasahara *et al.* (2010); Jiang *et al.* (2009)
	Rb	23/0.1	Bukowski *et al.* (2009)	Ni	20.5/0.1	L. J. Li *et al.* (2009)			
				Pd	19/0.11	Ni *et al.* (2009)			
				Rh	24/0.11	Ni *et al.* (2009)			
				Ru	21/0.9	Sharma *et al.* (2010)			
				Pt	25/0.1	Zhu *et al.* (2010); Saha *et al.* (2010b)			
$SrFe_2As_2$	K	36.5/0.5	Sasmal *et al.* (2008)	Co	20/0.2	Leithe-Jasper *et al.* (2008)	P	27/0.7	Shi *et al.* (2009)
	Na	35/0.5	Goko *et al.* (2009)	Ni	10/0.15	Saha *et al.* (2010a); Leithe-Jasper *et al.* (2008)			
	Cs	37/0.5	Sasmal *et al.* (2008)	Pd	9/0.15	F. Han *et al.* (2009)			
	La	22/0.4	Muraba *et al.* (2010)	Rh	22/0.25	F. Han *et al.* (2009)			
				Ru	13.5/0.7	Qi *et al.* (2009a)			
				Ir	22/0.5	F. Han *et al.* (2009)			
				Pt	16/0.16	Kirshenbaum *et al.* (2010)			
$CaFe_2As_2$	Na	33/0.66	K. Zhao *et al.* (2010) (see also Wu *et al.*, 2008a)	Co	17/0.06	Kumar *et al.* (2009b)	P	13/0.3	Shi *et al.* (2009)
				Ni	15/0.06	Kumar *et al.* (2009a)			
				Rh	18/0.1	Qi *et al.* (2011)			
$EuFe_2As_2$	K	32/0.5	Jeevan *et al.* (2008b), Anupam *et al.* (2009)				P	26/0.6	Ren *et al.* (2009); Jeevan *et al.* (2011)
	Na	35/0.3	Y. Qi *et al.* (2008)						

[a]Note: Cu substituted for Fe in $BaFe_2As_2$ suppresses T_S and T_{SDW} but does not induce superconductivity (Canfield *et al.*, 2009b) while Mn substituted for Fe in $SrFe_2As_2$ up to $x = 0.3$ is relatively ineffective in suppressing T_S and T_{SDW} (Kasinathan *et al.*, 2009).

Figure 1.1: Selected reports on critical temperature of various FBSs[Ste11].

At the time of my work, intensive research on the 11, 111, 1111, and 122 systems had revealed a few common properties that presumably hold the clue to understand the relatively high critical temperature for the onset of superconductivity[Ste11] in FBSs:

- All of the discovered FBSs compounds contain 2D planes made of edge-sharing $FeAs_4FeSe_4$ tetrahedra(Figure 1.2). In the other word, FeAs/FeSe layers are the ones mediating superconductivity. This finding sparked interest in research on the correlation between the critical temperature and details of the tetrahedral geometry, specifically, the bond angle and As/Se height above the Fe ion[LIE08].

- The $3d$ electron orbital of Fe is close to the Fermi level and clearly plays an very important role in the superconductivity[RQL08].

- For most FBSs, the parent compound and lightly doped ones exhibit both structural and magnetic phase transitions, with very few exceptions. Interestingly, the two tran-

sition temperatures either coincide or differ slightly. Commonly, they evolve from a high-temperature tetragonal paramagnetic phase into a low-temperature orthorhombic antiferromagnetic (AFM) phase. However, this feature is slightly different in the 10-3-8 and 112 systems, as I will explain in the next section.

- The magnetism in Cuprates is clearly localized. However, it is still under debate if the nature of the magnetism in FBSs is localized or itinerant. Nevertheless, the spin-fluctuation resonance found in the 1111, 122, 111, and 11 superconductors below T_c provide strong evidence regarding whether the superconductivity in FBSs is mediated by spin fluctuations.

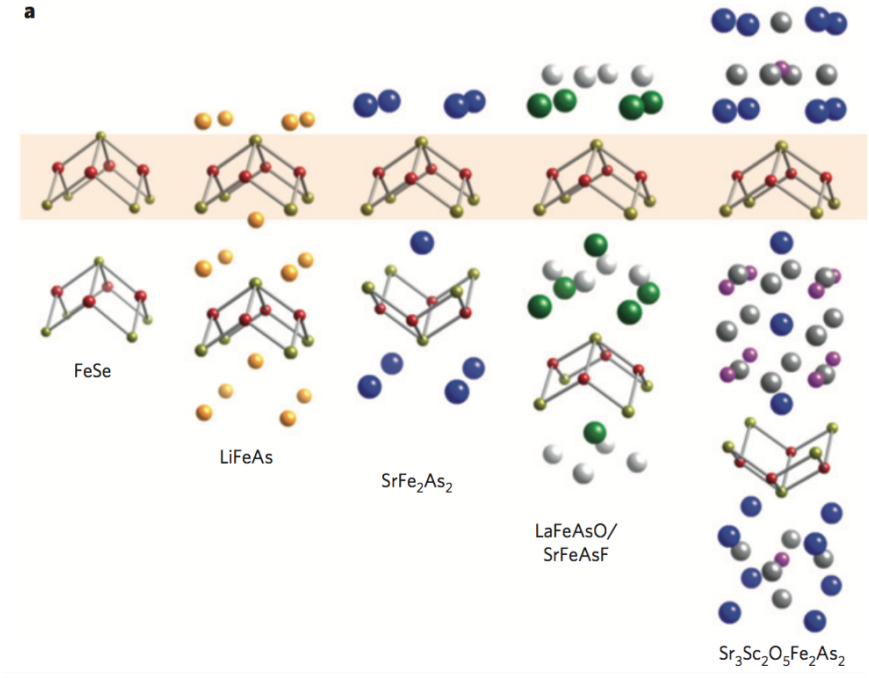

Figure 1.2: Representative crystal structures of the FBSs [PG10].

1.3 Brief introduction to 10-3-8 and 112 families

Research on the 10-3-8 and 112 families was at a relatively early stage when I began to focus on these compounds. The discovery of 10-3-8 and 10-4-8 compounds in early 2011 and 112

pnictide compounds in later 2013 [KKN11, NAC11, LST11, KKO13], broadened our view of the chemical and structural complexity of FBSs.

Let me start from the structural perspective. The 10-3-8 and 10-4-8 families refer to the compounds with the chemical formula of $Ca_{10}Pt_nAs_8(FeAs)_{10}$ ($n = 3$ or 4). Both of them have the -Ca-(Pt_nAs_8)-Ca-Fe_2As_2-layer stacking ($n = 3$ or 4) with the skutterudite Pt_nAs_8 spacer layers. In the Pt_nAs_8 layer, the formation of As-As dimers with a bond length of $\sim$2.6 $\mathring{A}$ leads As_2^{4-}. In addition, due to the stability of the d^8 configuration of Pt, the only oxidization state for Pt is 2+. This results in a spacer layer of $[Pt_3As_8]^{10-}$ for the 10-3-8 phase and $[Pt_4As_8]^{8-}$ for the 10-4-8 phase. Therefore, integer oxidization states can be assigned for all elements in 10-3-8 as $Ca_{10}^{20+}[Pt_3As_8]^{10-}[Fe_2As_2]_5^{10-}$ but not for the 10-4-8, suggesting the insulating nature of the Pt_3As_8 layer but the metallic nature of the Pt_4As_8 layer. Unlike the typical tetragonal structural of the parent FBSs, the parent 10-3-8 phase forms in a triclinic structure (group space: $P\bar{1}$) at room temperature ($a = b \approx 8.78$ $\mathring{A}$, $\gamma \approx 90°$). However, due to the equal a and b lattice parameters, the local fourfold C_4 rotational symmetry of the FeAs layers is preserved. Synchrotron x-ray and neutron diffraction data on the 10-3-8 single crystal [STR14] suggests a triclinic to triclinic structural phase transition with unequal a and b below 110(2) K, which destroys the local C_4 symmetry in the FeAs layer[SFL13].

The 112 compound is the other example of a FBS with low-symmetry. It crystalizes in the monoclinic structure with the -Ca-As-Ca-Fe_2As_2 layer stacking. The As spacer layers are made of As zigzag chains with the intra-chain As-As bond distance of 2.46 $\mathring{A}$ and inter-chain As-As bond distance as 3.02 $\mathring{A}$. Since the As-As bond formation distance is 3.0 $\mathring{A}$, along the chain direction, As-As dimers are formed. The zigzag As chains distort the FeAs layer so that it lacks the local C_4 rotational symmetry even at room temperature. Soon after the initial debate if the space group is noncentrosymmetric $P2_1$[KKO13] or centrosymmetric $P2_1$/m[YOO14], rotational anisotropy optical second-harmonic generation measurement concluded that $Ca_{1-x}La_xFeAs_2$ belongs to a noncentrosymmetric monoclinic

$P2_1$ lattice system[HCJ16], a derivative of the $HfCuSi_2$ structure[KWI11, HMS13, RBK15].

The role of the distinct nature of the spacer layers in 10-n-8 has attracted extensive research effort, considering the huge T_c difference in Pt doped 10-n-8 (11–15 K for 10-3-8 and 26–38 K for 10-4-8)[SSJ16, NAC11]. Overall, metallic spacer layers can have two major effects in affecting the electronic structure. Firstly, it will enhance the FeAs interlayer coupling, resulting in a Fermi surface with less k_z dispersion. Secondly, it will self-dope the FeAs layer without bringing chemical impurities on the FeAs layer. The higher critical temperature in 10-4-8 was tentatively attributed to the stronger FeAs interlayer coupling in 10-4-8 mediated by the metallic Pt_4As_8 layers in the original work. This was inspired by the observation that the 10-3-8 SC has much higher anisotropy parameter than the 10-4-8 ones, despite that both of them have similar FeAs interlayer distance[NAC11]. On the other hand, a few followup theoretical calculations[Ber14] suggested that both Pt_3As_8 and Pt_3As_8 layers contribute certain amount of density of states at the Fermi level, but the electronic structure is not significantly influenced by the presence of the them. Further more, these calculations shows the 10-4-8 compounds possess lower Pt 5d bands, which are more likely to self-donate electrons to the FeAs layers. All ARPES measurements[NLX12, TSZ13] indicate that the Fermi surface of the 10-n-8 family is similar to that of the 122 and 1111 compounds with center hole pockets and corner electron pockets in the first Brillouin zone. Both ARPES experiments[NLX12, TSZ13] measured on the parent and optimally doped 10-3-8 show no clear evidence of density of states arising from the Pt_3As_8 layer, suggesting its insulating nature. The ARPES experiments on the 10-4-8[TSZ13, SCG13b] show that depending on the doping level, Pt_4As_8 layer may or may not contribute density of states at the Fermi level. Furthermore, the energy distribution map data suggest that 10-4-8 crystals are less electron-doped than those of 10-3-8, suggesting that the origin of the high T_c of the 10-4-8 phase is indirect electron transfer from Pt_4As_8 to the FeAs layers[LST11] rather than interplay coupling. This was supported by the observation that La-doped 10-3-8 with no Pt on the FeAs layer exhibits superconductivity with a critical temperature of around 30 K[SDJ12]

while Co- and Ni-doped 10-3-8 show superconductivity up to 15 K. This is in agreement with the fact that doping on the FeAs layer is detrimental to T_c[SKJ14]; and 10-3-8 doped with a series of rare earth elements shows a T_c higher than that obtained when the dopant is at the Fe site (Figure 1.3[SDB15]).

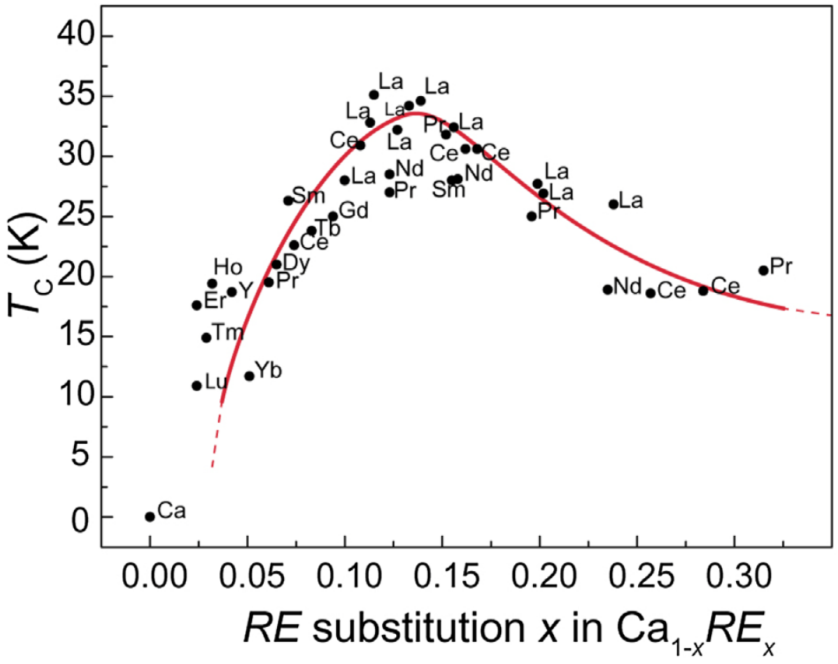

Figure 1.3: The superconducting critical temperatures of the $(Ca_{1-x}RE_x)_{10}(FeAs)_{10}Pt_3As_8$ vs. x, the RE substitution in $Ca_{1-x}RE_x$ [SDB15].

As to the 112 family, its experimental discovery is closely associated with the theoretical prediction. The existence of superconductivity was first claimed by Kotliar to be in the hypothetical compounds $BaFeAs_2$ and $BaFeSb_2$ with metallic spacer layers unlike the insulating spacer layers in other pnictides. This suggested that it is a suitable compound to examine the role of charge fluctuation and dimensionality in the superconductivity mechanism[SHK09]. Early work focused on $SrMnBi_2$ [PLW11] and $CeTMPn_2$ (TM = transition metal, Pn = pnictogen) (superconductors with $T_c \approx 4$ K)[RJA15]. It was not until the discovery of $Ca_{1-x}La_xFeAs_2$ with $T_c \approx 34$ K[KKO13] that intensive investigation of this new Fe pnic-

tide system started. Although neither $CaFeAs_2$ nor $LaFeAs_2$ was successfully synthesized. Superconductivity could be obtained in a few derivative compounds by elemental doping and pressurization. $Ca_{1-x}La_xFeAs_2$ exists in a very limited x concentration range between 0.18 and 0.27, T_c could be greatly enhanced to 41 K[KMK14] by a small amount of P doping on the As site. Various levels of Sb doping could enhance T_c further to 43 and 47 K[KMK14, KKF14], where the 47 K compound showed a superconducting volume fraction (SVF) of 100% at 2 K, which was higher than those of previously reported compounds. Further, replacing La with other rare earth elements using high-pressure synthesis has led to polycrystalline $Ca_{1-x}RE_xFeAs_2$ (RE = Pr, Nd, Sm, Eu, Gd) with T_c ranging from 10 to 25 K [SYO14] while the Ce version of 112 shows no sign of superconductivity at attainable doping levels. On the other hand, considering the opportunity to dope the Fe sites, transition element doping of $Ca_{1-x}RE_xFeAs_2$ is being vigorously explored. Remarkably, Co doping on the Fe site actually enhances T_c to above 30 K for RE = La, Ce, Pr, Nd, and Sm [SYO14, XZX15], which doped the CaCe112 into a superconductor. The doping research is summarized in Fig. 1.4[RA16].

1.4 Thesis organization

These structural novelties have raised the following intriguing questions:

- How does the nature of the space layers affect the the physical properties in FBSs?

We would like to discuss this in a more confined perspective, how does the nature of the spacer layers affect the competing orders in FBSs? As we mentioned, the interplay of competing orders lies at the heart of the study of strongly correlated electron systems. Tuning various energy scales by chemical doping or external pressure have enriched our understanding of these systems. Now, we would like to add one more tuning parameter, that is the electronic anisotropy into the discussion. To shed light on this quest, a systematic investigation of the 10-3-8 and 112 FBSs families with non-trivial crystal structures has been conducted.
This thesis is organized as follows:

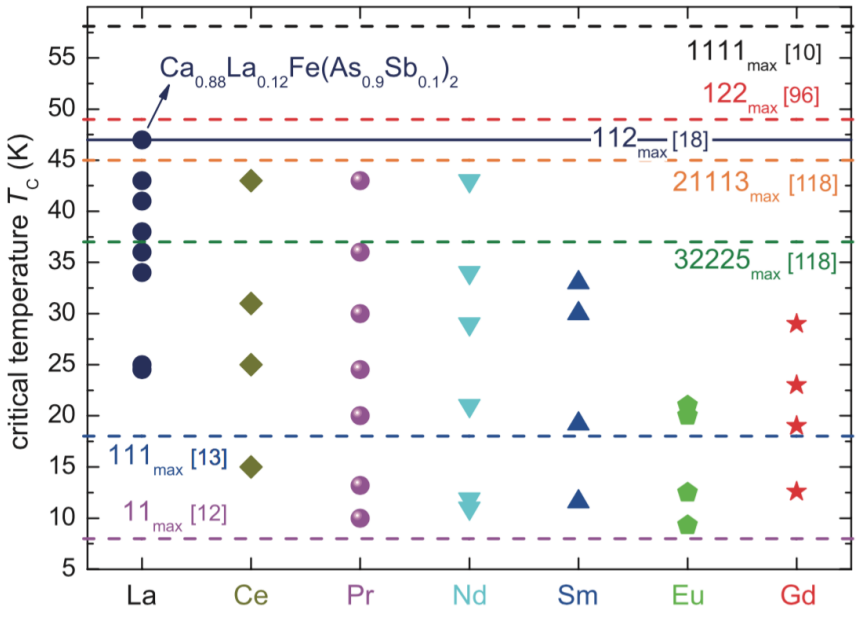

Figure 1.4: The summary of the superconducting critical temperatures of the CaRE112 family vs. RE elements. Horizontal dash lines indicate the maximal T_c values reported for other families of pnictides[RA16].

Chapter 2 is a brief theoretical overview of superconductivity.

Chapter 3 describes the experimental methods, including the growth method and various measurement techniques.

Chapter 4 presents the synthesis, transport, thermodynamic and neutron scattering study of Co-doped 10-3-8 single crystals. The temperature–doping concentration phase diagram is mapped out. We conclude that within our experimental resolution, no phase coexistence of antiferromagnetism and superconductivity is observed.

Chapter 5 presents a combined structural, transport, thermodynamic, neutron scattering and ARPES study of high-quality $Ca_{0.73}La_{0.27}FeAs_2$ single crystals obtained using our original recipe. We first reveal the existence of the monoclinic to triclinic phase transition and the paramagnetic to antiferromagnetic phase transition in this compound. Furthermore, we provide solid evidence to elucidate the metallic nature of the As zigzag chains.

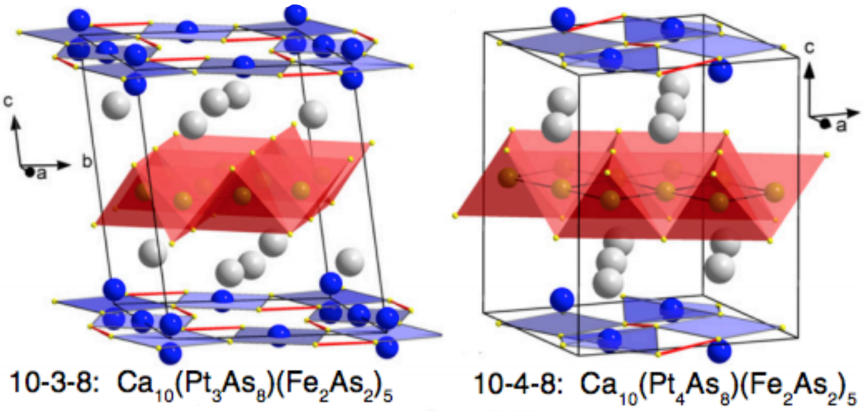

Figure 1.5: The crystal structures of the 10-3-8 (left) and 10-4-8 (right) phase. Red: FeAs tetrahedra; White: Ca; Blue: Pt; Yellow: As [NAC11].

Chapter 6 presents a systematic study of Co-doped $Ca_{0.74(1)}La_{0.26(1)}FeAs_2$ single crystals by transport, thermodynamic, μSR and neutron scattering measurements. We map out the temperature–doping concentration phase diagram. We show unambiguously the phase conexistence between antiferromagnetism and superconductivity in this system in the underdoped region. Supported by model calculations, we discuss the differences in the phase diagrams of the Co doped CaLa112 and Co-doped 10-3-8 compounds in terms of the FeAs interlayer coupling, whose strength is affected by the character of the spacer layer, which is metallic in the 112 and insulating in the 10-3-8.

Chapter 7 presents a combined transport, thermodynamic, μSR and neutron scattering study of $Ca_{1-x}RE_xFeAs_2$ (RE = Ce, Pr, Nd). In addition to the structural and magnetic phase transitions associated with the FeAs layer, we observe profound interplay between the Fe magnetism and rare earth magnetism in these systems. Our study of $Ca_{0.71}Ce_{0.29}(Fe_{1-x}Co_x)As_2$ single crystals shows although the structural/magentic instability associated with the FeAs layers is effectively suppressed, the Ce ordering persists and no superconductivity appears even when the structural/magentic phase transitions are fully suppressed.

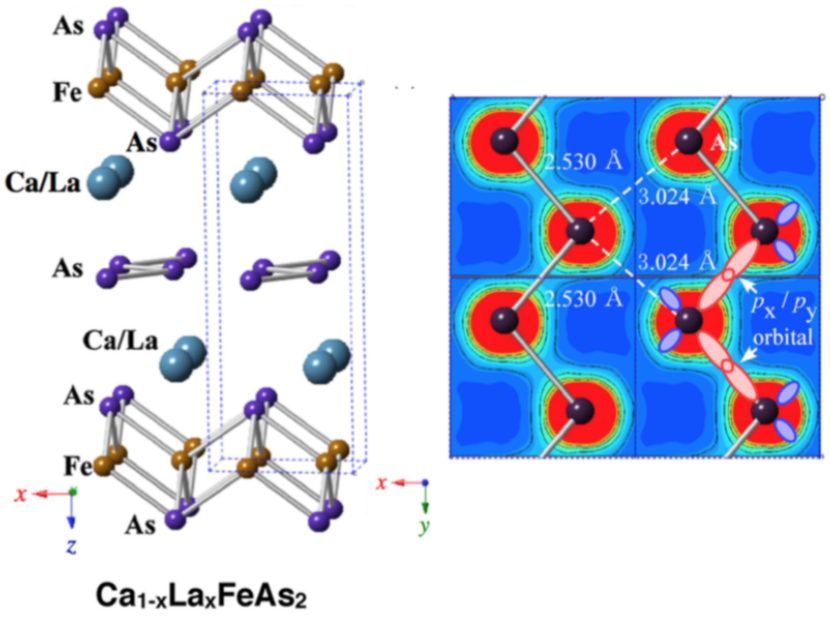

Figure 1.6: The crystal structure of CaLa112 (left); The top view of the As zigzag chain (right). Color map represents the contour of the charge distribution around As atoms and bonds formed within one chain [RA16].

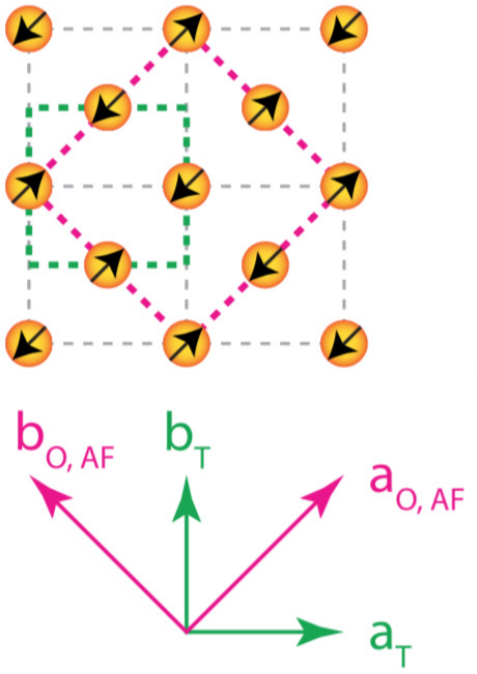

Figure 1.7: Collinear stripe AFM structure in Fe plane, where the dashed boxes mark the tetragonal crystalline unit cell in the paramagnetic state and the orthorhombic magnetic unit cell, respectively; a_T, b_T and $_{o,AF}$, $b_{o,AF}$ mark the directions of the tetragonal and orthorhombic lattice, respectively [Dai15].

CHAPTER 2

Overview of Superconductivity

2.1 Characteristics of superconductivity

The most notable characteristics of a perfect superconductor are zero electrical resistance and perfect diamagnetism. When the temperature exceeds the critical temperature, a superconducting material exhibits finite electrical resistivity, and magnetic flux can penetrate the sample. As the temperature passes below this critical temperature, a superconducting state will emerge, and the material will exhibit perfect electrical conductivity ($\rho = 0$) and perfect diamagnetism ($\chi = -1$). The latter characteristic can be obtained in two ways. In a zero-field-cooled (ZFC) process, the sample is placed in a zero field and cooled below the critical temperature. It will block magnetic flux if a field is then applied. In the second process, the field-cooled (FC) process, the sample is placed within a nonzero magnetic field at high temperature. When the temperature drops below the critical temperature, the field will be expelled by the superconducting state, that is, by the Meissner effect. Applying the FC process to a perfect conductor will cause the field to fully penetrate the sample. Therefore, the diamagnetism signal under FC process differentiates a superconductor from a perfect conductor.

To clarify the principles involved in the ZFC and FC processes, assume a cylindrical sample with total volume V_T. It is composed of a superconducting volume V_s, a cylindrical hole of volume V_h that is open at the top and bottom, and an enclosed cylindrical cavity V_c. They obey the following relation:

$$V_T = V_s + V_h + V_c$$

The magnetic moment m is defined as

$$m = VM = V \cdot \frac{\chi B}{\mu_0}$$

where B is the magnitude of the applied field. In the superconducting case, because of the Meissner effect, $\chi = -1$; thus,

$$m_{ZFC} = -(V_s + V_h + V_c)\frac{B}{\mu_0}$$

and

$$m_{FC} = -(V_s + V_c)\frac{B}{\mu_0}$$

Therefore, the ratio of the magnetic susceptibility measured using the FC and ZFC processes is given as

$$\frac{\chi_{FC}}{\chi_{ZFC}} = \frac{m_{FC}}{m - -_{ZFC}} = \frac{V_s + V_c}{V_s + V_h + V_c}$$

This simple model could explain the different behavior of the ratio $\frac{\chi_{FC}}{\chi_{ZFC}}$ in Type I and Type II superconductors.

2.2 Theoretical frameworks for superconductivity

2.2.1 Ginzburg–Landau theory

The Ginzburg–Landau (GL) theory was proposed by Ginzburg and Landau in 1950. It is a phenomenological approach without a microscopic understanding of superconductivity. It is very powerful for understanding and predicting the behavior of superconductors. The theory is formulated in terms of a complex order parameter $\phi(r)$, which involves a phase factor Θ and is formulated as

$$\phi(r) = |\phi(r)|e^{i\Theta}$$

The square amplitude is assumed to be the super-fluid density

$$n_s^* = |\phi|^2$$

It is assumed that the Gibbs free energy per unit volume, $G_x[\phi]$, can be expanded as a local functional of the order parameter when the temperature is close to but below the transition temperature T_c.

$$\begin{aligned} G_s[\phi] &= G_n + \frac{1}{V}\int d^3r[\frac{1}{2m^*}(-i\hbar\nabla + e^*A)\phi^* \cdot (i\hbar\nabla + e^*A)\phi + (\frac{1}{2\mu_0}B^2(r)) \\ &\quad -\mu_0 H(r)M(r) + a\phi\phi^* + \frac{1}{2}b\phi\phi^*\phi\phi^* + \ldots] \end{aligned}$$

where G_n is the free-energy density of the normal state, A is the magnetic vector potential, and a and b are functions that depend only on the temperature. In equilibrium, the currents in the superconductor are distributed in a way that minimizes the total free energy. In a small temperature range near T_c, the parameters a and b can be approximated as

$$\begin{aligned} a(T) &\approx a_0[\frac{T}{T_c} - 1] \\ b(T) &\approx b_0 \end{aligned}$$

According to the function variational principle, minimizing $G_s[\phi]$ leads to the first GL equations

$$\frac{1}{2m^*}(i\hbar\nabla + e^*A)^2\phi + a\phi + b|\phi|^2\phi = 0$$

If the variational derivative of G is taken with respect to A, the second GL equation will be

$$\nabla \times (\nabla \times A) + \frac{i\hbar e^*}{2m^*}(\phi^*\nabla\phi - \phi\nabla\phi^*) + \frac{e^{*2}}{m^*}A|\phi|^2 = 0$$

Solving the first and second GL equations at a boundary between the normal and superconducting states at $A = 0$, we can analytically calculate the order parameter function.

$$\phi = (\frac{|a|}{b})^{\frac{1}{2}} tanh\frac{x}{\sqrt{2}\xi}$$

Here, ξ, namely, the coherence length, is defined as

$$\xi = \sqrt{\frac{\hbar^2}{2m^*|a|}}$$

It is the characteristic length over which ϕ changes substantially. On the other hand, taking the derivative of the current and using the Maxwell equation yields the so-called first London

equation,

$$\frac{dJ_s}{dt} = \frac{n_s e^2}{m} E$$

and the second London equation,

$$\frac{mc}{n_s e^2}(\nabla \times J_s) + B = 0$$

If both equation are combined with the Meissner effect, we obtain

$$\lambda_L^2(\nabla \times \nabla \times B) + B = 0$$

where

$$\lambda_L = \sqrt{\frac{m^*}{\mu_0 e^{*2}|\phi_{infty}|^2}} = \sqrt{\frac{m^* c^2 b}{4\pi e^{*2}|a|}}$$

The penetration depth describes the strength of the exponential field decay inside a superconductor.

If we put the coherence length and penetration depth together and compare the energy difference σ at an interface between a pure phase (either all normal or all superconducting) and a mixed phase, we obtain

$$\begin{aligned} \frac{\lambda_L}{\xi} &< \frac{1}{\sqrt{2}} \Rightarrow \sigma > 0 \Rightarrow \qquad \textit{type I superconductor} \\ \frac{\lambda_L}{\xi} &> \frac{1}{\sqrt{2}} \Rightarrow \sigma < 0 \Rightarrow \qquad \textit{type II superconductor} \end{aligned}$$

If $\sigma > 0$, the homogeneous phase has a lower free energy than the mixed phase. Therefore, the system will stay in the superconducting state until the external field exceeds the critical field. This type of superconductor is defined as a Type I superconductor. Most elemental superconductors are Type I superconductors. Otherwise, $\sigma < 0$, indicating that a mixed state is energetically favorable. This type of superconductor, called a Type II superconductor, will exhibit the complete Meissner effect if the applied field B is less than B_{c1}. When the magnetic field is greater than the lower critical field B_{c1}, magnetic vortices start to penetrate the superconducting region. The magnetization of the sample increases with increasing magnetic field until the value of B reaches that of the upper critical field, at which the entire sample enters a normal state.

The parameters m^*, e^*, and n^* describing the super electrons are linked to the quantities m, e, and n for electrons (see below) as follows:

$$\begin{aligned} m^* &= 2m \\ e^* &= \pm 2e \\ n_s^* &= \frac{1}{2} n_s \end{aligned}$$

These equations are proved by the Bardeen–Cooper–Schrieffer (BCS) theory, which also confirms the correctness of GL theory.

2.2.2 BCS theory

Although the GL theory successfully explains many of the principal properties of superconductors, it does not explain the origin of superconductivity microscopically. Historically, the BCS theory is the first microscopic theory of superconductivity. It was proposed by Bardeen, Cooper, and Schrieffer in 1957, who showed that it could quantitatively predict the properties of a certain subset of elemental superconductors. The GL theory could also be derived from the BCS theory.

The BCS theory assumes that superconductivity arises from the Cooper pair, a state in which the attractive interaction dominates the repulsive Coulomb force. A Cooper pair is an electron–electron pair mediated by a weak attractive interaction, such as electron–phonon interaction. In 1956, Cooper demonstrated that if two electrons outside of the Fermi surface form a pair state, the system energy would be lowered by

$$\Delta E \approx -2\hbar\omega_D exp(-\frac{2}{V_0 D(E_F)})$$

where $\hbar\omega_D$ is a typical phonon energy, reflecting the belief that attraction between electrons occurs via electron–phonon interaction. This result is remarkable because it shows that such pairs will always have a lower energy than the normal ground state regardless of how small the interaction V_0 is. The most efficient way to write the Hamiltonian is using the notation of second quantization. Here $c_{k\sigma}$ and $c_{k\sigma}^\dagger$ are the electron annihilation and creation operators,

respectively, of the momentum k and spin σ. They are given as follows:

$$\{c_{k\sigma}, c^{\dagger}_{k'\sigma'}\} = \delta(k,k')\delta(\sigma,\sigma')$$

Thus, the proposed Hamiltonian can be written as

$$H = \sum_{k\sigma} \epsilon_k c^{\dagger}_{k\sigma} c_{k\sigma} + \sum_{kk'} V_{kk'} c^{\dagger}_{k\uparrow} c^{\dagger}_{-k\downarrow} c_{-k'\downarrow} c_{k'\uparrow}$$

It can be diagonalized using the Bogoliubov transformation. During this process, it is common to define an order parameter that is nonzero at low temperature but zero at high temperature; the definition naturally uses $\langle c_{k\uparrow} c_{-k\downarrow} \rangle$. A function called the gap function can also act as the order parameter in descriptions of the phase transition.

$$\Delta = -\sum_{k'} V_{kk'} \langle c_{k'\uparrow} c_{-k'\downarrow} \rangle$$

This will result in an important dispersion relation:

$$E_k = \sqrt{\epsilon_k^2 + \Delta^2}$$

E_k is the Bogoliubov quasiparticle energy in a paired superconductor, and Δ is the gap function. This equation states that the minimum 2Δ energy is required to break a Cooper pair. Thus, if we use $\gamma_{k\sigma}$ and $\gamma^{\dagger}_{k\sigma}$ as the annihilation and generation operators, respectively, for the Bogoliubov quasiparticle, and denote the bare vacuum state as $|0\rangle$, the ground state of the BCS superconductor is

$$|\Psi_0\rangle \propto \prod_{k\sigma} \gamma_{k\sigma} |0\rangle$$

The ground state energy will be

$$\langle \Psi | H - \mu N | \Psi \rangle = \sum_k (\xi_k - \frac{\xi_k^2}{E_k}) - \frac{\Delta^2}{V}$$

The condensation energy between the superconducting and normal states can be calculated as $\Delta E = -\frac{1}{2} N(0) \Delta^2$.

The gap function itself, under the mean field approximation, satisfies

$$\Delta_k = \frac{V}{2} \sum_{k'} \frac{\Delta_{k'}}{E_{k'}} tanh(\frac{\beta E_k}{2})$$

This is an equation that has gap functions on both sides. Depending on the situation, this equation can be simplified to evaluate the critical temperature either analytically or numerically.

From the BCS theory, at zero temperature, the gap function and critical temperature have the relation

$$\frac{2\Delta}{k_B T_c} \approx 3.53$$

The coherence length is

$$\xi(T) = \frac{\hbar v_F}{\pi \Delta(T)}$$

Near the critical temperature T_c, the gap function obeys

$$\frac{\Delta(T)}{\Delta(0)} \approx 1.74(1 - \frac{T}{T_c})^{\frac{1}{2}}$$

Thus, the coherence length can be simplified as

$$\xi(T) \sim |T_c - T|^{-\frac{1}{2}}$$

Thermodynamically, the heat capacity in the superconducting state obeys

$$C \propto exp(-2\beta\Delta)$$

Using the electronic entropy $S = -2k \sum_k [(1 - f_k) ln(1 - f_k) + f_k ln f_k]$ for a fermion gas and $C = -\beta \frac{dS}{d\beta}$, the BCS theory shows

$$\Delta C = C_{SC} - C_{normal}|_{T_c} = N(0)(-\frac{d\Delta^2}{dT})|_{T_c} \approx 9.4 N(0) k^2 T_c$$

This equation can also be written as

$$\frac{\Delta C}{\gamma T_c} \approx 1.43$$

CHAPTER 3

Experimental methods

3.1 Single crystal growth

A perfect single crystal is defined as a material with continuous crystal lattice and no grain boundaries. Most importantly, it allows for the measurement of intrinsic properties of materials. Unlike polycrystals, a single crystal only has one grain, which excludes the existence of impurity phases that are always embedded between grains in polycrystals. Besides impurities, the presence of a secondary phase is more annoying because of the difficulty to identify and separate it from the desired phase. Single crystal growth normally depends on a reliable recipe that is less likely to contain impurity phases. Even in that case, in most situations impurity phases can be separated from the single crystal by the differences in shape/color/size/crystallinity *etc.* Therefore, single crystal growth can provide samples with less strain, higher purity and fewer grain boundaries[CF01]. Single crystal samples are also necessary for the measurement of anisotropic properties, since they maintain their growth habit macroscopically. In addition, indirect use of the crystallinity is widely embedded within advanced measurement techniques, such as single crystal neutron scattering, angle resolved photoemission spectroscopy (ARPES), de Haas-can Alphen (dHvA) measurements *etc.* High quality single crystals are always critical for convincing results.

The most used synthesis method in my research is the high temperature solution growth method, which provides access to a wide variety of congruently and incongruently melting materials using relatively simple equipment and short time scales[CF01]. The high temperature solution growth method requires a glovebox or a working space for materials preparation,

a glass melting station for ampoule evacuation and sealing and a furnace (box or vertical tube). Arc melting of materials is also favored in the precursor preparation. Beyond the hardware requirement, the most critical factors that affect the results of a synthesis are solvent selection, initial concentrations and heating and cooling rates. Other possible factors are pressure, directions of ampoule, purity of precursors and starting amount.

The solvent, also called "flux", is vital for the success of single crystal synthesis. Generally speaking, an ideal flux would have a low melting point and vapor pressure, so that it could be in the liquid state during the synthesis. The target element set is expected to have high solubility in the flux and not form a stable secondary phase easily. Empirically speaking, Zn, Al, Ga, In, Ge, Sn, Pb, Sb and Bi are common first candidates for a trial synthesis. In addition to those elemental fluxes, an important type of solvent is the self-flux. Unlike the elemental flux, the self-flux does not introduce extra elements in terms of the target compound, in which case the number of possible secondary phases will be reduced. In the realm of iron based superconductors, the self-flux method is widely accepted and used to achieve large high quality single crystals. Although empirical binary and ternary phase diagrams are likely to contain information on how to choose the solvent and starting concentration, the true parameters of the recipe have to be determined experimentally. The cooling rate is important for the size of sample. A slower cooling rate is always associated with relative larger samples, in which less strain is expected as well. Once adequent single crystals have formed, they are typically filtered out at the decanting temperature. This temperature needs to be above a certain value so that the solvent remains in its liquid phase and impurity phases are less likely to be present. On the other hand, it is also expected to be a value as low as possible because low temperature always means lower solubility and a greater yield of crystals. The last and most important point I'd like to emphasize about the synthesis of iron based superconductors is the purity of precursors, especially in the synthesis of the 112 compounds, as even little oxidization of FeAs or CaAs will result in a corrupted growth. The detailed synthesis recipes will be explained in the corresponding chapters.

3.2 Measurement methods

3.2.1 X-ray diffraction methods

X ray diffraction is a powerful method for phase identification. X-ray diffraction data are always collected in our lab once crystals are obtained from a new recipe. Based on a good powder X-ray diffraction pattern, the main phase can be identified if it matches a known phase in the database. This also applies to any possible impurity phases."Good" X-ray diffraction data are obtained from well-prepared sample powders, which are supposed to be ground very finely so that the grain size is small. In addition, the sample holder should have a thin and flat layer of powder to reduce possible zero shift. The disadvantage of the powder x-ray is that it is not very sensitive to impurities that have very limited concentration.

Besides phase identification, a more careful measurement on a sample can give us more accurate information about the space group, the lattice constants, and even the atomic coordination of the atoms. This information is valuable, especially when it is used to refine a new structure that has not been recorded inside commercial databases. Normally, the space group and the lattice constants can be refined from the position of the Bragg peaks, while detailed atomic coordinates need careful refinement on a whole set of peak profiles through a series of operations using the software"FullProf". Occasionally, the results of a refinement are not satisfactory due to low sample quality. For iron-based superconductors, an alternative approach is to measure the X-ray pattern of a plate-like single crystal. This allows us to estimate the FeAs interlayer distance in order to evaluate the lattice constant. This method is also very effective for crystals with low symmetry groups such as the monoclinic structure. The software "UnitCell" is used for this type of refinement. More detailed examples can be found at later chapters.

3.2.2 Wavelength dispersive specstroscopy

Wavelength-dispersive X-ray spectroscopy(WDS) is a powerful method for measuring the element concentrations in a sample. The sample is bombarded by electrons and the detector counts the number of x-rays of a specific wavelength diffracted by a reference crystal. Compared to energy dispersive spectroscopy, which is detecting direct x-rays that are emitted by the sample, WDS measures wavelengths that have been diffracted a second time. Thus, it can largely enhance the elemental resolution, not to mention that the count rate is much higher than EDS for the same system. These advantages result in a resolution of $\sim$0.01% of weight percentage while EDS normally reaches $\sim$0.1%, especially for light elements such as Be, B, C, N, O and F. The only disadvantage would be that for a measurement of a specific element set, WDS usually requires a pre-test to select a proper wavelength range and measurement resolution to decide the most efficient reference crystal and sample standard. This pre-test could increase the measurement time significantly in some "notorious" element combinations.

In terms of my research, elemental analysis is crucial in order to link the real concentration to its physical properties. Thus, WDS measurements were usually performed for the same pieces which were used for other measurements. In addition, multiple dot measurements on the same pieces at different layers (if possible) were performed to estimate the average concentration and concentration variation, as a metric to indicate the doping homogeneity. Besides detecting secondary electrons that could indicate the element concentration, using the backscattered electron mode can yield an image whose pixel intensity is proportional to the local atomic number. This mode is usually applied to test the existence of a secondary phase if the sample either has a flat surface or is polished. More detailed measurement results can be found at later chapters.

3.2.3 Transport measurement

3.2.3.1 Resistivity and Hall coefficient measurement

Resistivity and Hall coefficient measurements are the most common transport measurements to determine the sample resistivity, carrier type(s) *etc.* The temperature dependent resistance measurement is fulfilled with a Quantum Design (QD) Physical Properties Measurement System (PPMS) using the resistivity option. A platelike sample is either cleaved or polished to have a rectangular shape with uniform thickness. This typical resistivity bar is assembled with four (R or Hall measurement individually) or six (R and Hall combined measurement) platinum wires using Epotek H20E silver epoxy. A tiny amount of current is favored in order to minimize the heat generated at low temperature to maintain the temperature homogeneity. For large resistance measurements the two wire setup can be used. For

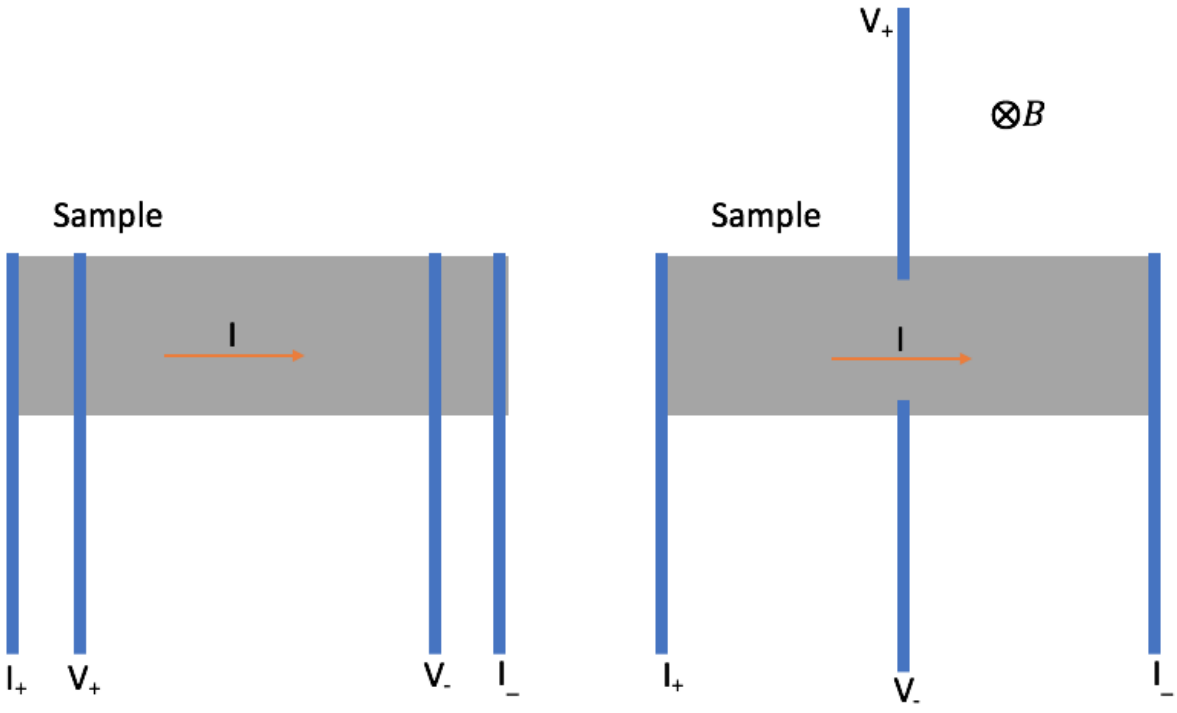

Figure 3.1: Left: The configuration of the four probe resistivity measurement. Right: The configuration of the Hall measurement.

Hall measurements, in order to extract the intrinsic sample contribution, thinner samples are preferred. In principle, an ideal sample should have a surface area of at least $2mm^2 \cdot 2mm^2$. But experimentally, this is not always the case. Thus, more attention needs to be spent on the middle pair of wires. Firstly, the separation of the two wires should be as wide as possible so the effective width would be as close as the sample width. Secondly, the two wires are supposed to be aligned as much as possible so that no drift signal is introduced in the voltage measurement.

3.2.4 Magnetization measurement

The magnetization measurements are performed at a QD Magnetic Properties Measurement System (MPMS) up to magnetic fields of $\pm$ 7T in a temperature range from 1.8K to 400K. For superconducting samples, samples of a few milligrams can give a large diamagnetic signal. Zero-field-cooled(ZFC) and field-cooled(FC) are typical methods to measure the superconducting volume fraction, especially for Type-II superconductors. The field value needs to be selected carefully based on the extent of critical temperature drop when the field is applied. It needs to be large enough to extract the superconducting signal over the random noise, but should not depress the critical temperature too much. This tiny amount of field will strictly require minimal amount of remnant magnetic field, which could be achieved by oscillating the magnetic field to zero using a monotonically decreasing amplitude. A thin plate whose surface is parallel to field direction is favored in order to minimize the effect of demagnetizing fields. If that is not the case, a correction needs to be made to calculate the intrinsic superconducting volume fraction.

Measuring magnetic susceptibilities, especially in direction-dependent measurements, always requires a new design of the measurement apparatus with the sample holder in an appropriate direction. It is always recommended to test the noise introduced by a new medium used in a new setup. It has to be stable throughout the entire temperature range and be as minimal as possible. Detailed data can be found at later chapters, especially chapter 5.

3.2.5 Specific heat measurement

Temperature dependent heat capacity measurements are also performed in a PPMS with field ranging from 0T to 9T and temperature ranging from 1.8K to 400K. The sample mass is more important in this measurement and should ideally be above 5mg. Sample(s) are attached to the platform of the HC measurement holder using N grease. The amount of N grease should not be too much to avoid a large background. A good measurement will require a well calibrated sample puck at both cases: with or without field, especially at low temperature.

3.2.6 Muon spin relaxation

Muon spin relaxation(μSR) is a method of using the muon's spin to look at structural and magnetic properties in the bulk of a material. Generated by high energy protons hitting a target of carbon or beryllium, $\sim 100\%$ spin-polarized muons are transported down the beam line to the sample being studied. Once the muon decays, it emits a fast decaying positron preferentially along the direction of its spin.

$$\mu^+ \rightarrow e^+ + v_e + \bar{v}_\mu$$

However, the local magnetic field will cause the muon spin to precess around the direction of the magnetic field, thus changing the direction of the positron. By measuring the anisotropic distribution of the time evolution of the decayed positron, it could statistically determine the time evolution of its average spin direction. Notably, the asymmetry is $\frac{1}{3}$ when all position energies are detected with equal probability. On the other hand, the precession frequency only depends on B_{local}.

In experiments, muons are transported into the crystals and trapped later by local electric fields. However, the precession of the muon spin is only affected by the local magnetic field. Thus, by looking at the time evolution at different temperatures, if any magnetic phase transition or superconducting phase transition takes place, the different magnetic environment will lead to a change in the asymmetry time evolution pattern. Thus, it is an

important technique can be used to reveal information about phase transitions. Zero-field muon spin relaxation in particular is ideal for the detection of weak internal magnetism that arises due to an ordered magnetic phase, or random fields that are static or dynamic. A detailed understanding of data will require a carefully selected model, which should be able to match the experimental data but also explain the physics behind it, such as the very famous Kubo-Toyabe function that explains substances with nuclear magnetic moments[HUI79].

3.2.7 Elastic neutron scattering measurement

Neutron scattering is a technique used to determine the positions and motions of atoms in condensed matter physics since they have wavelengths comparable to the interatomic spacing in solids. In addition, due to their limited interaction only with nuclei and electron spins, they can penetrate farther inside the sample compared to electrons or x-rays. Further, neutrons have the right energy and momentum transfer to investigate both structure and dynamics in condensed matter physics. Although a relatively large amount of sample is required, elastic neutron scattering is a very effective method for structure refinement and magnetic structure determination.

Compared to the μSR technique, neutron scattering is able to detect magnetic fluctuations ranging between $10^8 Hz$ to $10^{13} Hz$ while μSR is able to measure from $10^4 Hz$ to $10^{12} Hz$. In terms of magnetic phase transitions, although both methods can give information about the phase transition temperature, μSR is better for the determination of the phase transition since it is extremely sensitive to small internal magnetic fields($\sim$0.1G), but only elastic neutron scattering can give the detailed magnetic structure from data refinement as well as the absolute value of moment size. As for the magnetic volume fraction, this can only be extracted from μSR data. In some cases, if the material strongly absorbs neutrons, μSR can be used as an alternative. This is typically the case for liquids. In terms of sample requirement, both techniques can be used with single crystals and polycrystals, but the amount of sample required varies depending on the research goal.

In my research, neutron scattering was first used to determine the magnetic structure of CaLa112. It was also used to determine the structural and magnetic phase transition temperatures of Ce112, Pr112, Nd112 and Cobalt doped 10-3-8 series by measuring the order parameters. Detailed results can be found at chapters 4-7.

CHAPTER 4

Microscopic, transport, and thermodynamic properties of $Ca_{10}(Pt_3As_8)[(Fe_{1-x}Co_x)_2As_2]_5$ single crystals

4.1 Introduction

Since the discovery of high temperature Fe based superconductors (FBS) in F doped LaFeAsO in 2008, a dozen of new FBS were discovered. Most of them, such as $BaFe_2As_2$ and FeSe, crystalize in known crystal structures; only a couple of them were discovered with a brand new crystal structure, bringing in structural complexity. The so-called 10-3-8 compound with the stoichiometric formula $Ca_{10}(Pt_3As_8)(Fe_2As_2)_5$ belongs to the family of $Ca_{10}(T_nAs_8)(Fe_2As_2)_5$ (n = 3,4 and T = Pt, Pd, Ir) compounds discovered in 2011. The stacking of -Ca-(Pt_nAs_8)- Ca-(Fe_2As_2)- with the skutterudite Pt_nAs_8 spacer layers and dozens of ions in one unit cell give rise to the structural and chemical complexity. The parent compound of the 10-3-8 family, $Ca_{10}(Pt_3As_8)(Fe_2As_2)_5$ shows a triclinic to triclinic structural phase transition at 110(2) K and a paramagnetic to stripe-like antiferromagnetic ordering at T_N = 96(2) K. Partial substitution of Fe sites with Pt, Co or Ni[KKN11, NAC11, LST11, SDJ12, TDT13, CTK12, XLY12, DTS12], partial substitution of Ca with La[SDJ12, NSW13, KSJ13] and the application of external pressure[GSN14] can suppress the structural/magnetic phase transitions and induce superconductivity (SC). The interplay among various competing orders always lies at the heart of the study of high temperature superconductors because it can provide profound insight on the pairing mechanism. Although temperature-concentration and temperature-pressure phase diagrams were

mapped out for the 10-3-8 families, to clarify if there is phase coexistence or separation of antiferromagnetism (AFM) and SC faces serious difficulties and needs further investigation. Accidental Pt doping on Fe sites makes it hard to synthesize a pure parent compound and blurs the effect of other dopants[NAC11] on the appearance of SC; moreover, inhomogeneous doping may result in measurements with misleading information[XLY12]. Therefore, single crystal growths and characterization of a well controlled 10-3-8 doping series is needed. In this chapter, we report a systematic study of a series of high quality Co-doped 10-3-8 single crystals. With Co doping, both the structural and magnetic phase transition temperatures are suppressed. Superconductivity is stabilized in a dome-like region in the temperature-concentration phase diagram. Through a combination of transport, thermodynamic and elastic neutron scattering experiments, we conclude that no phase coexistence of AFM and SC exist in Co doped 10-3-8. The fact that no phase coexistence in Co-doped 10-3-8 provides new insight in understanding the interplay of AFM and SC in FBS. In chapter 6, by comparing the phase diagrams of the Co-doped 10-3-8 and Co-doped CaLa112, we suggest the effect of the interlayer coupling in the extent of phase coexistence in FBS. Furthermore, using the optimally doped sample ($x = 0.112$) as the representative, we studied the superconducting properties of Co-doped 10-3-8.

4.2 Experimental results and discussion

4.2.1 Single crystal growth and characterization

High-quality single crystals of $Ca_{10}(Pt_3As_8)[(Fe_{1-x}Co_x)_2As_2]_5$ were synthesized by the CaAs-rich self-flux method. Precursors of CaAs, FeAs, and CoAs in powder form and Pt powder (Alfa Aesar, 99.9%) were thoroughly mixed at a nominal ratio of 3.5:2 $-x$:x:0.4, pressed into a pellet, placed in an alumina crucible, and sealed in a quartz tube under vacuum. The pellet was then heated to 1100 °C at 180 °C/h, held for 72 h, and cooled to 885 °C at 5 °C/h. Water quenching was then applied. After the half-melted pellet cooled to room temperature, it was rinsed in an ultrasonic water bath, and typical $4 \times 4 \times 0.5$ mm^3 shiny platelets were

obtained, as shown in the inset of Figure 4.2. Comparing with the Pt doped and La doped 10-3-8 compounds, the Co doping resulted in much larger single crystals.

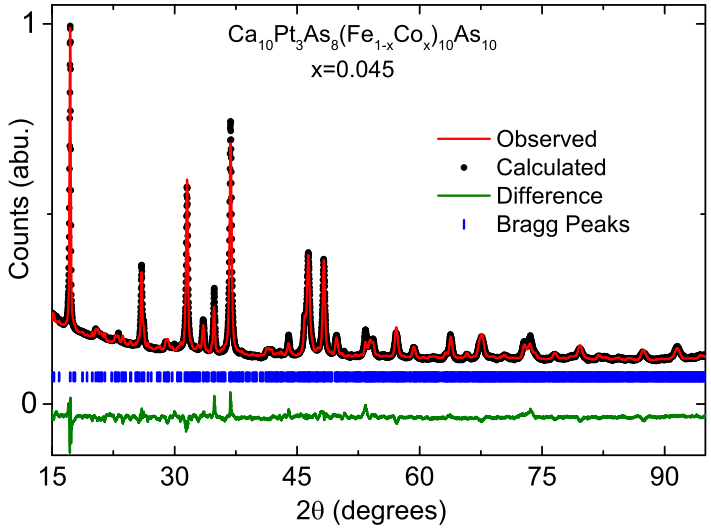

Figure 4.1: Powder XRD data and the FullProf refinement of $Ca_{10}(Pt_3As_8)[(Fe_{1-x}Co_x)_2As_2]_5$ with $x = 0.045$. Black dots and red curve are the experimental data and refinement result, respectively. Short blue vertical bars indicate the the Bragg peak position. Green line below shows the refinement differences between the calculated and experiment patterns. No impurity peak is observed.

Elemental analysis was performed using wavelength dispersive spectroscopy (WDS) on multiple representative crystals selected from each batch. We have to point out that to carefully determine the revolution of structural and physical properties with Co doping, pieces with known concentrations were selected to perform various measurements. Using a PANalytical Empyrean diffractometer (Cu Kα radiation), powder X-ray diffraction was collected. The doping dependent FeAs interlayer distance at room temperature was determined by scanning the (00l) peak diffraction pattern of pieces with uniform thickness and flat shiny surfaces. The data were refined with the Unit Cell software[HR97]. In-plane electrical transport, Hall

coefficient and heat capacity data were collected for pieces measured by WDS in a Quantum Design Dynacool PPMS system. The magnetic susceptibility data were measured on pieces measured by WDS in a Quantum Design VSM MPMS3 system.

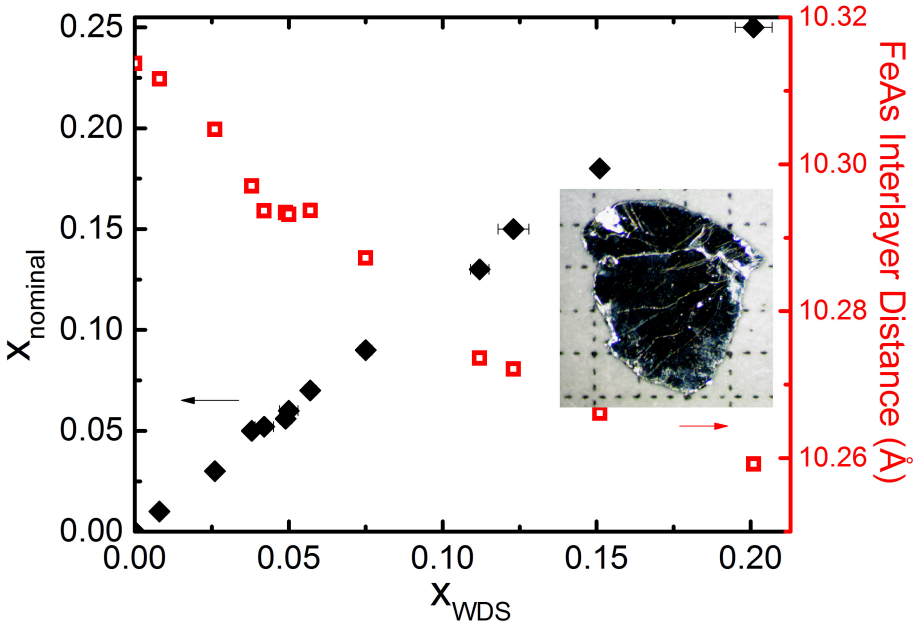

Figure 4.2: The x_{nominal} vs. x_{WDS} and the evolution of the FeAs interlayer distance d with x_{WDS}. The variance of x in each piece is very limited. Inset: image of a single crystal against 1 mm scale.

To identify the phase, room-temperature powder XRD data for the 10-3-8 batch with a real Co doping level of 0.045 Co were obtained. Using the Rietveld refinement, the data can be well refined in the space group P-1 with the 10-3-8 crystal structure, shown in Fig. 4.1, which gives $a = 8.7524$ $\mathring{A}$, $b = 8.7528$ $\mathring{A}$, $c = 10.6557$ $\mathring{A}$, $\alpha = 94.5851°$, $\beta = 104.2121°$, and $\gamma = 90.1062°$. No detectable impurity phase, in particular no 10-4-8, is observed. The WDS measurements are summarized in Fig. 4.2. Firstly, although to some extent, Co dopant concentration shows piece to piece variance in each batch, but from Fig. 4.2 where each black data point represents the average Co dopant concentration with uncertainty measured

by WDS on one piece, we can see there is a very limited concentration variation on each piece, suggesting a highly homogeneous doping level in each piece in the concentration range we studied. Henceforth, x denotes the actual concentration from the analyzed WDS data. Secondly, our WDS measurements show the Pt concentration is almost unchanged across the entire Co doping range. Thirdly, the actual Co dopant concentration measured by WDS exhibits an essentially linear relationship with the nominal concentration, giving the ratio of $\frac{X_{WDS}}{X_{nominal}} \approx 0.8$. Figure 4.2 also shows the linear relationship between the FeAs interlayer distance which is extracted from the (00l) XRD data and the WDS Co concentration. Note that the interlayer distance decreases monotonically as the dopant concentration increases, in contrast to the behavior of both La- and Pt-doped series[NSW13][XLY12], where doping yields an increasing interlayer distance, owing to the radius difference of the dopants. This is consistent with the Co doped series in other FBS, which always decreases the FeAs interlayer distance with doping.

4.2.2 The suppression of the structural/magnetic phase transitions

The tendency toward easy exfoliation is quite prominent in 10-3-8. Therefore, to avoid the error in resistivity due to the large geometry uncertainty, the in-plane temperature-dependent normalized resistance $R/R(300K)$ (RRR) of $Ca_{10}(Pt_3As_8)[(Fe_{1-x}Co_x)_2As_2]_5$, rather than its resistivity, is summarized in Fig. 4.3. Unlike the resistivity of all other iron pnictide parent compounds, which show poor metallic behavior, the RRR of the 10-3-8 parent compound ($x = 0$) increases along decreasing temperature with a slope change around 110 K, indicating semiconductor-like behavior. The doping process effectively suppresses the upward trend, and the RRR indicates metallic behavior at higher doping levels. Anomalies in the RRR are observed for samples with low doping concentrations. With Co doping, the anomalies are suppressed to lower temperatures. This feature can be more clearly seen in the derivative of RRR, d(R/R(300K))/dT, as shown in the lower panel of Fig. 4.3. According to previous elastic neutron and X-ray scattering reports[STR14], the parent 10-3-8 compound undergoes a triclinic to triclinic structural phase transition at $T_s = 110(2)$ K and a paramagnetic to

stripe-like AFM phase transition at $T_m = 96(2)$ K. However, even in our $d(R/R(300K))/dT$ plot, we can only identify one-kink feature with unknown nature. As a result, we can not separate these two transitions in the way for other FBS, where two-kink feature was observed. Therefore we will only refer the peak temperature indicated in 4.3 as $T_{s/m}$. Based on the previous neutron and transport study of the parent compound [STR14], this value is likely to be smaller than the T_s but larger than T_m. With regard to these magnetic samples, the $T_{s/m}$ temperatures can be determined for the $x = 0$, 0.0085, 0.027 and 0.038 samples. No detectable anomalous features were observed in RRR for samples with doping levels of $x = 0.05$ or higher whereas zero resistance emerges at $x = 0.05$ with a T_c offset temperature at approximately 8 K.

The temperature-dependent Hall coefficients of Co-doped 10-3-8 at $x = 0$, 0.0085, 0.050, 0.057, 0.112 and 0.151 are summarized in Fig. 4.4. Over the entire temperature range, the Hall coefficient at each doping level remains negative, indicating that electrons are the dominant carriers in this multiband system. In addition, the absolute value of R_H decreases with increasing doping level x at the same temperature. This is consistent with the scenario in which the dopant Co adds extra electrons to the system. Note that the temperature corresponding to a sudden change in the slope of R_H in the non-SC samples ($x = 0$ and 0.0085) matches the structural and magnetic phase transition temperature inferred from transport measurement. This change is likely attributed to a gap opening at the spin-density-wave(magnetic) phase transition that reduces the density of states at the Fermi level[DZX08]. No clear sudden change in R_H is detected for other dopings we measured, as shown in the inset of Fig. 4.4.

4.2.3 Physical properties of the superconducting state

Figure 4.5 shows a close-up view of the $Ca_{10}(Pt_3As_8)[(Fe_{1-x}Co_x)_2As_2]_5$ series in the SC state. The top panel is the expanded portion of the in-plane RRR data based on Fig. 4.3, and the bottom panel shows the FC and ZFC data measured by applying a 5 Oe magnetic field parallel to the sample ab plane. For the $x \leq 0.038$ samples, neither zero resistance nor

zero diamagnetism signal is observed. At $x = 0.05$, the RRR data drops sharply to zero accompanied with a significant diamagnetism signal at the critical temperature of $T_c = 8$ K. With increasing Co substitution, the T_c gradually increases, reaching the optimal $T_c = 13.5$ K at $x = 0.112$. The overdoped region is subsequently built up, and SC is observed until $x = 0.202$ with a $T_c = 3$ K, which is the highest concentration we could obtain. Diamagnetism signals are observed over the full range of $x = 0.05$-0.202. Although the transition is slightly broader than that of electron-doped Ba122[NTY08] and the newly discovered Co-doped CaLa112[JLS16], the ZFC data refers to large shielding effect, confirming the bulk superconductivity in these compounds. In addition, the small Meissner fraction indicates strong flux pinning, like that in other Fe pnictides.

To better investigate the SC state, the optimal $x = 0.112$ sample is taken as a representative sample. Figure 4.6(a) shows the heat capacity of the $x = 0.112$ sample. A clear heat capacity jump appears at $T_c = 13.0$ K with $\Delta C_p/T_c = 10mJ/mole \cdot K^2$ as scaled to one Fe_2As_2 unit per formula. This value sits well in the plot of the BNC scaling[BCB14], suggesting that the pairing symmetry is $s^{\pm}$. Figures 4.6(b) and (c) show the upper critical fields H_{c2} measured with $H \parallel ab$ and $H \perp ab$. T_c is suppressed with increasing field. Using the 50% criterion shown in Fig. 4.6(b), the measured $H_{c2}^{\parallel}ab$ and $H_{c2}^{\perp}ab$ are plotted in Fig. 4.6(d). An almost linear field dependence deviating from the single band Werthamer-Helfand-Hohenberg (WHH) theory is observed, consistent with its multiband superconductivity nature. The obvious broadening of the SC transition under high magnetic field may be due to the short coherence length ξ and low dimensionality[MLT03]. The anisotropy parameter $\gamma = H_{c2}^{\parallel}/H_{c2}^{\perp}$ has a maximum around 8 at 13.7 K, which is much larger than that of the well-studied 122 family [NTY08], indicating much weaker interlayer coupling in the 10-3-8 system.

The anisotropy parameter can be gauged more precisely by measuring the angle dependence of the melting field $H_m = H/(sin^2\theta + \gamma^{-2}cos^2\theta)^{\frac{1}{2}}$[BGL92]. For the $x = 0.112$ sample, the resistance was measured at 11 K under 1 T while the sample was rotated at various angles.

We then repeated the measurement at various fixed field ranging from 1 to 9 T in 1 T steps. Figure 4.6(e) summarizes the resistance curves versus the H_m. To get the best scaling, an anisotropy parameter of $\gamma = 8$ is chosen to collapse the data on a universal curve. Figure 4.6(f) shows the data in red and blue to indicate data taken under fields below or above 3 T, respectively. Close examination of the scaled curves indicates that the red group is better scaled at low H_m, whereas the blue group is better scaled at higher H_m. By increasing the fitting parameter γ, the blue group becomes more confined at high H_m, but the red group begins to diverge, and vice versa. This difference allows us to estimate the uncertainty of the fitting as $\delta\gamma = \pm 0.5$. In addition, the different behavior of these two groups indicates that the system exhibits a strong multiband effect. The γ value of $\sim$8 matches well with the one obtained from the H_{c2} measurement and is similar to those of Pt-doped 10-3-8 ($\Gamma \approx 10$)[LST11] and 1111 ($\Gamma \approx 7 \sim 8$)[PPB10], but higher than that of the well-studied Ba122 family ($\Gamma \approx 2 \sim 4$)[TNM09]. This result demonstrates that the 10-3-8 family is among one of the most anisotropic Fe pnictides.

4.2.4 Phase separation of antiferromagnetism and superconductivity

The resistivity data and Hall coefficient measurements both show that for samples showing superconductivity, neither a structural nor a magnetic phase transition can be detected by our transport measurements, suggesting the possible phase separation of AFM and SC. To investigate this in details, an elastic neutron scattering experiment was conducted on samples with concentrations near the phase boundary between the AFM zone and the SC dome. The $x = 0.038$ sample shows no SC while the 0.045 sample shows 80% of shielding fraction at 2 K, as shown in the inset of Fig. 4.7. The order parameter data were collected by measuring the (2 2 0) peak intensities in a wide temperature range. For the $x = 0.038$ sample, below 120 K, the intensity decreased gradually to 70 K; then the peak intensity dropped sharply from 70 to 45 K, where the peak intensity started to increase with decreasing temperatures. This change in the slope suggests that the structural phase transition occurs at 70 K while the magnetic phase transition appears at 45 K. The slow decrease in the peak intensity from

110 to 67 K may be related to short-range structural distortions while the increase below 45 K is likely resulted from the change in the (2 2 0) structural factor caused by the appearance of magnetic order. The determined T_s of 70 K and T_m of 45 K are consistent with data from our transport measurement where the peak of the kink feature in $d(R/R(300K))/dT$ is around 65 K. However, the features showing in Fig. 4.7 (a) are all absent for the $x = 0.045$ sample, as seen in Fig. 4.7 (b). This solid evidence strongly suggests that within our experimental resolution, the AFM zone and the SC dome do not overlap.

Combining the transport, thermodynamic, and neutron scattering data, we can map out the 10-3-8 temperature–concentration phase diagram in Fig. 4.8. With the Co doping, the structural/magnetic phase transitions in the parent 10-3-8 compounds were suppressed to lower temperatures. With more Co doping, superconductivity up to 13.5 K can be induced in an extended doping region between $x = 0.045$, the lowest concentration where 80% of shielding fraction was observed at 2 K, and $x = 0.202$, the highest concentration we can reach. Within our doping resolution near the AFM and SC phase boundary, based on our low field susceptibility and neutron scattering measurements on the non-SC $x = 0.038$ piece and the SC $x = 0.045$ piece with 80% of shielding fraction at 2 K, we conclude no detectable phase coexistence exists at the phase boundary. This behavior is remarkably similar to that of the $LaFeAsO_{1-x}F_x$[LKK09] and high-T_c cuprates[FKK03]. Interestingly, in contrast to our findings and those on F-doped LaFeAsO[ZHC08a], it has been shown that no phase coexistence of AFM and SC appears in F-doped CeFeAsO. On the other hand, the microscopic coexistence of AFM and SC in the underdoped regime in F-doped SmFeAsO has been reported[DNB09]. It is notable that the 10-3-8 family shows high anisotropy while the REFeAsO (RE = La, Ce, Sm) has an anisotropy parameter γ of 7–8 for RE = La[PPB10], 2–4 for RE = Ce[SWS10], and 2–3 for RE = Sm[SFC08]. The evolution of γ and the extent of the phase coexistence phase diagram suggest that the electronic anisotropy affects the phase competition mechanism.

4.3 Conclusion

In summary, we carefully mapped out the temperature–concentration phase diagram of $Ca_{10}(Pt_3As_8)[(Fe_{1-x}Co_x)_2As_2]_5$ from a combination of transport, thermodynamic, and neutron scattering experiments. Based on the data obtained on homogeneously doped single crystals with WDS measured dopant concentrations, the structural/magnetic phase transitions in the parent 10-3-8 phase were suppressed with Co doping and bulk SC was induced in an extended dome like region. Within our concentration resolution at the AFM and SC phase bounder, no phase coexistence of AFM and SC was detected, indicating phase separation scenario. By comparing with the phase diagrams of the other FBS, we tempt to argue the importance of the electronic anisotropy in affecting the interplay of AFM and SC.

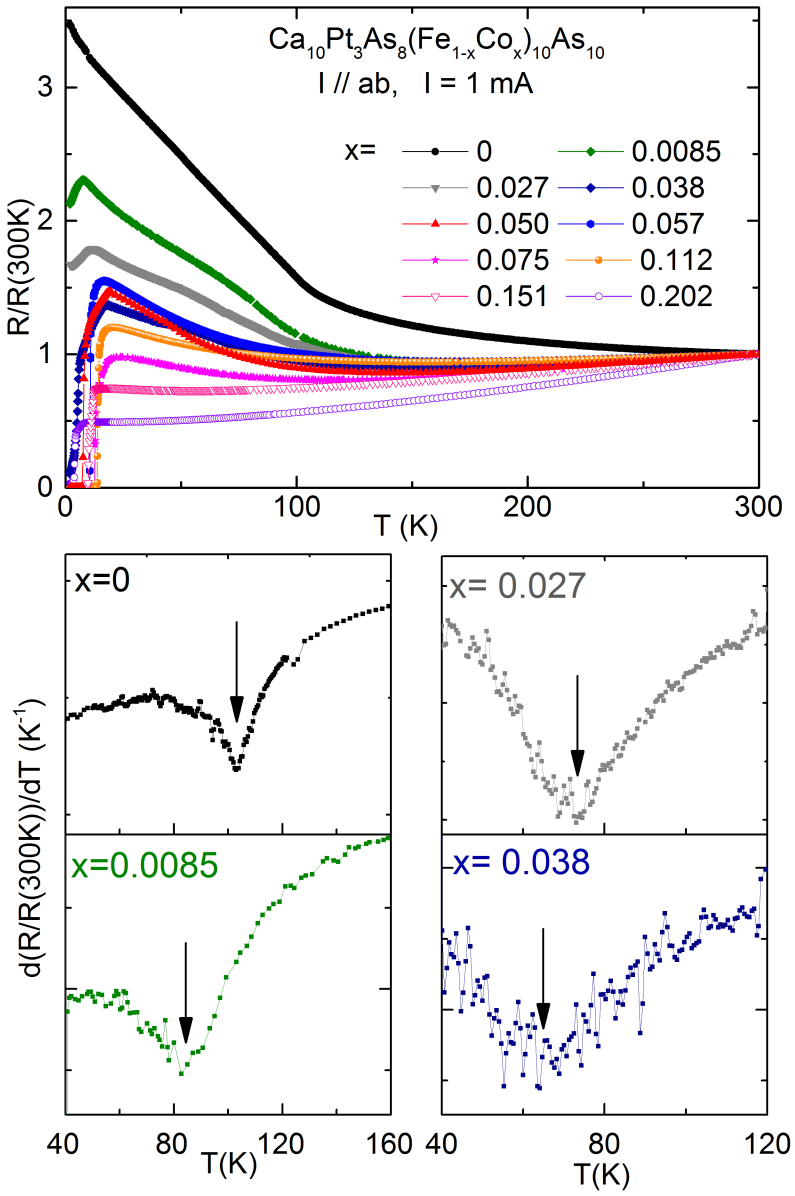

Figure 4.3: Top: Temperature-dependent R/R_{300K} of $\mathrm{Ca}_{10}(\mathrm{Pt}_3\mathrm{As}_8)[(\mathrm{Fe}_{1-x}\mathrm{Co}_x)_2\mathrm{As}_2]_5$. Bottom: $\mathrm{d}R/\mathrm{R}_{300K}/\mathrm{d}T$ vs. T. The kink feature indicates the structure and magnetic phase transition.

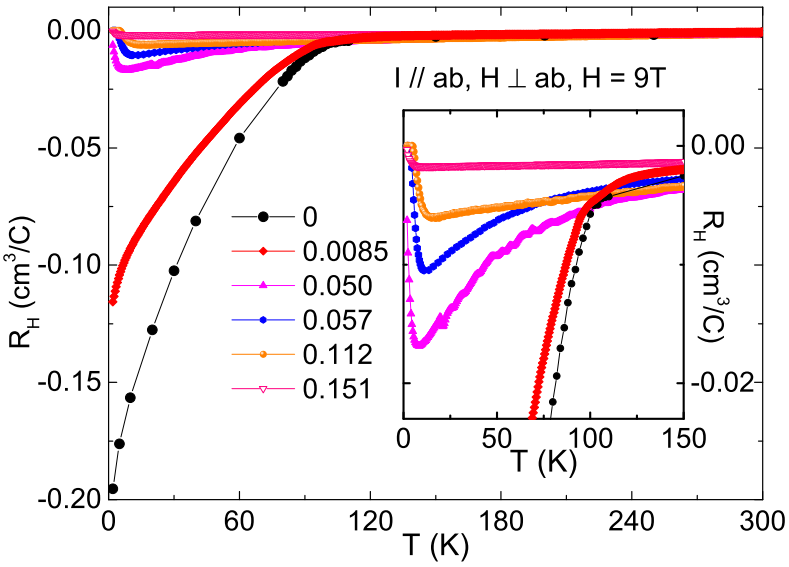

Figure 4.4: Temperature-dependent Hall coefficient of $Ca_{10}(Pt_3As_8)[(Fe_{1-x}Co_x)_2As_2]_5$. Inset: The closeup look at low temperatures.

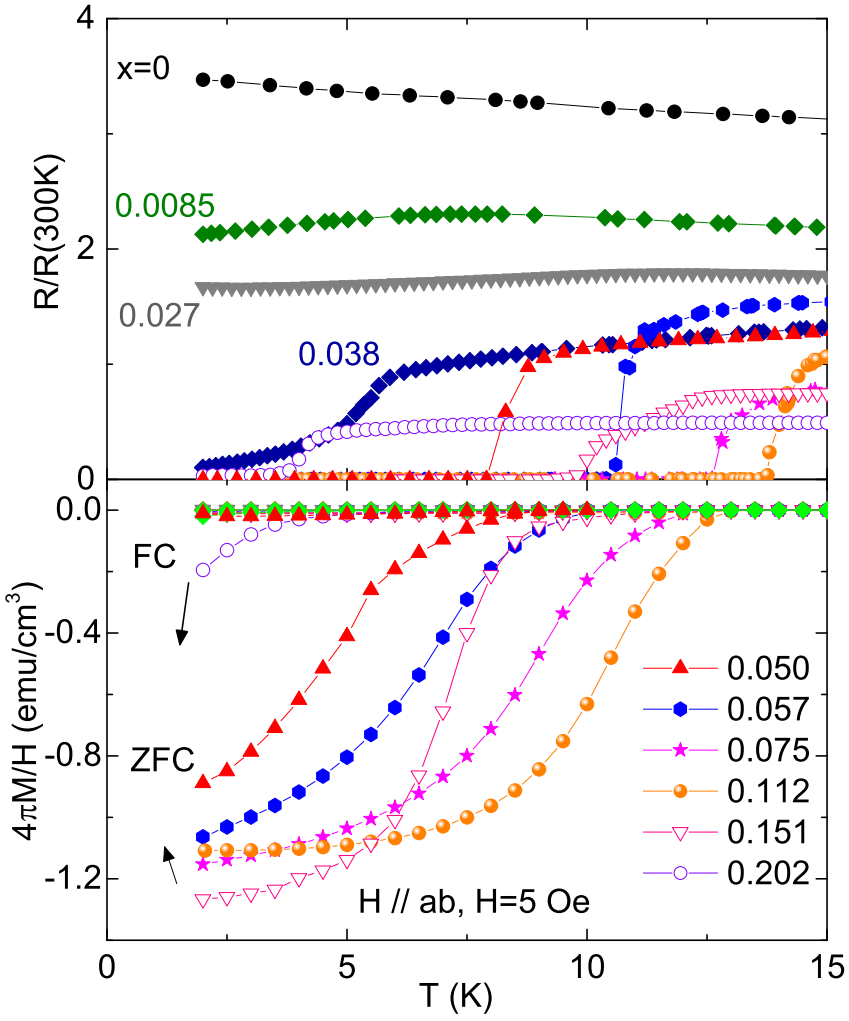

Figure 4.5: $Ca_{10}(Pt_3As_8)[(Fe_{1-x}Co_x)_2As_2]_5$: Top: The closeup look of the R/R_{300K} at low temperatures. Bottom: Temperature dependent FC and ZFC susceptibility data taken at 5 Oe with H // *ab*.

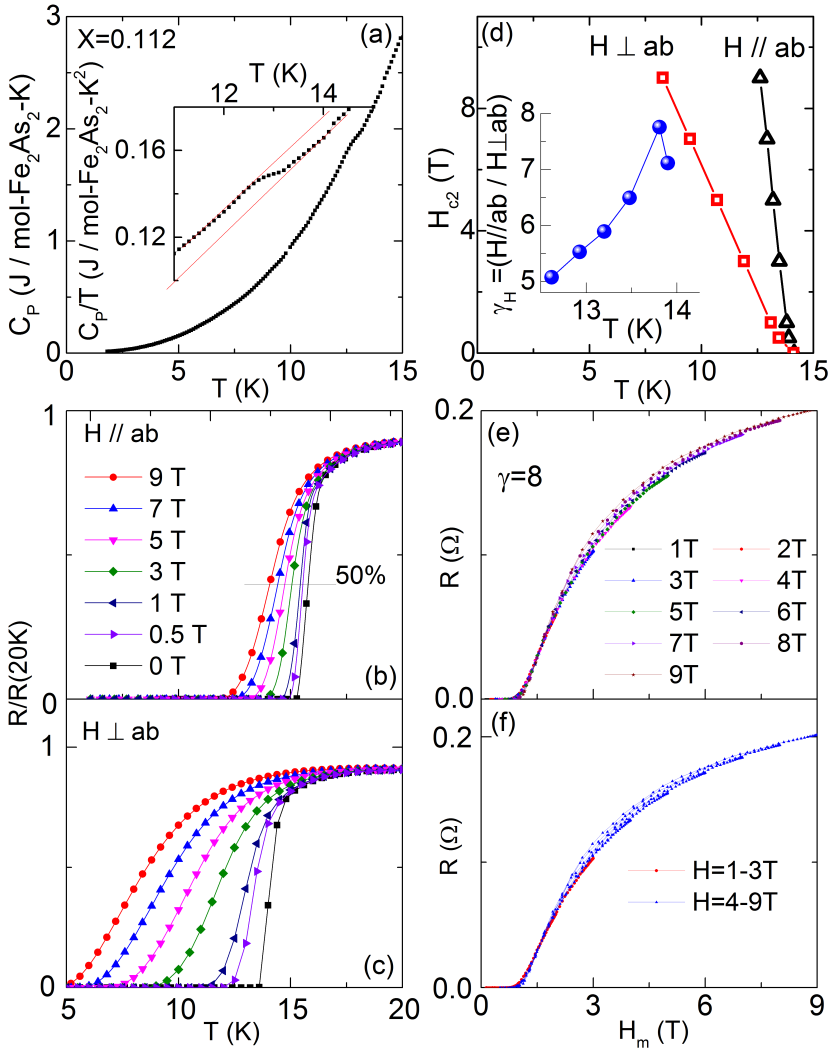

Figure 4.6: (a): C_p vs. T of the optimally doped sample (x=0.112). Inset: C_p/T vs. T. ΔC_p is clearly seen in the inset. (b) and (c): Anisotropic H_{c2} measurements of $x = 0.112$ sample measured at various external field. The 50% R criterion is used to determine T_c. (d) H_{c2} vs. T. Inset: Anisotropy parameter γ vs. T. (e): R vs. melting field H_m, see text. (f): R vs. melting field H_m, see text. Data grouped into a red group with fields of 1, 2, and 3 T and a blue group with a field larger than 3 T.

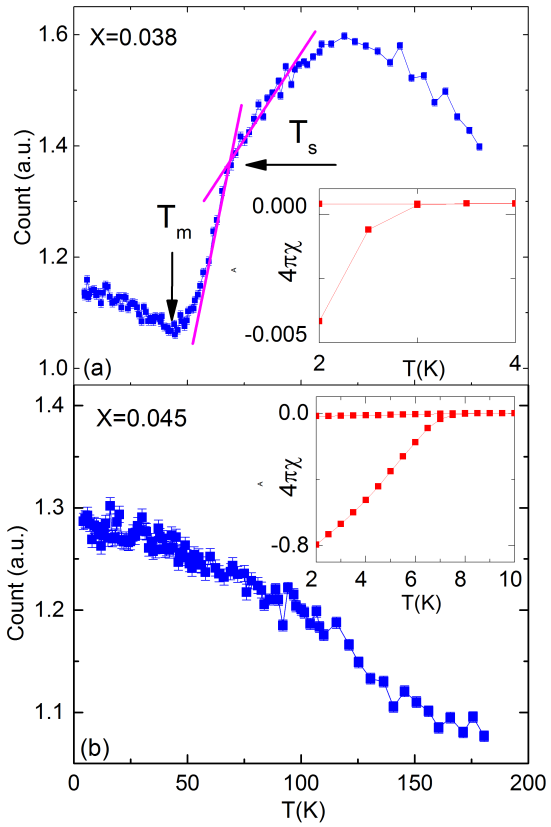

Figure 4.7: Order parameter measurements centered at the (2 2 0) nuclear peak for (a) $x = 0.038$ and (b) $x = 0.045$ samples. The criteria to infer structural phase transition temperature T_s and magnetic phase transition temperature T_m are indicated. Inset: Temperature dependent FC and ZFC susceptibility data taken at 5 Oe with H // *ab*.

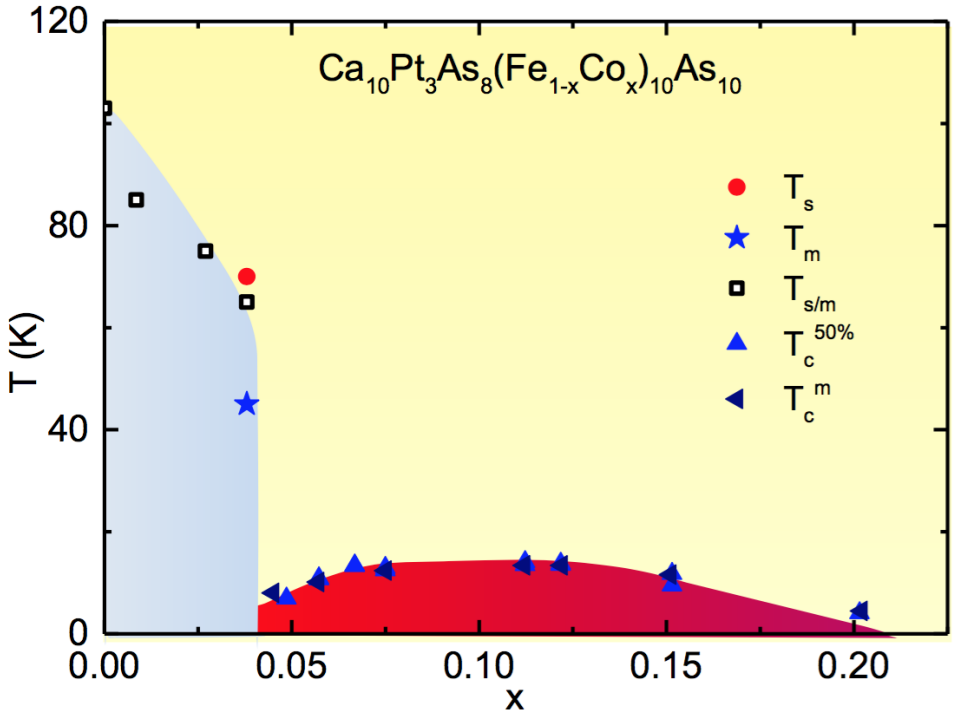

Figure 4.8: The temperature–concentration phase diagram of $Ca_{10}(Pt_3As_8)[(Fe_{1-x}Co_x)_2As_2]_5$.

CHAPTER 5

Structural and magnetic phase transitions in non-superconducting $Ca_{0.73}La_{0.27}FeAs_2$

5.1 Introduction

As we introduced in Chapter 1.3, a few compounds containing As/Sb layers and alternating prototypical FeSb/FeAs layers were theoretically proposed to be candidates of high temperature superconductors. However, none of them has been able to be experimentally synthesized. It was not until the end of 2013, Naoyuki Katayama *etc.*[KKO13] discovered that a small substitution of La on Ca site managed (CaLa112) to stabilize the crystal structures and superconductivity($T_c \approx$40K) was induced. Nevertheless, the poly-crystals obtained by FeAs self-flux method did not exhibit comparable sample quality as $BaFe_2As_2$ in terms of the small size and low superconducting volume fraction. $CaFeAs_2$ was proposed to be the parent compound and the superconductivity arises from the electron doping of it. However, $CaFeAs_2$ can not be synthesized. It is, first and foremost, important and urgent, to improve the sample quality before we could proceed to understand its superconductivity. Here, a recipe that enables reproducible growth of sizable single crystalline $Ca_{1-x}La_xFeAs_2$(CaLa112) was introduced by CaAs self flux method. Besides, being an exceptional Fe based superconductors (FBS) where the global C_4 rotational symmetry is broken even at room temperature, it is important to extract the similarities and differences between CaLa112 and other FBSs to unravel the nature of its rich emergent orders and interaction in between. Here, I will present a systematic experimental study on this system to understand the competing emergent orders

and discuss the possible insight.

5.2 Experimental results and discussion

5.2.1 Single crystal growth and characterization

On observation of the FeAs growth flux method which would either give tiny poly-crystal[KKO13] or require large amount of starting ingredients[ZZY14, ZXZ15], CaAs self flux method was proposed. The single crystals of $Ca_{0.73}La_{0.27}FeAs_2$ were grown using CaAs self-flux method. The starting ingredients, high purity CaAs, LaAs, FeAs precursors and As powders, were thoroughly grounded and mixed at a ratio of 1.3:0.5:1:0.7 inside glovebox. The mixture was then pressed into a pellet, loaded into an Al crucible, and sealed into a quartz tube under $\frac{1}{3}$ argon atmosphere pressure. The tiny amount of oxidization of precursors or residue of gaseous oxygen sealed inside ampule would deteriorate the sample quality greatly. The ampoule was kept at 1100 °C for 72 h, then was slowly cooled down to 875 °C at a rate of 2 °C/h, followed by water quenching. The partially melted pellet was removed from the crucible at room temperature and rinsed with de-ionized water to get rid of the excess of flux and remaining precursors. A successful synthesis would yield quite an amount of thick silver-shining plate-like single crystals with dimension up to a few millimeter.

The single crystals were characterized by a Panalytical powder X-ray diffractometer at room temperature. The collected data was refined by Fullprof software as illustrated in Fig. 5.1 All the reflections could be well indexed into the $P2_1$ monoclinic structure with lattice parameters a=3.9543(1)$\mathring{A}$, b=3.8866(33)$\mathring{A}$, c=10.3787(1)$\mathring{A}$, α=90.0°, β=91.014(1)° and γ=90.0°. we didn't observe impurity phases. The doping concentration of La was further characterized by WDS on tens of single crystals that having at least one shining surface with uniform thickness. The measurement result indicates the La concentration x is 0.266±0.009. Notably, the concentration within the same pieces were always very close but slight concentration variance exists between different pieces. Within this chapter, the CaLa112 compound grown by this

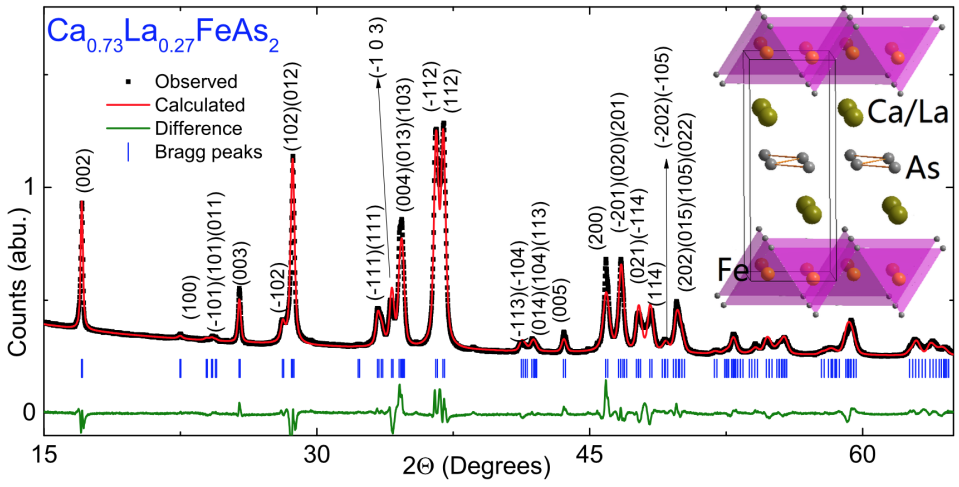

Figure 5.1: The room temperature powder X-ray diffraction and the profile refinement. The blue ticks show the Bragg peak positions. Each peak is indexed to one or several (hkl)s. The inset shows the crystal structure of the CaLa112.

recipe will be labeled as $Ca_{0.73}La_{0.27}FeAs_2$. This recipe results in a rather small sample to sample variance considering that no detectable difference in transition temperature exists.

5.2.2 Evidence of structural and magnetic phase transitions

Based on the sample geometry, the electrical resistivity were measured on *ab* plane (in-plane) and along *c* axis (out of plane), respectively. As seen in Fig. 5.2(a), the in-plane plane resistivity is in the range of 1 mΩ-cm. It decreases with decreasing temperature, reaching an nonzero minimum at the base temperature. This indicates its poor metal nature. The sharp slope change of resistivity around 58 K. The temperature dependent derivative of the in-pane resistivity (Fig. 5.2(d)) shows two kinks. This is reminiscent of the anomaly observed in LaFeAsO and other magnetic FBS [KWH08], which are associated with the structural and magnetic phase transitions[CHL08] there. The resistivity initially increase then decrease along *c* axis upon cooling. This is reminiscent of the one in Ba122 family, which is proposed to be due to the formation of pseudogap[TNT11]. Susceptibility measurement was operated at the condition while field H was perpendicular or parallel to sample *ab*

plane. At both situations, susceptibility shows no Curie-Weiss behavior, suggesting no local moment formation. This also reminisces the other magnetic FBS. Meanwhile, the anomaly in susceptibility also appears around 58 K, confirming the existence of phase transitions. Figure 5.2(d) plots the specific heat data over the derivative of the in-plane resistivity data. The two-kink feature arises at the same temperatures from both measurements. All these measurements suggest that instead of $CaFeAs_2$, $Ca_{0.73}La_{0.27}FeAs_2$ is the "parent" compound of the CaLa112 series since it shows the structural/magnetic instabilities. Assuming a spin gap formation in $Ca_{0.73}La_{0.27}FeAs_2$ like in the other magnetic FBS at low temperatures, the fit of the heat capacity data using $\gamma T+\beta T^3$ leads to γ=12.2 mJ/mol K^2 and Debye temperature θ_D = 346 K. Comparing to $BaFe_2As_2$, the larger value of Debye temperature demonstrates that CaLa112 family has a stiffer lattice.

In order to reveal the nature of those anomalies in Fig. 5.2, elastic neutron scattering data were taken on a $Ca_{0.73}La_{0.27}FeAs_2$ single crystal(namely piece I) at HB1A in Oak Ridge National Lab (ORNL). (0,2,0), chosen as a representative of nuclear Bragg Peaks, and (1/2 1/2 1/2), chosen as a representative of magnetic peaks, were centered and counted while raising the temperature from base. Drawn together in Fig. 5.2(c), the (0 2 0) nuclear peak intensity (black curve) increases below 58 K, which is regarded as a signal of a structural phase transition; the (1/2 1/2 1/2) magnetic peak intensity (red curve) shows a sudden increase below 54 K, indicating a magnetic phase transition. The magnetic peak formation is better seen in Fig. 5.2(g), where (1/2 1/2 1/2) magnetic peak is clearly present at 54 K but absent at 55 K, indicating the onset of a magnetic phase transition at 54 K. These neutron scattering data are consistent with the specific heat capacity and resistivity measurements, clarifying the nature of the two-kink feature in the transport and thermodynamic measurements.

In addition to the neutron scattering measurement, μSR data was used to detect the magnetism inside $Ca_{0.73}La_{0.27}FeAs_2$. Around 100 pieces of $Ca_{0.73}La_{0.27}FeAs_2$ (200 mg) single crystals were wrapped together and measured. Figure 5.2(f) shows the evolution of $Ca_{0.73}La_{0.27}FeAs_2$ magnetic volume fraction and the transverse relaxation rate σ with tem-

perature. Once the temperature falls below 54 K, the magnetic volume fraction builds up to 100% rapidly. A sharp increase in the magnetic volume fraction would suggest the high homogeneity of samples. On the other hand, the transverse relaxation rate, which is proportional to the local magnetic moment, builds up gradually. This implies the magnetic phase transition is of the second-order.

In conclusion, our high quality $Ca_{0.73}La_{0.27}FeAs_2$ single crystals show clearly separated structural and magnetic phase transitions without superconductivity, on the other hand, $Ca_{0.82}La_{0.18}FeAs_2$ exhibits superconductivity with $T_c \approx 42$ K. Therefore, we revealed that $Ca_{0.73}La_{0.27}FeAs_2$ is the "parent" compound of the superconducting CaLa112 family, while the superconducting state of $Ca_{0.82}La_{0.18}FeAs_2$ is induced by hole dopings via substituting La with Ca.

5.2.3 Intrinsically structurally untwined scenario below T_s

Synchrotron single crystal x-ray measurement was performed on $Ca_{0.73}La_{0.27}FeAs_2$ (piece III) at room temperature in Argonne national lab. Figure (5.5) shows the spots at the (0 1 0), (1 0 0) and (1 1 0) position of this single crystal. If there is only one growth domain A, the (0 1 0) reflection is prohibited in this material. Therefore, the spot at (0 1 0) position arises from the (1 0 0) reflection of a second growth domain B whose a axis rotates 90° with respect to the growth domain A. As a result, the (1 1 0) position contains two peaks, one is the (1 1 0) peak from domain A and the other is from the (1 -1 0) peak from domain B. The tiny splitting of these two peaks (Fig.(5.5)) suggests a tiny orientation mismatch between the two growth domains. The intensity of the $(2\ 2\ 0)_A$ and $(2\ -2\ 0)_B$ nuclear peaks are shown in Fig. 5.3, where the superscript A and B denote domain A and domain B, respectively. Neither peak splits below 58 K. This is in sharp contrast with Ba122. The (2 2 0) synchrotron x-ray peak of Ba122 splits into two/four blobs with similar brightness below T_s, which indicates the formation of structural twinning when the symmetry of the crystal structure is lowered below T_s [TKN09]. We double checked the synchrotron x-ray data to make sure no splitting of either peak appears below T_s. Indeed, in the non-reduced data, the $(2\ 2\ 0)_A$ and $(2\ -2\ 0)_B$

are resolved at all temperatures, which unambiguously show that neither peak splits below 58 K. The drastic difference between CaLa112 and Ba122 suggests there is no structural twinning below T_s in $Ca_{0.73}La_{0.27}FeAs_2$. A conservative estimation points to 95% of each growth domain being untwined in this piece. Therefore, the $Ca_{0.73}La_{0.27}FeAs_2$ is intrinsically structurally untwined.

A single crystal of $Ca_{0.73}La_{0.27}FeAs_2$ (piece II) were measured at HB3A in ORNL[CCY11]. At 4.5 K, on observing the peak splitting of (2 -2 0) but with relatively large intensity difference showing in Fig. 5.4, it suggested this piece has merely one major growth domain. What's more, the refinements based on 170 nuclear reflections collected at both 60 K and 4.5 K indicate only one single growth domain exists. A detailed comparison of the peak profile collected at 200 K and 4.5 K for peak (2 0 0) is present in Fig. 5.2(g). Within the measurements' resolution, the low temperature profile almost has the same full width at half maximum (FWHM) as that of the high temperature peak. This observation reminds the same scenario of detwined $BaFe_2As_2$ under 0.7 MPa[DYT12]. Referring to this paper, $BaFe_2As_2$ at ambient pressure would have low temperature (2 0 0) peak with lower peak intensity but broader FWHM due to the formation of twining below T_s. If uniaxial strain is applied and detwined the sample, low temperature (2 0 0) peak would have higher peak intensity but the same FWHM as the high temperature peak profile. This similarity strongly suggests $Ca_{0.73}La_{0.27}FeAs_2$ is either substantially untwined or the twining below T_s is too weak to cause detectable peak broadening.

Further evidence comes from the polarized optical image measurement as shown at Fig. 5.2(h) and (i). At 290 K, as shown on the image, the growth domains are bordered by the bright lines which remain the same to 5 K, the lowest temperature measured. Unlike the extra μm-sized structural domains observed in $BaFe_2As_2$ below T_s[TKN09], none of those extra tiny strips is observed in $Ca_{0.73}La_{0.27}FeAs_2$ at 5 K. It supports that the sample has no detectable twining at this measurement condition.

Though $Ca_{0.73}La_{0.27}FeAs_2$ undergoes structural and magnetic phase transitions, our experimental data strongly suggest that $Ca_{0.73}La_{0.27}FeAs_2$ is substantially structurally untwined below T_s at the experimental resolution. In principle, lowing crystal symmetry would inevitably generates a pair of inequivalent lattice configuration which degenerate in terms of energy. This pair of lattices would form equally in volume below structural phase transition temperature T_s. This is called twinning. In our case, This feature may be related to the As chains in the crystal, which make the T-walls formation energetically unfavorable in $Ca_{0.73}La_{0.27}FeAs_2$, being consistent with the stiffer lattice suggested by the specific heat measurement.

5.2.4 The nature of the magnetic phase transition

We determined the magnetic structure of $Ca_{0.73}La_{0.27}FeAs_2$ based on 13 effective magnetic reflections collected on single crystal piece II(refer to Fig. 5.4). Since synchrotron x-ray diffraction shows that $Ca_{0.73}La_{0.27}FeAs_2$ is substantially untwined, no T walls are considered in the neutron data fitting. We found that a reasonable fit requires two equal volumes with different spin orientations either along a or b axis. The refined magnetic patterns are present in Fig. 5.7. Within one magnetic domain, the spins are aligned head to tail in one direction antiferromagnetically, whereas in the other direction (stripe direction) marked as orange color in Fig. 5.7 are aligned ferromagnetically. Although the detailed magnetic structure of this compound is unique, with the spins being 45° or 135° away from the stripe direction instead of being perpendicular to the stripe direction like in other magnetic FBS, it shows the same AFM stripe pattern with the wave vector k = (1,0) in the 1-Fe cell akin to other FBS, which is consistent with the dynamical mean-field theory(DMFT) calculations from our collaborator. However, the existence of "magnetic domains" with the easy axis 45° or 135° away from the stripe direction suggests the existence of spin-rotation walls (S wall) which separate the regions with the same stripe direction but different spin orientations. The existence of S-walls is consistent with the DMFT calculations which show the magnetic

anisotropy energy of these two spin configurations is so close to each other (0.1 meV/Fe) that they can practically coexist. This is consistent with our DFT calculation collaborator who inferred the anisotropy energy to be ≈0.1 meV/Fe. Finally, the refined data gives moment to be 1.08(3) μ_B/Fe, which agrees well with the theoretical DMFT prediction of 1.0μ_B/Fe.

5.2.5 The nature of the structural phase transition

In all known magnetic FBSs, because of the magnetoelastic coupling, the onset of the (1 0) stripe magnetic order breaks the fourfold rotational symmetry and leads to a tetragonal to orthorhombic phase transition. As a result, the 2-Fe cell enclosed by dashed lines in the lower panel of Fig. 5.7 distorts from an exact square to a rhombus with the short diagonal along the stripe direction[ATB14]. Since the magnetic wave vector of $Ca_{0.73}La_{0.27}FeAs_2$ is the same as those in other magnetic FBS, we expect a similar type of magnetoelastic coupling, which breaks the only symmetry element of $P2_1$ and reduces it to triclinic P1. This leads to $\gamma \neq 90°$. Consequently, the 2-Fe cell distorts from a rectangle into a parallelogram(refer to the upper panel in Fig. 5.7) and (L_1 + L_3) is no longer equal to (L_2 + L_4) below T_s. Figure 5.3(b) shows that upon cooling, the difference in d spacing between these two reflections in Fig. 5.3(a) monotonically increases. A sharp kink at 58 K appears in $d\Delta d/dT$. Assuming $\alpha \approx 90°$, the Δd gives a cell with γ=89.92° and (L_1+L_3)-(L_2+L_4)=0.007(4)$\AA$ at 10 K, suggesting a weak spin-orbit coupling.

5.2.6 The metallic spacer layers

In $Ca_{0.73}La_{0.27}FeAs_2$, the nearest neighbor As to As distance is 2.56(1)$\AA$. It is slightly larger than As-As single bond distance 2.46$\AA$ but much shorter than 3.00$\AA$ where As-As starts to form a bond, suggesting the bond number is slightly less than one. Based on this logic, the $Ca_{0.73}La_{0.27}FeAs_2$ could be model as $Ca^{2+}_{0.73}La^{3+}_{0.27}[FeAs]^{(1.27-\delta)-}As^{(1+\delta)-}$. It indicates that FeAs layer is doped by (0.27-δ) electrons per Fe site.

ARPES measurement and DMFT calculation from our collaborator provide us a quantitative understanding of the electronic structure. The fermiology data from ARPES is summarized in Fig. 5.7(a) and (b). ARPES resolves two hole pockets at the Brillouin zone center Γ and one oval-like electron pocket at the corner M at 67 K akin to the other magnetic FBS using s geometry (electric fields out of the emission plane). Interestingly, an extra electron pocket appears at the Brillouin zone edge (X point), which is qualitatively consistent with the DMFT calculation in Fig. 5.7(c-e). In addition to the two hole pockets (β and γ) at Γ and two similar-sized electron pockets at M with only FeAs layer character, DMFT also reveals one extra electron pocket at X with only an As chain character(in Fig. 5.7(c)). By calculating the volume difference between the Fermi pockets at Γ and M, the DMFT calculation concludes the FeAs layer is doped by 0.17 e/Fe. Since the ARPES k_z dispersion has not been measured, assuming all pockets are 2D-like, a rough estimation of the ARPES Fermi volume suggests a doping level of ∼0.2 e/Fe. Comparing with the prototype electron-doped Ba122[LKF10], this value places $Ca_{0.73}La_{0.27}FeAs_2$ as electron overdoped. A closer look into the Fermi surface (FS) shows that, despite its overdoped nature, a reasonable FS nesting much stronger than the one in electron-overdoped Ba122 survives in this "parent" compound. This highlights the important role of FS nesting in inducing structural and magnetic instabilities.

On the other hand, Figure 5.7(d) shows that the DMFT FS nesting is enhanced upon decreasing x (hole doping). Since experimentally the T_s/T_m are suppressed with decreasing x which can not be simply accounted by the FS nesting picture, it suggests that the super-exchange interaction also plays a role in causing these instabilities. This is one strong piece of evidence of the dual itinerant and localized nature of magnetism in FBS[DHD12]. Both the comparison of the ARPES FS between the "parent" and SC CaLa112 (nominal $x = 0.1$, real $x = 0.18$, $T_c = 42$ K)[ZZY14, LLZ15] and the comparison of the DMFT FS between $x = 0.3$ and $x = 0$ CaLa112 (Fig. 5.7(e)-(f)) reveal the As chains deeply affect the doping mechanism. With Ca doping, part of the holes create an extra 3D hole pocket (α pocket) at

Γ with a mixed Fe and As chain nature[LLZ15], part of them fill the X electron pocket, and part of them distribute to the rest of the pockets.

5.3 Conclusion

Tunable Fe pnictide superconductor(FBS) with metallic layers can shed light on the role of interlayer coupling on the interplay of magnetism and SC in FBSs. Recently, a 10-4-8 FBS family and $Ba_2Ti_2Fe_2As_4O$ have been found to be self-doped with metallic spacer layers[MRR14, SCG13a]. However, there is no good control on the extent of self-doping. Therefore, the CaLa112 system is more promising for the systematic study of the impact of metallic layers in FBSs with a controllable doping level. What is more, since the C4 rotational symmetry is already broken even at room temperature, it raises the question that if electronic nematicity exists in this family. Electronic nematicity lowers the rotational symmetry but keeps the translational symmetry and manifests as the in-plane electronic anisotropy of the 1-Fe cell.[TBK10, INL13, LPZ14, ACM13, YLC11]. It was theoretically proposed that the nematic fluctuation can enhance other types of fluctuations and thus enhance superconductivity. For archetype magnetic FBS, such as Ba122 and FeSe families, suggested by both theory and experiments, the nematic temperature coincides with the T_s. Despite of the absence of C_4 rotational symmetry at room temperature and the subtle distortion in the FeAs layers in $Ca_{0.73}La_{0.27}FeAs_2$, for the first time, our comprehensive experimental study reveals very similar stripe AFM at 54 K and monoclinc to triclinic structural phase transitions at 54 K, akin to the archetype magnetic Ba122. This not only suggests the robust of the FeAs layer in hosting structural/magnetic instabilities and superconductivity, but also allow the possibility of electric nematicity in this CaLa112 family.

In conclusion, $Ca_{0.73}La_{0.27}FeAs_2$ with an overdoped FeAs layer is evidenced to be the "parent" compound of CaLa112 FBS. It is substantially untwined with S walls under ambient pressure below T_s. Furthermore, while the central-hole and corner-electron Fermi pockets

appear with reasonable nesting, both the ARPES and DMFT have unravelled an extra electron pocket at the Brillouin zone edge originating from As chains, establishing the As chains actively participating in the doping mechanism. These characteristics make this material a great platform to study the roles of electronic nematicity and metallic spacer layers in iron based superconductors.

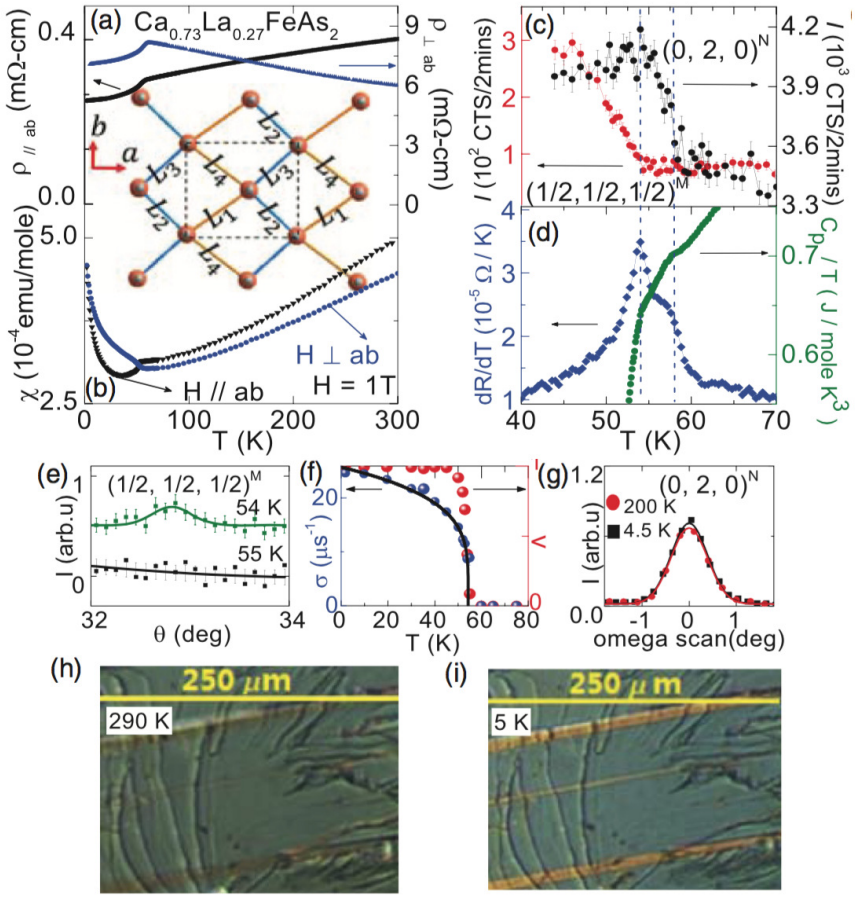

Figure 5.2: (a) Electric resistivity $\rho_{\parallel ab}$ (I $\parallel$ ab) and $\rho_{\perp ab}$ (I $\perp$ ab) vs T. Inset: Top view of the Fe and spacer As sublattices. The structure subtlety is exaggerated. Orange ball: Fe. Gray ball: As in the spacer layers. The orange and blue lines indicate Fe-Fe bonds with bond lengths of L_1, L_2, L_3, and L_4. $L_1 + L_3 = L_2 + L_4$ if $\gamma = 90°$. The dashed lines enclose the unit cell. (b) Susceptibility $\chi_{\parallel ab}$ and $\chi_{\perp ab}$ vs T . (c) The neutron intensity of the nuclear $(0\ 2\ 0)^N$ and the magnetic $(1/2\ 1/2\ 1/2)^M$ peaks vs T . (d) Heat capacity C_p/T and $d\rho_{\parallel ab}/dT$ vs T. (e) The neutron intensity of the $(1/2\ 1/2\ 1/2)^M$ peak at 55 K and 54 K with offset. (f) The magnetically ordered volume fraction V and transverse relaxation rate σ in zero-field muon spin rotation (ZFμSR) asymmetry spectra vs. T. (g) The neutron intensity of the $(0\ 2\ 0)^N$ peak at 200 K and 4.5 K. (h) The polarized optical image at 290 K. (i) The polarized optical image at 5 K.

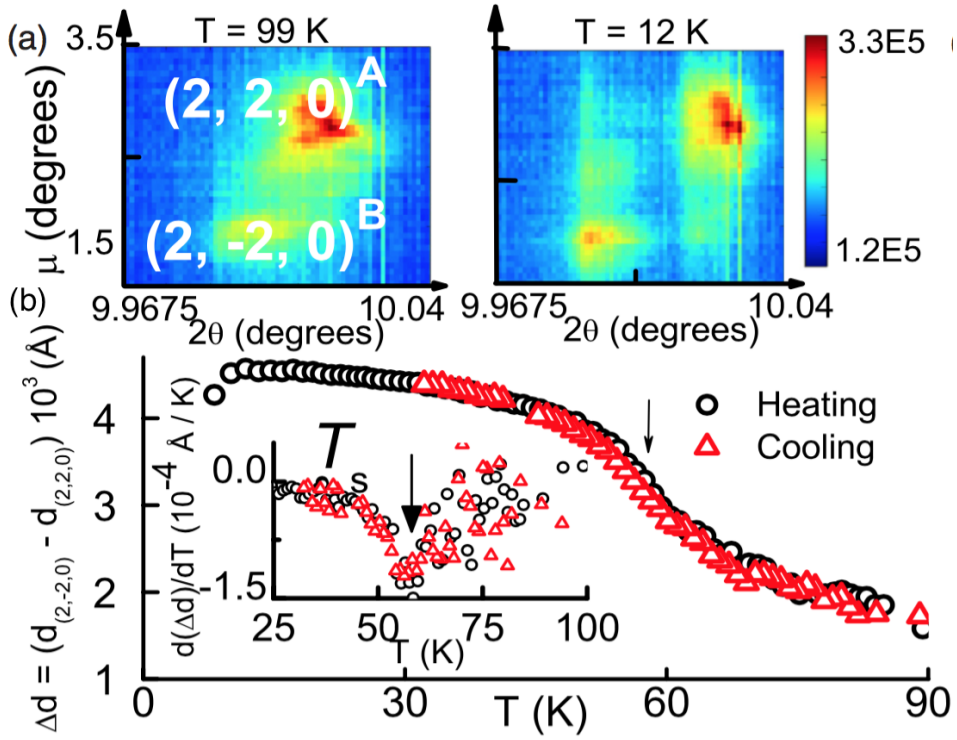

Figure 5.3: (top) The synchrotron x-ray μ vs. 2θ diffractograms of the (2 2 0)^A and (2 -2 0)^B peaks from the growth domains A and B of $Ca_{0.73}La_{0.27}FeAs_2$, respectively. μ is a rotation of the crystal along an axis perpendicular to the x-ray beam. (bottom) Splitting of the two reflections as determined by Gaussian fits. Inset: d(Δd)/dT vs T.

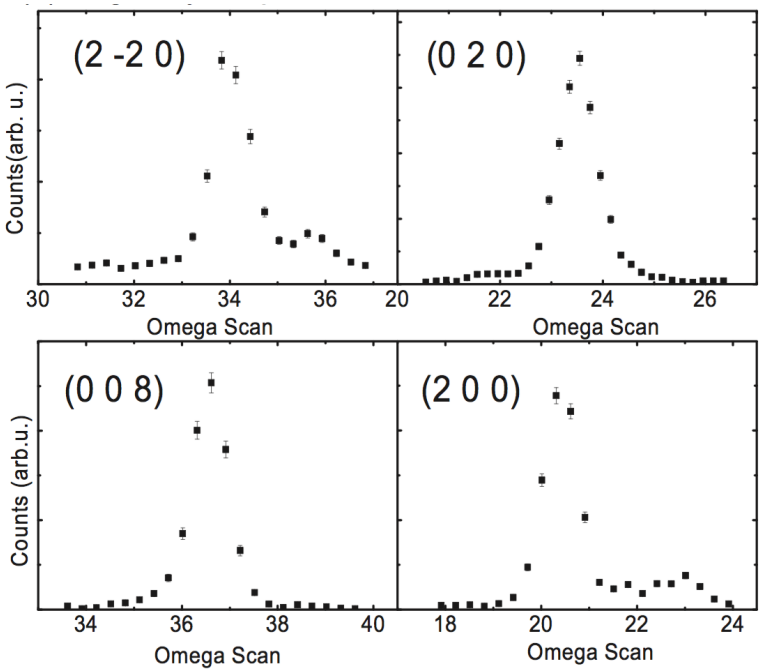

Figure 5.4: Omega scan of the (2 -2 0), (0 2 0), (0 0 8) and (-2 0 0) nuclear Bragg peaks.

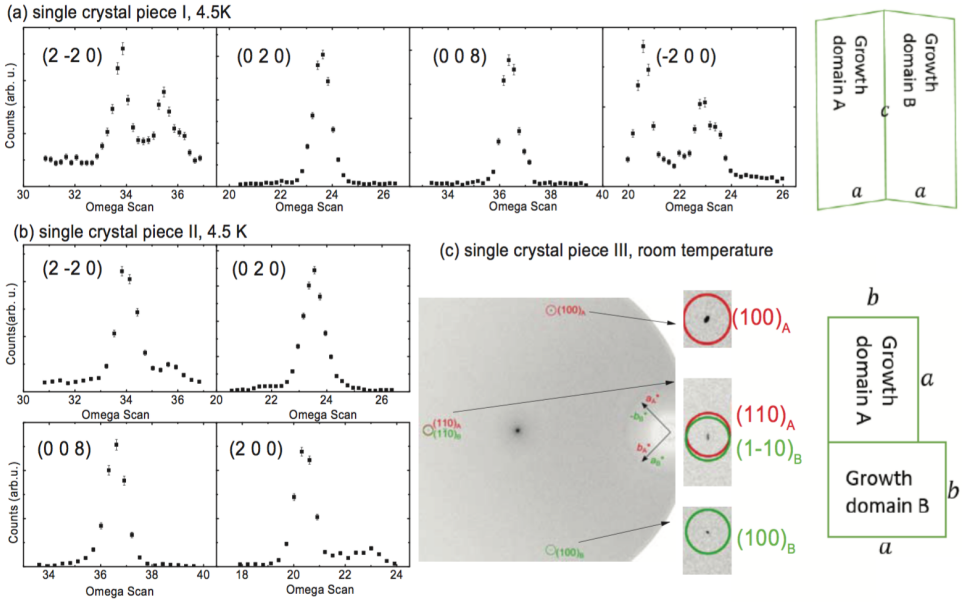

Figure 5.5: (a) Omega scan of the (2 -2 0), (0 2 0), (0 0 8) and (-2 0 0) nuclear Bragg peaks of the single crystal I and the cartoon plot of the domain distribution. (b) Omega scan of the (2 -2 0), (0 2 0), (0 0 8) and (-2 0 0) nuclear Bragg peaks of the single crystal II. (c) The (0 1 0), (1 0 0) and (1 1 0) spots of the single crystal III measured using synchrotron x-ray and the cartoon plot of the domain distribution.

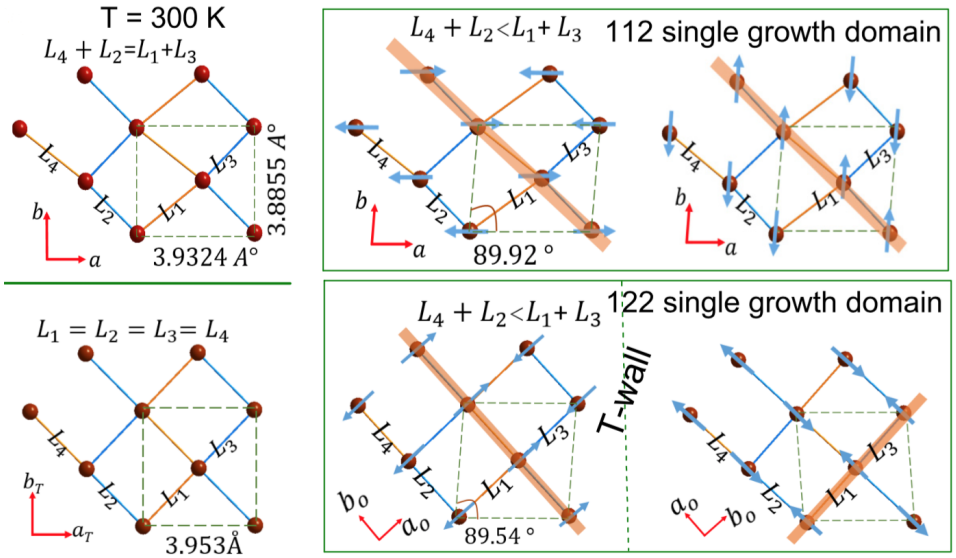

Figure 5.6: The comparison of the magnetic and crystal structures between $Ca_{0.73}La_{0.27}FeAs_2$ and $BaFe_2As_2$ in a single growth domain. Orange ball: Fe. Blue arrow: Spin direction. Orange ribbon: Spin stripe along which the spins order in parallel. The dashed lines enclose the 2-Fe cell.

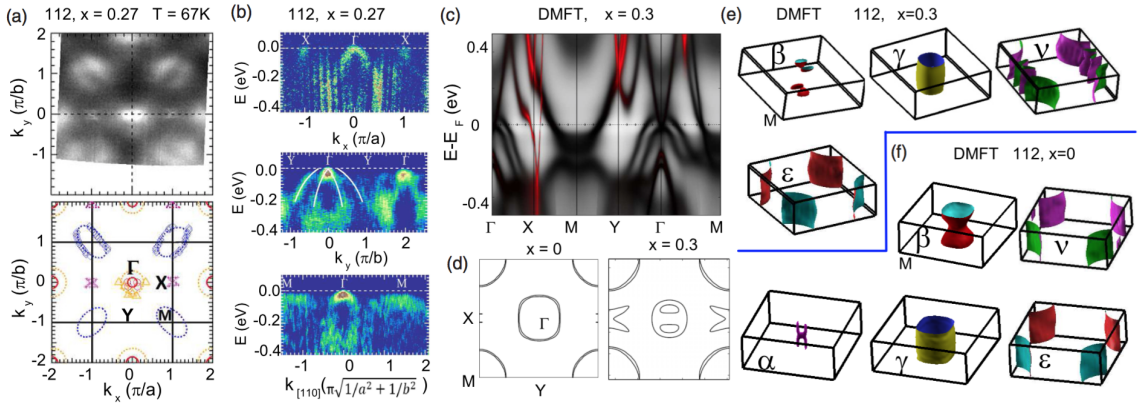

Figure 5.7: (a) The two-dimensional (2D) contour of the angle-resolved photoemission spectroscopy (ARPES) Fermi surface (FS) of $Ca_{0.73}La_{0.27}FeAs_2$ at $K_z \sim \pi/c$ in the 2-Fe/cell representation. Red and orange circles: Two hole pockets at the center Γ point. Blue ovals: Electron pockets at the corner M point. Purple lines: Extra electron pocket arising from the As chains at the X point. (b) The second derivative of ARPES k-E maps. Two hole pockets at Γ points can be clearly identified in the Y-Γ cut. (c) The spectral function A(k,ω) of $Ca_{0.73}La_{0.27}FeAs_2$ from DMFT. The red color represents the projection of the orbital character onto the in-plane p orbitals of the As chain atoms. (d) The 2D contour of the DMFT FS of CaLa112 (x = 0 and 0.3) at $K_z \sim \pi/c$. (e), (f) The 3D DMFT FS of (e) CaLa112 (x = 0.3) and (f) CaLa112 (x = 0.0) in the 2-Fe/cell representation.

CHAPTER 6

Coexistence of superconductivity and antiferromagnetism in $Ca_{0.74(1)}La_{0.26(1)}(Fe_{1-x}Co_x)As_2$ single crystals

6.1 Introduction

In chapter 5, we have shown that we successfully grew, characterized and identified $Ca_{0.73}La_{0.27}FeAs_2$ as the parent compound of the CaLa112 superconducting family, which crystalizes in the FeAs-(Ca/La)-As-(Ca/La)-FeAs-layer stacking with the prototypical FeAs layers and unique zigzag As chains inside. The FeAs layer in $Ca_{0.73}La_{0.27}FeAs_2$ was electron-overdoped by 0.17e/Fe. At this doping level, all other Fe based superconductors (FBS) are neither magnetic nor superconducting. However, we observed a monoclinic-to-triclinic structural phase transition at 58 K, and a paramagnetic to stripe AFM phase transition at 54 K with the easy axis either along a or b axis, which suggest both itinerant and localized nature of the magnetism in FBS. Angle-resolved photoemission (ARPES) measurements revealed two hole pockets at the Brillouin zone center Γ and one oval-like electron pocket at the corner M akin to the other magnetic Fe pnictide superconductors (FBS), with an extra electron pocket of mainly As chain character at the Brillouin zone edge X point. This clearly shows the As-zigzag-chain spacer layers contribute density of states at the Fermi level, indicating the metallic nature of the spacer layers. This observation is also supported by our anisotropic transport measurements and the DMFT calculations.

By substituting La with Ca in the magnetic $Ca_{0.73}La_{0.27}FeAs_2$, the electron over-doped

FeAs layers can be hole doped into superconducting. T_c is reported to be around 40 K [KKO13] in $Ca_{0.82}La_{0.18}FeAs_2$. What is the effect of electron doping in this already electron-overdoped FeAs layer in $Ca_{0.73}La_{0.27}FeAs_2$? Will superconductivity (SC) be realized with electron doping? What is the doping mechanism considering the metallic nature of the spacer layers? To shed lights on the above questions, we decided to dope Co on Fe sites to add extra electrons. While my research was underway, a few groups reported superconductivity in Co doped CaLn112 (Ln = La, Ce, Pr, etc.) polycrystals[YOS15a, XZX15, YOS15b]. However, no systematic research has been performed to understand the doping mechanism and the interplay of AFM, structure and SC in Co doped CaLa112.

In this chapter, a systematic study of Co-doped CaLa112 single crystals will be discussed. We show that upon Co doping, the structure and magnetic phase transitions in $Ca_{0.73}La_{0.27}FeAs_2$ are suppressed, and bulk superconductivity up to 20 K emerges. Using the sample with the WDS Co concentration x of 0.046 as a representative specimen, we report the SC properties of the Co-doped CaLa112 through measurement of Hc_2 and the vortex motion. In particular, the microscopic coexistence of antiferromagnetism and superconductivity in this system is revealed by a combined μSR, susceptibility, and elastic neutron scattering measurements. We contrast this behavior with the related 10-3-8 compound $Ca_{10}(Pt_3As_8)((Fe_{1-x}Co_x)_2As_2)_5$ we discussed in chapter 4, which has similar FeAs interlayer spacing as Co-CaLa112, but displays no AFM-SC coexistence. We interpret this difference in terms of the nature of the spacer layer, which is metallic in the 112 compound but insulating in the 10-3-8 system. Finally, we will discuss the importance of interlayer coupling in affecting the extent of the phase coexistence in FBS within the scope of the mean field theory.

6.2 Experimental results and discussion

6.2.1 Single crystal growth and characterization

Via the recipe similar to that used to make $Ca_{0.73}La_{0.27}FeAs_2$, single crystals of $Ca_{0.74(1)}La_{0.26(1)}(Fe_{1-x}Co_x)As_2$ were grown by CaAs self-flux at a ratio of CaAs : LaAs : FeAs : CoAs : As $= 1.3 : 0.5 : 1 - x_{nominal} : x_{nominal} : 0.7$. The mixture was then pressed into a pellet, loaded into an aluminum crucible, and sealed in a quartz tube under $\frac{1}{3}$ argon atmosphere. The ampoule was kept at 1100 °C for 72 h and then slowly cooled to 875 °C at a rate of 2 °C/h, followed by water quenching. Sizable, thick single crystals were obtained by rinsing off the flux using distilled water. Samples with $x_{nominal} = 7\%$ (which was later determined to have a real concentration x of 0.046) with clean, shiny surfaces were carefully collected for powder XRD measurement, as shown in Figure 6.1. All the peaks can be in-

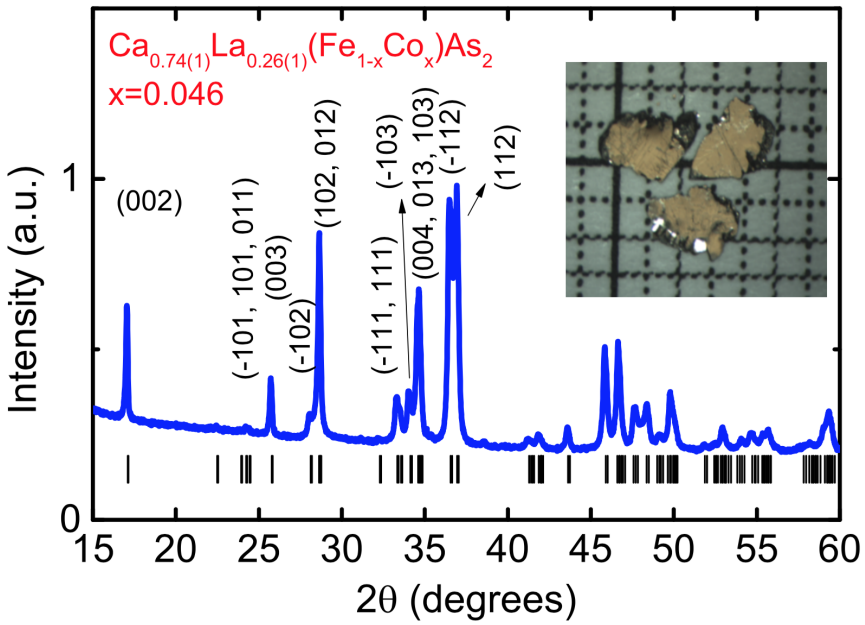

Figure 6.1: The powder x-ray diffraction of $Ca_{0.74(1)}La_{0.26(1)}(Fe_{1-x}Co_x)As_2$ ($x = 0.046$) with (hkl) indexing. Inset: The crystal structure of CaLa112.

dexed in the monoclinic $P2_1$ CaLa112 structure, indicating that the single crystals contain only Co-doped CaLa112. Unlike the case in [XZX15], even in our highest Co doping series,

no $CaFe_2As_2$ peaks are observed.

The complexity of Ca and Co double-doping on $Ca_{0.73}La_{0.27}FeAs_2$ can introduce inhomogeneity in the concentrations. To clarify the effect of Co doping, the variance of the La concentration must be strictly controlled and verified. Thus, WDS measurements were performed on at least five pieces from each batch to determine the concentration and its variance for each nominal concentration. The linear relationship between the nominal concentration $x_{nominal}$ and the real concentration x_{WDS} is summarized in Figure 6.2, which shows that the ratio $x_{WDS}/x_{nominal}$ is ~0.63. The FeAs interlayer distance also demonstrates a linear evolution. Upon Co doping, the interlayer distance shrinks, decreasing by 0.22% at $x = 0.065$. This is comparable to the decrease in the interlayer distance at a similar Co doping level in $BaFe_2As_2$[NTY08]. The small variance of x_{WDS} indicates the homogeneous doping concentration of Co within each batch. The concentrations of La and Co in each batch

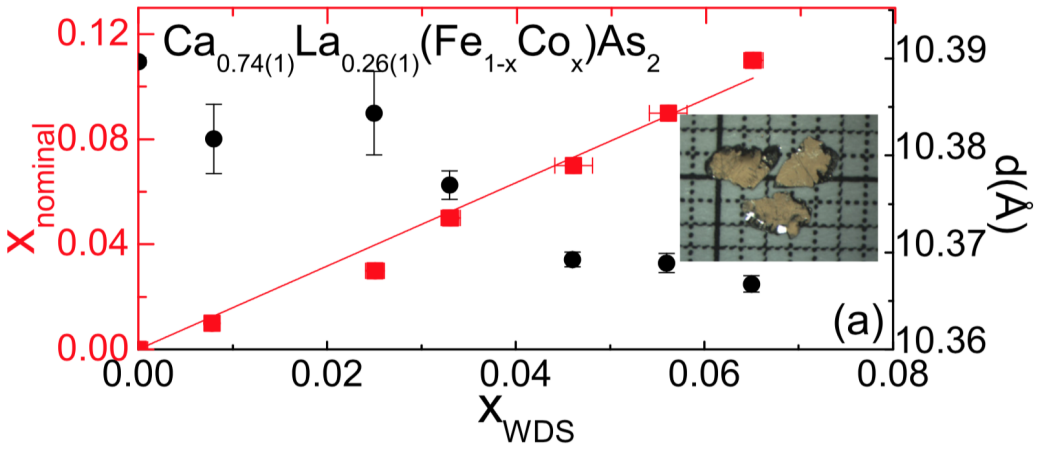

Figure 6.2: The x_{nominal} vs. x_{WDS} and the evolution of the FeAs interlayer distance d with x_{WDS}. Inset: single crystals against the 1 mm scale.

are summarized in Table 6.1. Notably, our WDS data within each piece indicate a very homogeneous concentration, which enables us to perform concentration-based neutron scattering and μSR measurements. On observing the concentration variances of La within each batch, we denote La:x_{WDS} as $La_{0.26(1)}$. Thus, henceforth, the chemical formula for Co-doped

Table 6.1: WDS measurement result for $Ca_{1-x_{WDS}}La_{x_{WDS}}Fe_{1-y_{WDS}}Co_{y_{WDS}}As_2$

Co:$y_{nominal}$	La:x_{WDS}	Co:y_{WDS}
0%	0.270(4)	0
1%	0.250(10)	0.008(1)
3%	0.269(3)	0.025(1)
5%	0.259(5)	0.033(1)
7%	0.249(7)	0.046(4)
9%	0.264(2)	0.056(4)
11%	0.270(6)	0.065(2)

CaLa112 will be denoted as $Ca_{0.74(1)}La_{0.26(1)}(Fe_{1-x}Co_x)As_2$, where x indicates the real Co concentration measured by WDS.

6.2.2 Transport and thermodynamic properties

The resistance of flat, shiny samples with known concentrations was carefully measured. Figure 6.3(a) shows the representative temperature dependence, R/R_{300K} (RRR). Samples with $x = 0$ and $x = 0.008$, which have not yet entered the SC dome, exhibit resistive anomalies around 50 K. The derivative of the RRR for these two samples versus temperature is shown in Fig. 6.3(b). The two-kink feature with the criteria to determine the transition temperatures is shown in d(R/R300 K)/dT. As we discussed in chapter 5, the higher-temperature kink is associated with the monoclinic-to-triclinic structural phase transition, and the lower-temperature kink is related to the paramagnetic-to-AFM magnetic phase transition. The two-kink feature was suppressed to lower temperature with Co doping from $x = 0$ to $x = 0.008$. As shown in Figure 6.3(a), superconductivity emerges when the Co concentration x exceeds 0.008. The critical temperature increases to 10 K in the $x = 0.025$ sample, increases further to 20 K in the $x = 0.046$ sample, and finally drops down to 16 K at $x = 0.065$, forming a dome-like region in the temperature–concentration phase diagram.

The temperature-dependent zero-field-cooled (ZFC) and field-cooled (FC) susceptibility data taken at $H = 5$ Oe and $H \parallel ab$ are shown in Fig. 6.3(c). The small Meissner fraction inferred from the FC data indicates strong flux pinning, which is a common feature in FBS. The ZFC $4\pi\chi$ data for all the concentrations except for $x = 0.025$ show a relatively sharp drop below T_c and saturate at base temperature with a magnitude between ∼110% and ∼120%, which are comparable to those in the prototype Co-doped Ba122 compound[NTY08]. This is in contrast to the much broader transition within Co-doped polycrystalline CaLa112[YOS15a, YOS15b], suggesting the much better homogeneity of our single crystals. Considering the demagnetization effect, the real superconducting volume fraction (SVF) for all samples needs to be corrected. When a thin disk of radius a and thickness $c \ll a$ is placed in a field parallel to the disk plane, its intrinsic susceptibility is given by $\chi_{intrinsic} = \chi_{expt}$ /(1 - 4π Nχ_{expt}), where $N = 0.5\pi c/a$, and χ_{expt} is the experimental value shown in Figure 6.3(c). Given that the average c/a ratio of the four measured pieces is 0.10, the calculation yields an average SC shielding fraction at 2 K to be ∼ 80% for $x = 0.025$ sample without saturation and ∼ 100% for higher concentrations with saturation. The Hall coefficient data for the x = 0 and $x = 0.033$ samples are presented in Fig. 6.3(d). Their negative values indicate that electron carriers dominate the transport properties. The smaller absolute value of the Hall coefficient in the $x = 0.033$ sample confirms that Co doping adds electrons to the system.

As a representative, the superconducting properties of the $x = 0.046$ sample are shown in Fig. 6.4. Figure 6.4(a) presents the upper critical field H_{c2}, which is determined by using the 50% resistivity criterion shown in Figure 6.3(b). The anisotropy parameter of the upper critical field, γ_H, defined as $H_{c2}^{\perp ab}/H_{c2}^{\parallel ab}$, yields a value of approximately 4.7. Because the effective mass anisotropy Γ is related to γ_H by $\Gamma = \gamma_H^2 = m^{*\perp ab}/m^{*\parallel ab}$, the effective mass anisotropy is calculated as approximately 22. Note that $\gamma_H \approx 4.7$ in the 112 compound is smaller than $\gamma_H \approx 8$ in the 10-3-8 compound, which has a similar FeAs interlayer distance but insulating spacer layers. This result suggests stronger FeAs interlayer coupling in the

112 compound, possibly arising from the metallic spacer layers. Figure 6.4(b) shows the temperature-dependent specific heat C_p measurement taken at $H = 0$ T. A bump in C_p associated with the SC phase transition appears, confirming the bulk superconductivity in this sample. By the equal entropy construction shown in Fig. 6.4(b), the heat capacity jump is calibrated as $\Delta C_p/T|_{T_c} \approx 6.7$ mJ/(mole Fe K^2) at $T_c \approx 16$ K. This value follows the Budko–Ni–Canfield (BNC) log–log plot quite well[KFS12], suggesting that $C_p \propto T_c^3$. Because most FBSs that follow BNC scaling[BCB14] show $S^{\pm}$ pairing symmetry, this may suggest an $S^{\pm}$ pairing symmetry in Co-doped CaLa112.

The field-dependent current density J at various temperatures is shown in Fig. 6.4(c). We calculated the critical current density on the basis of the Bean model[BEA64], $J = 20\frac{\Delta M}{\omega(1-\frac{\omega}{3l})}$, where $\Delta M = M_+$-M_-, and $M_+(M_-)$ is the magnetization associated with increasing(decreasing) field; ω and l are the width and length of the sample, respectively. At 2 K, J reaches 2.2×10^5 A/cm^2, which is comparable to those of $FeTe_{0.5}Se_{0.5}$ and LiFeAs but lower than those of $Ba_{0.6}K_{0.4}Fe_2As_2$ and $SmFeAsO_{1-x}$[TTN09]. To understand the mechanism of the vortex motion, the normalized pinning force $f = F_p/F_{p,max}$ as a function of the reduced field ($h = H/H_{irr}$) is plotted in Figure 6.4(d), where $F_p = J \times \mu_0 H$[DD74]. All the curves can be scaled well and are characterized by a maximum near $h = 0.25$. This value is smaller than those of most FBSs but close to the values of $h_{max} = 0.28$ for $FeTe_{0.7}Se_{0.3}$[BGV12], suggesting that both surface pinning and small-scale normal core pinning contribute to the vortex motion.

6.2.3 The temperature-concentration phase diagram

It is critical to understand the interplay between magnetism and superconductivity in FBS since among all the paring mechanisms proposed for the FBS, spin fluctuation mediated SC is the frontrunner[ZHC08b, NKK10, LGZ13]. A theoretical proposal states that $S^{\pm}$ pairing will favor microscopic coexistence of the AFM and SC phases, whereas S^{++} pairing symmetry will result in phase exclusion [FPT10]. Thus, it would be of particular interest if we can

clarify the interplay between AFM and SC phases in Co doped CaLa112.

To get further information on the magnetic phase in the doping series, zero field μSR(ZFμSR) experiments were performed on ∼200 mg of packed randomly oriented single crystals of the $x = 0.025$ and $x = 0.033$ samples, respectively. The ZF asymmetry spectra of the representative $x = 0.033$ sample at selected temperatures are shown in Fig. 6.5(a). Although the resistivity measurements reveal no clear anomaly associated with the structural or magnetic phase transition, an asymmetry loss beginning at 30 K and 10 K appears in the ZFμSR data for $x = 0.025$ and 0.033, respectively. The loss gradually builds during cooling and clearly forms a rapidly relaxing shape at the base temperature, unambiguously demonstrating the existence of magnetic ordering at low temperatures. The ZFμSR data are fitted to a model composed of a fast relaxation term plus a slow relaxation term:

$$A_{ZF}(t) = A[f_T exp(-\frac{1}{2}(\sigma t)^2) + (1 - f_T)exp(-\lambda t)] \tag{6.1}$$

where f_T is the transverse fraction and denotes the rapidly relaxing component originating from the static magnetic order; σ is the fast transverse relaxation rate of muons; and $(1 - f_T)$ is the longitudinal fraction, which represents the fraction of muons trapped in a paramagnetic environment, or muons with spins parallel to the local magnetic field in the region with static magnetic order. The fast relaxation term is formulated in Gaussian relaxation form assuming that muons are affected by the magnetic field produced by randomly oriented magnetic moments. For an ideal isotropic and fully ordered system, f_T is expected to be 0.67, whereas our data show that f_T reaches 0.75, 0.72, and 0.58 in the $x =$ 0, 0.025, and 0.033 samples, respectively. The slightly larger values for the $x = 0$ and 0.025 samples likely arise from the field anisotropy, which results in imperfect randomization of the orientations of the packed plate-like single crystals. Using the scale factor that resets the magnetic volume of the $x = 0$ sample to 100%, we can calculate the magnetic volume fraction, V_{mag}, in the other samples, as shown in Fig. 6.5(b). For the $x = 0.025$ sample, owing to sample inhomogeneity, approximately 6.4% of the sample is already magnetic at 50 K, but for the rest of the sample, antiferromagnetism develops below 31 K, and the V_{mag},

is saturated at $V_{mag} \sim 96\%$ below 20 K. At $x = 0.033$, antiferromagnetism appears below 12 K. V_{mag} increases gradually with cooling and reaches 76% at 2 K without saturation. The fast relaxation rate σ is shown in Fig. 6.5(c). Because σ is proportional to the size of the local magnetic moment, if we assume that the muon sites of the parent and doped samples are similar, we could infer the magnetic moment according to our previous data, which determined that $Ca_{0.73}La_{0.27}FeAs_2$ has a magnetic moment of $1.0\mu_B$/Fe. Thus, a simple calculation yields a magnetic moment of $0.6\mu_B$/Fe for the $x = 0.033$ sample. In addition to the μSR data, which revealed the magnetic phase transition temperature and volume fractions, we also performed elastic neutron scattering measurements on a single pieces of the $x = 0.025$ sample to infer structural/magnetic phase transition temperature, as shown in Fig. 6.5(d). The integrated (0,2,0) nuclear peak intensity increases sharply below 35 K, like that of the parent sample[JLC16], marking the onset of a structural phase transition. The intensity of the (0.5, 0.5, 0.5) magnetic peak increases abruptly below 28 K, indicating the development of long-range magnetic ordering, which is consistent with the μSR data shown in Fig. 6.5(b).

Based on the data discussed above, a temperature–concentration phase diagram is constructed (Fig. 6.6). Upon Co doping, the structural and magnetic phase transitions are suppressed, and superconductivity up to 20 K emerges. In addition, by combining the μSR and ZFC susceptibility data collected at 2 K, it shows that the $x = 0.025$ sample has 96% magnetic volume and approximately 80% superconducting volume; the $x = 0.033$ sample has at least 76% magnetic volume and 100% of superconducting volume, as summarized in Table 6.2. Therefore, superconductivity and antiferromagnetism clearly coexist microscopically in the $x = 0.025$ and 0.033 samples, as in Co-doped Ba122, K-underdoped Ba122, and $Ca_{1-x}La_xFeAs_2$[PTK09, ACG11, JMH09, WLP11, MKD10, MJD12, YZL14, KMM15, JCF08, DJY15]. The coexistence of the AFM and SC phases is consistent with the proposed $s^{\pm}$ order parameter.

It is instructive to compare these results for the 112 $Ca_{1-x}La_xFeAs_2$ compound with those for the 10-3-8 $Ca_{10}(Pt_3As_8)[(Fe_{1-x}Pt_x)_2As_2]_5$ system. Both of them have similar atomic

Table 6.2: SVF and MVF of $x = 0.025$ and $x = 0.033$ samples at 2 K.

x	0.025	0.033
SVF	∼80%	100%
MVF	96%	76%

constituents and very close values for the interlayer FeAs distance. However, in contrast to the 112, where an extended AFM-SC coexistence region emerges, the 10-3-8 shows no coexistence – or at best a very limited region of coexistence [NSW13, CTK12]. One of the most salient differences between these two classes of compounds is the fact that in the 10-3-8, the spacer layer is insulating, whereas in the 112 it is metallic. This difference is manifest, for instance, in the larger H_{c2} anisotropy of the former ($\gamma_H \approx 8$) over the latter ($\gamma_H \approx 4.7$). Presumably, the existence of a metallic spacer layer enhances the FeAs interlayer coupling in the 112, making it more three-dimensional. Although several factors could be at play, it is tempting to attribute the presence of the AFM-SC coexistence region in these systems to the difference in their degree of three-dimensionality promoted by the distinct characters of the spacer layers.

In order to investigate whether the more pronounced k_z band dispersion of the 112 material favors the microscopic coexistence of AFM and SC, we consider a toy two-band model widely employed in the FBS to study the competition of AFM and SC [VVC10, PVC09, FPT10]. This model is characterized by a hole-pocket with dispersion ξ_h at the center of the Brillouin zone and an electron-pocket with dispersion ξ_e at the corner of the Brillouin zone. The fate of the competing AFM-SC phases is determined by a single coefficient g, which depends on the quartic coefficient of the microscopically-derived Ginzburg-Landau expansion [JLS16]: if $g > 0$, the competition between the phase is so strong that there is no coexistence, whereas if $g < 0$, their competition is weak enough to allow them to coexist microscopically. In the hypothetical perfect nesting limit, $\xi_e = -\xi_h$, s^{+-} SC and AFM are at the verge of coexistence or macroscopic phase separation, with $g = 0$. Deviations from perfect nesting then determine whether g becomes positive or negative. Previously, deviations of

perfect nesting arising from the in-plane band dispersions were studied [FPT10, VVC10]. Here, we consider deviations arising from the out-of-plane band dispersion, and write $\xi_e = -\xi_h + \lambda b\,(k_z)$, with the general k_z-dispersion:

$$b\,(k_z) = t_0 + t_1 \cos(p_z) + t_2 \cos(2p_z) \tag{6.2}$$

To ensure that the system is nested at $k_z = 0$, the tight-binding coefficients are constrained to $t_2 = -t_0 - t_1$. In Fig. 6.7[JLS16], we compute the value of g in the (t_0, t_1) parameter space. Clearly, $g < 0$ in a wide region of the parameter space, showing that in general the k_z dispersion can promote microscopic coexistence between SC and AFM. Thus, this simple calculation lends support to the idea that the enhanced interlayer coupling in the 112 promoted by the metallic spacer contributes to the stabilization of a regime of microscopic coexistence between AFM and SC in the phase diagram.

6.3 Conclusion

In summary, we have mapped out the temperature-concentration phase diagram of the $Ca_{0.74(1)}La_{0.26(1)}(Fe_{1-x}Co_x)As_2$ superconductors. Microscopic coexistence between AFM and SC exists in this FBS. The comparison of the temperature-concentration phase diagrams between Co doped CaLa112 and Co-doped 10-3-8 as well as the phenomenological two-band model suggests the dispersion along k_z direction may favor AFM-SC microscopic coexistence over phase separation in FBS.

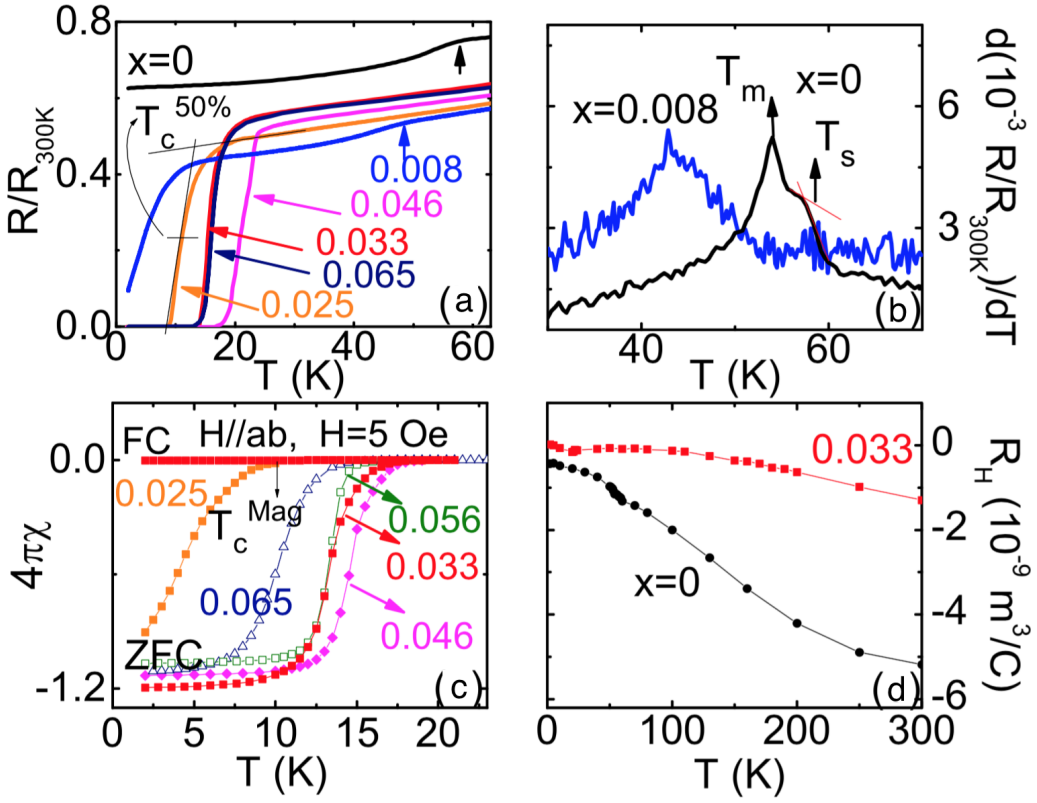

Figure 6.3: (a) Temperature-dependent normalized resistance R/R_{300K} of representative samples. The 50% criterion for inferring T_c from the resistivity is depicted for the $x = 0.025$ sample. (b) Derivative of R/R_{300K} vs. T for the $x = 0$ and $x = 0.008$ samples. The criteria for inferring T_s and T_m are depicted. (c) Temperature-dependent ZFC and FC data with $\mathrm{H}_{\|ab}$. For the $x = 0.025$ sample, the $4\pi\chi$ values of four pieces are averaged. The criterion for inferring T_c from the susceptibility is depicted. (d) Temperature-dependent Hall coefficient for the $x = 0$ and $x = 0.033$ samples.

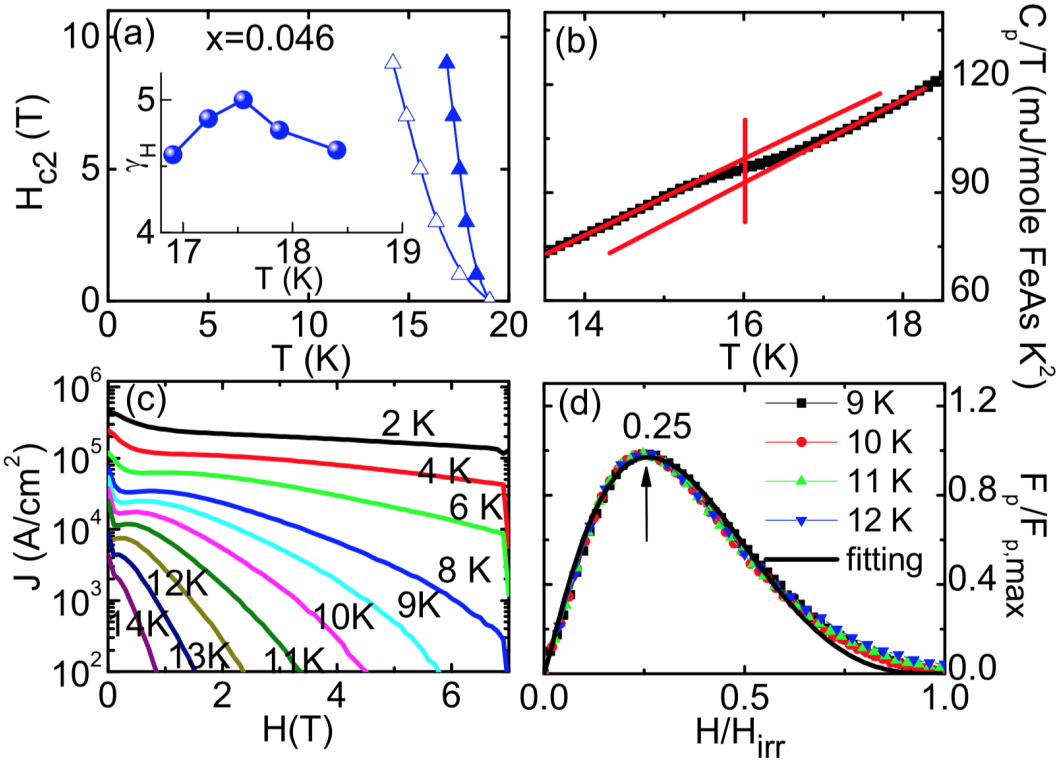

Figure 6.4: $Ca_{0.74(1)}La_{0.26(1)}(Fe_{0.954}Co_{0.046})As_2$: (a) H_{c2} data inferred by applying the 50% criterion [Figure 6.3(b)] to the resistivity data. Inset: the anisotropy parameter of the upper critical field $\gamma_H = H_{c2}^{\perp ab}/H_{c2}^{\parallel ab}$. (b) C/T vs. T. (c) Field-dependent critical current density J at various temperatures with H^{ab}. (d) Normalized pinning force $f = F_p/F_{p,max}$ vs. reduced field $h = H/H_{irr}$ at various temperatures. The data were fitted by $f = Ah^p(1-h)^q$ with the parameters $p = 1.14$ and $q = 3.24$.

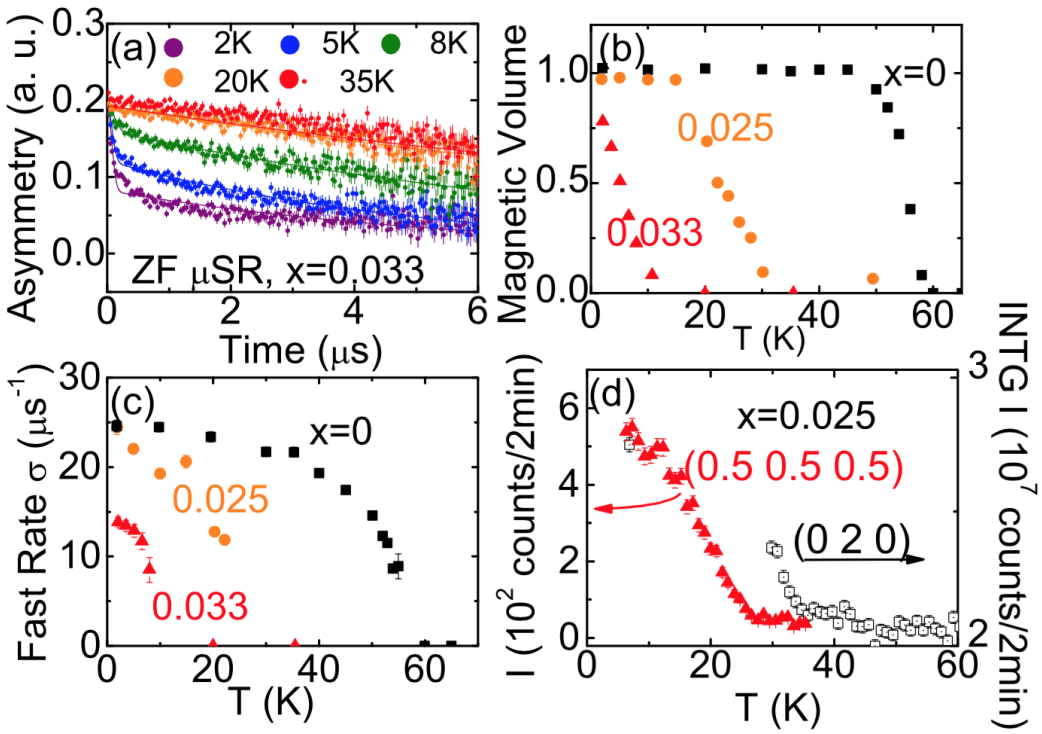

Figure 6.5: $Ca_{0.74(1)}La_{0.26(1)}(Fe_{1-x}Co_x)As_2$: (a) Representative ZF μSR data of the $x = 0.033$ sample. (b) Temperature-dependent ordered MVF V_{mag} determined from the fitting of the ZF μSR asymmetry spectra. (c) Fast transverse relaxation rate σ inferred from the ZFμSR asymmetry spectra. (d) Integrated intensity of the (0,2,0) nuclear neutron peak and intensity of the (0.5,0.5,0.5) magnetic neutron peak.

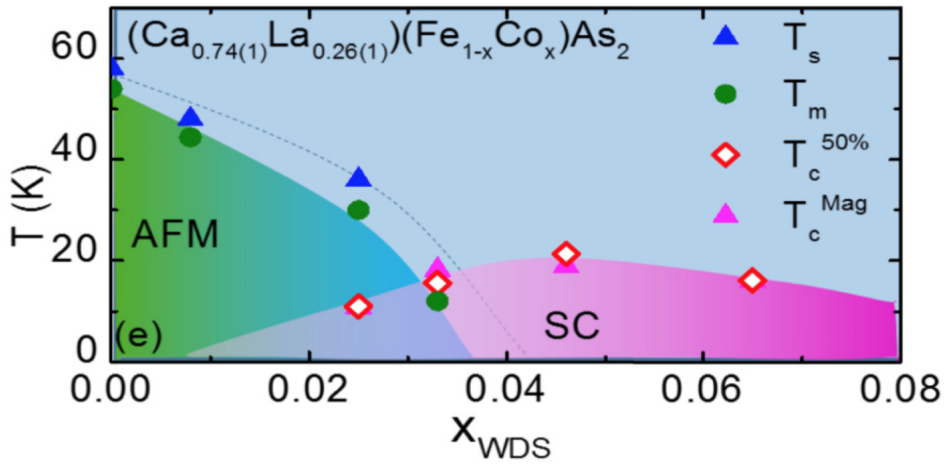

Figure 6.6: Temperature–doping level phase diagram of $Ca_{0.74(1)}La_{0.26(1)}(Fe_{1-x}Co_x)As_2$. For $x = 0$ and 0.008, T_s and T_m are the structural and magnetic phase transitions, respectively, determined from $dR/R_{300K}/dT$, respectively. For the $x = 0.025$ and 0.033 samples, T_m is inferred from the ZF μSR data. T_s for the $x = 0.025$ sample is inferred from elastic neutron scattering data. $T_c^{50\%}$ is the SC transition temperature determined using the 50% criterion shown in Figure 6.3(a). T_c^{Mag} is determined from the susceptibility data using the criterion shown in Figure 6.3(c).

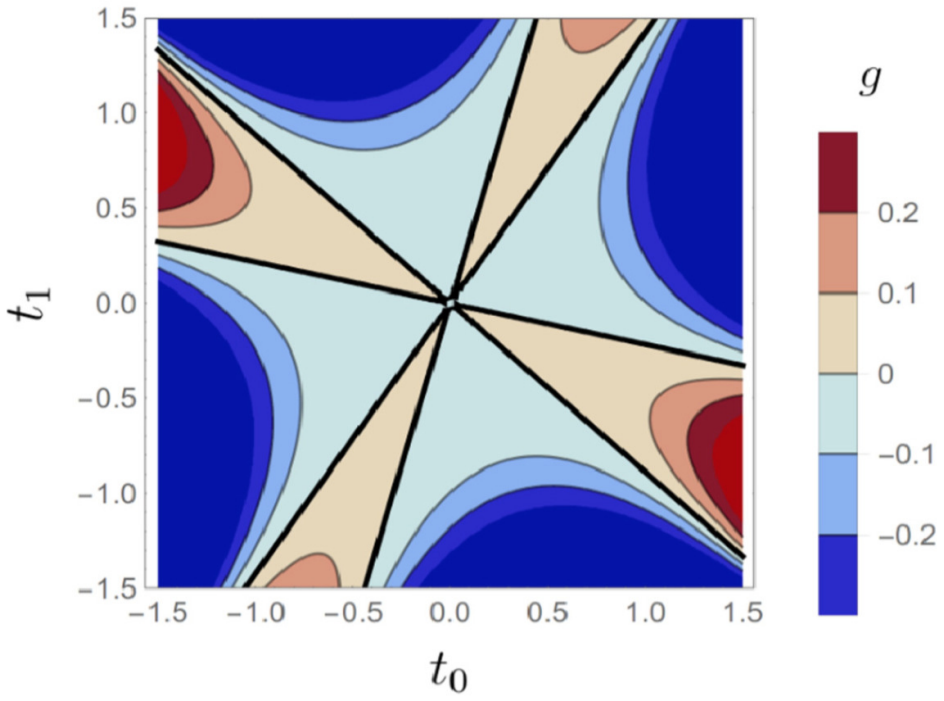

Figure 6.7: Coefficient g as a function of the tight-binding parameters t_0 and t_1 in Eq. 6.2, under the constraint $t_2 = -t_0 - t_1$ to maintain the perfect nesting condition at $k_z = 0$. Note that $g = 0$ at the black lines, whereas $g < 0$ in the blue-shaded region (implying AFM–SC microscopic phase coexistence), and $g > 0$ in the red-shaded region (implying AFM–SC macroscopic phase separation).

CHAPTER 7

Interplay of Fe and rare earth magnetism in CaRE112 single crystals (RE = Ce, Pr, Nd) and the Co doping effect in CaCe112

7.1 Introduction

Since the discovery of superconductivity (SC) in CaLa112[KKO13], the unique quasi-one-dimensional zigzag As chain has enriched the structural complexity within the Fe-based superconductor family. This family holds the record T_c values as high as 47 K[KMK14, KKF14] among oxygen-free Fe pnictides (FPSs). Its parent compound, $Ca_{0.73}La_{0.27}FeAs_2$, which we have extensively discussed in chapter 5, shows a monoclinic to triclinic structural phase transition at 58 K and a paramagnetic (PM) to stripe-like antiferromagnetism (AFM) at 54 K. Electron doping by Co substitution on Fe sites induces SC with a T_c value up to 20 K, which coexists with long range AFM [JLS16] in the underdoped region (chapter 6). By replacing La with other rare earth elements, new series of CaRE112 superconductors were reported in powder form[YOS15a, SYO14].

In sharp contrast to Cuprates, where the inclusion of magnetic rare earth elements suppresses SC, the replacement of La by smaller-sized rare earth elements (Ce-Gd) in Fe pnictides (FPSs) serves as the application of chemical pressure, which can even increase the T_c, despite of the long range magnetic ordering arising from the rare earth sublattice. Beside the effect of the magnetic rare earth elements on SC in FPSs, the interaction between the moments of the Fe sublattice and the rare earth spins have been observed and studied in Eu122

and RE1111 family [ZTL13, SLW12]. Therefore it is interesting to study the effect of magnetic rare earth elements in the CaRE112 family. Previous reports have mainly focused on the polycrystalline samples, which are frequently inhomogeneous and lack of concentration control.

In this chapter, we report the growth of single crystals of the parent CaRE112 (RE = Ce, Pr, Nd) compounds. Transport and magnetic susceptibility data indicate a robust structural and AFM phase transition associated with the FeAs layer. Comparing with the $Ca_{0.73}La_{0.27}FeAs_2$, a new resistive anomaly at low temperature was observed. As a representative, CaCe112 single crystals were examined by elastic neutron scattering and μSR measurements, which reveal the AFM ordering of the Ce sublattice and suggest strong interaction between the Fe and Ce moments even before Ce becomes ordered. Furthermore, a series of Co-doped CaCe112 single crystals were grown. Interestingly, although the structural/magnetic phase transitions are completely suppressed with Co doping, no SC is observed up to the Co doping level of 0.079.

7.2 Experimental results and discussion

7.2.1 Single crystal growth and characterization

High-quality $Ca_{0.71}RE_{0.29}FeAs_2$ (RE = Ce, Pr, Nd) single crystals were grown by the CaAs self-flux method. CaAs powder, FeAs powder, REAs powder, and As powder were thoroughly mixed inside an argon-filled glovebox at a ratio of x:1:0.5:1, where $x = 2.3$ (Ce version) or 1.8 (Pr or Nd version). They were then loaded into an alumina crucible and sealed in a quartz tube under a $\frac{1}{3}$ Ar atmosphere. The ampoule was heated to 1100 °C at 180 °C/h, held for 72 h, and then cooled to 870 °C at 2 °C/h. Water quenching was then applied. The half-melted mixture was rinsed in an ultrasonic water bath, and typical $3 \times 3 \times 0.2$ mm^3 shiny plate-like crystals were obtained, as shown in the inset of Figure 7.1. By substituting the y portion of CoAs in the FeAs layer but maintaining the concentration of the other compounds in the recipe, we grew a Co-doped CaCe112 series with nominal y values ranging from 0 to 0.11.

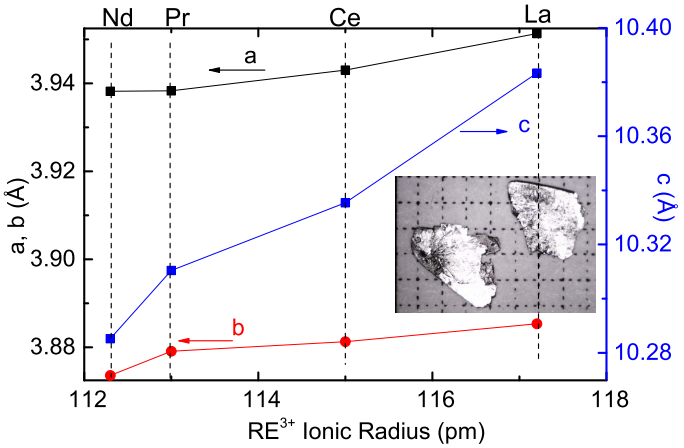

Figure 7.1: Lattice constants a, b, and c vs. ion radii for $Ca_{0.71}RE_{0.29}FeAs_2$ (RE = Ce, Pr, Nd)

The obtained single crystals were characterized by WDS using a JEOL JXA-8200 superprobe combined with a microanalyzer for elemental analysis. For each piece, WDS measurements were performed on multiple locations, and the corresponding concentrations of RE and Co were determined. The FeAs interlayer distances of CaRE112 and Co-doped CaCe112 were determined by scanning the (0 0 l) peak diffraction pattern of pieces with a flat shiny surface using a PANalytical Empyrean diffractometer (Cu Kα radiation) at room temperature. The data were refined using Unit Cell software[HR97]. The in-plane electrical transport data of WDS pieces were collected using a Quantum Design physical property measurement system. The magnetic susceptibility of flat WDS pieces was measured using a Quantum Design magnetic property measurement system with a field of 1 kOe applied parallel to the sample ab plane. Elastic neutron scattering data were collected at HB3A, ORNL.

7.2.2 Physical properties of $Ca_{0.71}RE_{0.29}FeAs_2$ (RE = Ce, Pr, Nd)

The WDS results suggest homogenous single crystals with the chemical formula of $Ca_{0.71}RE_{0.29}FeAs_2$ (RE = Ce, Pr, Nd). Their lattice constants were determined by Rietveld

refinement on respective powder X-ray diffraction patterns. The evolution of the lattice constants versus the rare earth ion size is summarized in Fig. 7.1. As the RE ion changes from La to Ce, Pr, and Nd, the lattice constants decrease monotonically, consistent with the Vegard's law. The largest reduction, approximately 1%, occurs at RE = Nd. This shrinkage caused by substitution on the Ca layer is much more effective than substitution of Co on Fe sites[JLS16], indicating that in addition to the $4f$ electrons, a large chemical pressure is introduced into the system by the rare earth elements.

Table 7.1: Curie–Weiss fitting parameters for $Ca_{0.71}RE_{0.29}FeAs_2$ (RE = Ce, Pr, Nd)

RE ion	χ_0	θ	μ_{eff}	μ_{free}
	10^{-4}emu/mole	K	μ_B/RE	μ_B/RE
Ce	1.4	−63.5	2.47	2.54
Pr	2.6	−24.6	3.57	3.58
Nd	3.1	−16.3	3.31	3.62

The temperature-dependent normalized resistance $R/R_{(300K)}$ of $Ca_{0.71}RE_{0.29}FeAs_2$ (RE = Ce, Pr, Nd) is summarized in Fig. 7.2 (a). No SC states are observed for them. Resistance anomaly akin to the ones in $Ca_{0.73}La_{0.27}FeAs_2$ appear around 60 K, suggesting they are the parent compounds of the CaRE112 superconductors. These features are better seen in the derivative of $R/R_{(300K)}$, as shown in the inset of Fig. 7.2 (a). Similar structural/magentic phase transitions arising from the FeAs sublattice as the ones in $Ca_{0.73}La_{0.27}FeAs_2$ are implied. The inclusion of rare earth elements strongly affect the temperature dependent susceptibility measured with $H \parallel ab$. Unlike the case for $Ca_{0.73}RE_{0.27}FeAs_2$, Curie–Weiss behavior is clearly observed in $Ca_{0.71}RE_{0.29}FeAs_2$ (RE = Ce, Pr, Nd) single crystals, as shown in Fig. 7.2 (b). The unit of the susceptibility is scaled for 1 mole of RE ions. The magnetic contribution from the $4f$ electrons were extracted by subtracting the susceptibility of $Ca_{0.73}RE_{0.27}FeAs_2$ from that of $Ca_{0.71}RE_{0.29}FeAs_2$, as shown in the inset of Fig. 7.2 (b). The subtracted value was then fitted by the Curie–Weiss law according to $\chi_{RE} = \chi_{exp} - \chi_{La} = \chi_0 + \frac{C}{T-\theta}$. The fitting is shown in the inset of Fig. 7.2 (black curves) with the fitted parameters summa-

rized in Table 7.1. The agreement between the fitted effective moment μ_{eff} and free RE^{3+} moment μ_{free} indicates that the rare earth element in CaRE112 behaves as the RE^{3+} ion. The negative Curie temperature θ suggests AFM correlations between these moments.

It is noticeable that although no SC is observed in $Ca_{0.71}RE_{0.29}FeAs_2$ (RE = Ce, Pr, Nd), low temperature anomaly in $R/R_{(300K)}$(T) can be seen below 20 K. Using $Ca_{0.71}Ce_{0.29}FeAs_2$ as the representative, these features can be best seen in Fig. 7.3 (a), which shows $\mathrm{d}(\chi T)/\mathrm{d}T$ and $\mathrm{d}R/R_{(300K)}/\mathrm{d}T$. To elucidate the origin of this observed anomalies, elastic neutron scattering measurement was performed on a sizable $Ca_{0.71}Ce_{0.29}FeAs_2$ single crystal. The red (green) curve in Fig. 7.3 (b) shows the order parameter obtained at the peak center for the magnetic peak (0.5 -0.5 -3.5) peak (nuclear peak (0 2 0)). The (0 2 0) nuclear peak intensity increases drastically below 75 K, suggesting a structural phase transition at 75 K. The slope change in the (0 2 0) nuclear peak intensity and the sharp increase of the (0.5 -0.5 -3.5) magnetic peak intensity below 70 K, indicating the buildup of long range magnetic ordering of the FeAs sublattice below 70 K. These two temperature scales agree well the our transport and thermodynamic data shown in Fig. 7.3 (a), strongly suggesting that the two well-separated structural and magnetic phase transitions in $Ca_{0.71}Ce_{0.29}FeAs_2$. Using the kink-feature in the $\mathrm{d}(R/R_{(300K)})/\mathrm{d}T$ show in the inset of Fig. 7.2 (a), the structural/magnetic phase transition temperatures of $Ca_{0.71}RE_{0.29}FeAs_2$ (RE = Ce, Pr, Nd) are extracted and summarized in Table 7.2. The separation between T_s and T_m is approximately 4–5 K.

Table 7.2: Magnetic and structural phase transition temperatures extracted from transport data for $Ca_{0.71}RE_{0.29}FeAs_2$ (RE = Ce, Pr, Nd)

RE ion	T_s (K)	T_m (K)
La	58	54
Ce	74	69
Pr	69	64
Nd	56	52

In addition to the structural/magnetic phase transitions associated with the FeAs layer,

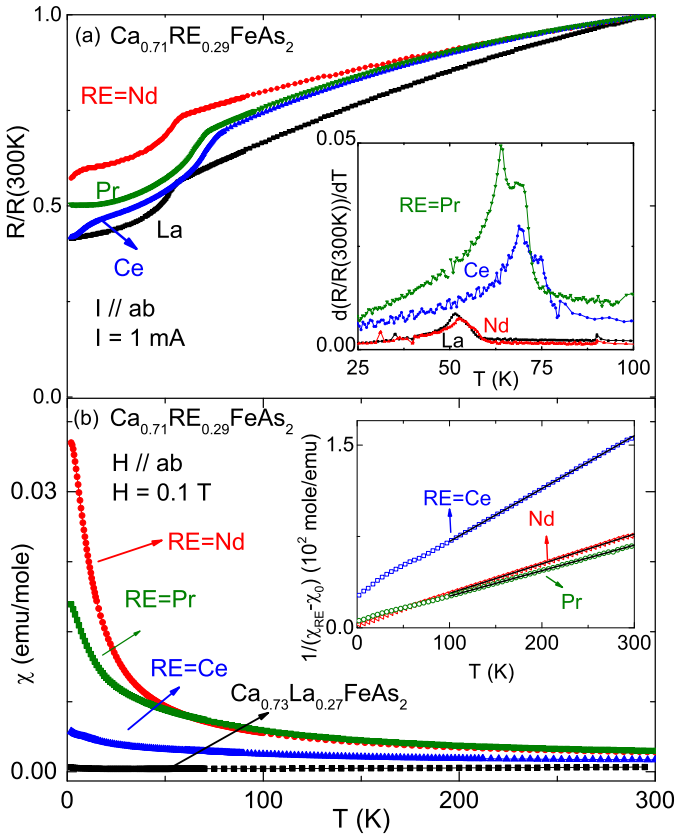

Figure 7.2: (a) Temperature-dependent $R/R(300K)$ of $Ca_{0.71}RE_{0.29}FeAs_2$ (RE = La, Ce, Pr, Nd). Inset: Corresponding derivatives of $R/R(300K)$. Higher and lower-temperature kinks indicate structural and magnetic phase transitions, respectively. (b) Susceptibility of $Ca_{0.71}RE_{0.29}FeAs_2$ (RE = La, Ce, Pr, Nd) under $H = 0.1$ T and $H \parallel ab$. Inset: Curie–Weiss fitting (black curves) compared with the experimental data (open circles).

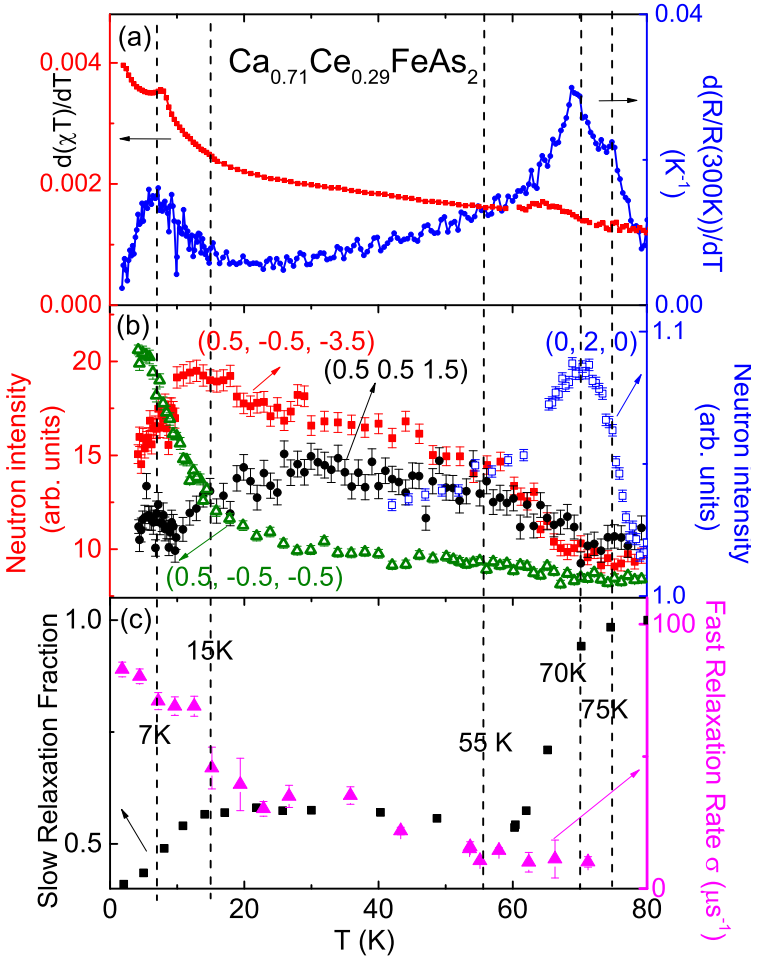

Figure 7.3: (a): d($R/R_{(300K)}$/dT) (blue) and d($\chi\times$ T)/dT (red). (b): Temperature-dependent order parameters at (0 2 0) nuclear peak center and the centers of (0.5 -0.5 -3.5) (red), (0.5 0.5 1.5) (black), and (0.5 -0.5 -0.5) (magenta) magnetic peaks. (c): Slow relaxation fraction and fast relaxation rate obtained from μSR data

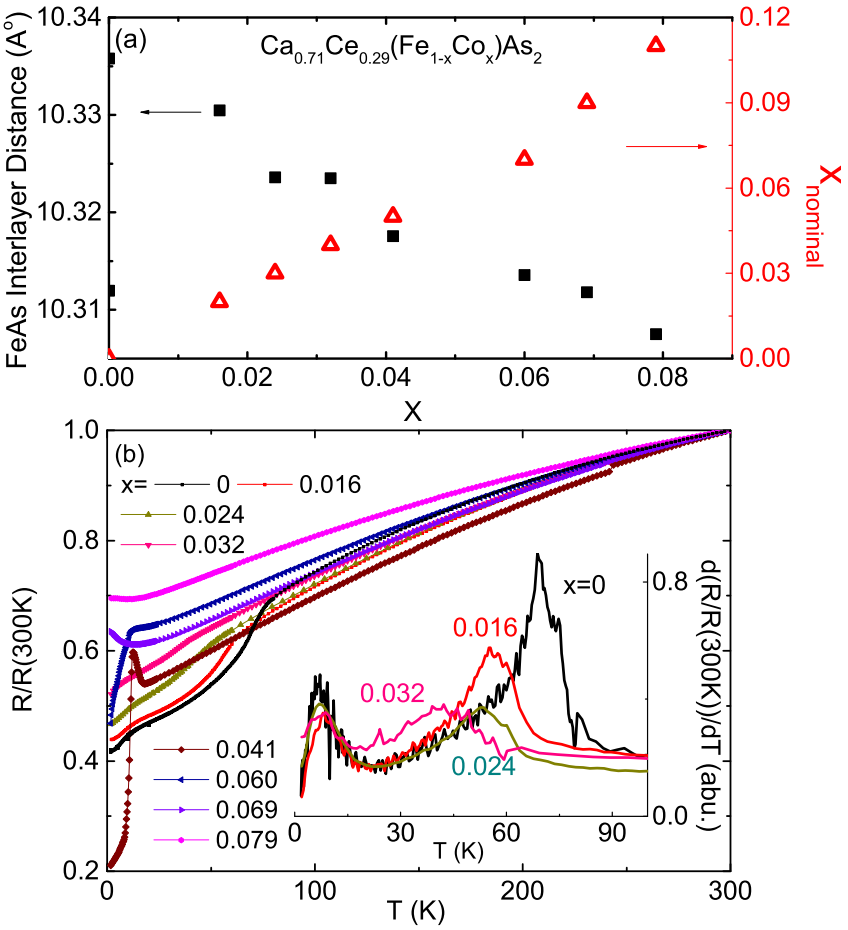

Figure 7.4: (a): $x_{norminal}$ vs. real x in the sample; FeAs interlayer distance vs. real x. Real concentration increases at a slope of ≈0.8 with increasing nominal concentration, whereas the FeAs interlayer distance shrinks monotonically. (b): Temperature-dependent $R/R(300K)$ for $Ca_{0.71}Ce_{0.29}(Fe_{1-x}Co_x)As_2$. Inset: $dR/R(300K)/dT$ vs. T. (x = 0, 0.016, 0.024, and 0.032)

complicated envelope of the order parameters that deviates from the mean field behavior appears in the low-temperature region. Below 15 K, the intensity of the (0.5 -0.5 -3.5) magnetic peak has a clear downward tendency, whereas that of the (0.5 -0.5 -0.5) magnetic peak keeps increasing. Moreover, the (0.5 0.5 1.5) magnetic peak shows a slope change around 7 K. These complex behavior of the order parameters show certain similarities as the ones of CeFeAsO[ZTL13] and PrFeAsO[SLW12], in which the RE ion interacts with the Fe moment even before forming its own order. Our data imply the existence of strong coupling between the Ce ion and Fe magnetic moment in $Ca_{0.71}RE_{0.29}FeAs_2$, like that in Ce1111 and Pr1111.

The ordering of Ce is implied by the μSR data shown in Fig. 7.3 (c), where the fast relaxation rate measures the local moment and the slow relaxation fraction is related to the magnetic volume fraction. The fast relaxation rate, slow relaxation fraction, as well as the (0.5 -0.5 -3.5) magnetic peak intensity all show slope change around 55 K, marking the temperature where the strong interaction between the Ce and Fe moment starts. The sharp increase of the fast relaxation rate below 15 K indicates the existence of a second magnetic phase transition. At approximately 4 K, the fast relaxation rate rises to $85\mu s^{-1}$, which is 3.4 times larger than $25\mu s^{-1}$ in $Ca_{0.73}La_{0.27}FeAs_2$, suggesting the second magnetic ordering arising from the Ce. Two characteristic temperatures related to ordering of Ce can be consistently inferred from the transport, magnetic, neutron and μSR data, as shown in Fig. 7.3 (c). One is at 15 K and the other is at 7 K. The fact that we observed two characteristic temperatures instead of one may suggest more complicated Ce ordering process, such as spin reorientation, etc. It is worth noting that the fitting on μSR data was performed based on the model with only one magnetic sublattice in play, which is not true in our case, therefore, it can be only taken qualitatively, instead of quantitatively. Successful fitting based on the model with two magnetic sublattices requires clear oscillation feature in the μSR asymmetry spectra, which we didn't observe in $Ca_{0.71}Ce_{0.29}FeAs_2$.

7.2.3 The Co doping effect in $Ca_{0.71}Ce_{0.29}(Fe_{1-x}Co_x)As_2$

To study the Co doping effect on $Ca_{0.71}RE_{0.29}FeAs_2$, a series of $Ca_{0.71}Ce_{0.29}(Fe_{1-x}Co_x)As_2$ single crystals were successfully grown. WDS measurements were performed on samples made with higher nominal Co concentration. By assuming a linear relation between the real x and $x_{norminal}$, real x for all series were inferred. Henceforward, x denotes the Co concentration obtain in the way described above, which is summarized in Fig. 7.4 (a). Figure 7.4 (b) shows the FeAs interlayer distance versus x. Increasing the Co dopant does shrink the FeAs interlayer distance, similar to the one in the Co-doped CaLa112 family[JLS16]. The temperature dependent normalized resistance $R/R(300K)$ (T) is shown in 7.4 (b). With Co doping, the resistive anomaly associated with the structural/magentic When x is suppressed to lower temperature. Based on the criteria we have developed to infer these temperatures using the $\mathrm{d}R/R(300K)\mathrm{d}T$ data shown in the inset of Fig. 7.4 (b), we can conclude that the structural/magentic phase transitions are fully suppressed at $x = 0.041$. No bulk SC is observed in all samples we made although a certain amount of resistance drop was observed for the $x = 0.041$ and 0.060 sample. This drop can be suppressed by magnetic field, suggesting trace SC may exist in this region. With even higher doping, resistivity at low temperature stated to slightly increase.

To investigate the evolution of magnetism in $Ca_{0.71}Ce_{0.29}(Fe_{1-x}Co_x)As_2$ with doping, ZFμSR experiments were performed using bags of tiny packed $\sim$200 mg single crystals of $Ca_{0.71}Ce_{0.29}(Fe_{1-x}Co_x)As_2$. Figure 7.5 shows the slow and fast relaxation rates obtained by fitting the μSR data. We want to emphasize that these data, especially the one for the x=0 sample should be taken qualitatively instead of quantitatively since a model with single instead of double magnetic sublattice is used. Nevertheless, it may provide us some hint on the evolution of magnetism. As a reference, the data of $Ca_{0.73}La_{0.27}FeAs_2$ are shown in Fig. 7.5. From the fast relaxation rate shown in Fig. 7.5 (a), firstly, we can see the increase of the rate around 55 K for the $x = 0$ sample, which we argue to mark the onset of the interaction between the Fe and Ce spins. This slope change was suppressed and no longer detectable in the samples with $x = 0.041$, 0.060 and 0.069. Since our transport data reveal that no Fe

ordering in this doping range, it is natural to expect the loss of interaction between Fe and Ce spins for the samples with $x = 0.041$, 0.060 and 0.069. This observation suggests the feasibility of the data analysis even if it is limited. Secondly, the 15 K feature in the $x = 0$ sample is absent for samples with $x = 0.041$, 0.060 and 0.069, implying the suppression of the transition at 15 K. Based on this observation, the 15 K transition of Ce in $Ca_{0.71}Ce_{0.29}FeAs_2$ strongly couples to the Fe spin. Thirdly, the 7 K transition in $Ca_{0.71}Ce_{0.29}FeAs_2$ seems persistent in all doped samples we measured. This is even better seen in the slow relaxation rate shown in Fig. 7.5 (b). Overall, our study of the μSR data suggest a scenario in which sufficient Co doping into $Ca_{0.71}Ce_{0.29}FeAs_2$ suppresses the magnetic ordering of the FeAs layer but has little effect on the ordering of the Ce.

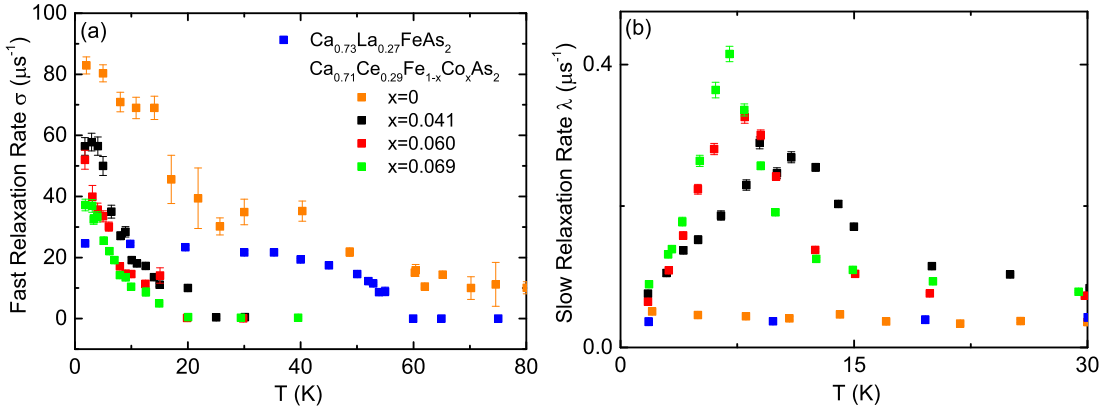

Figure 7.5: Fitted slow relaxation rate (a) and fast relaxation rate (b) from μSR measurement.

Combining our transport and μSR data, we map out the temperature–concentration phase diagram of $Ca_{0.71}Ce_{0.29}(Fe_{1-x}Co_x)As_2$ in Fig. 7.6. Although Co doping has little effect on suppressing the Ce ordering, it suppresses the Fe ordering to lower temperatures without inducing bulk SC state, in contrast to the case in $Ca_{0.74(1)}La_{0.26(1)}(Fe_{1-x}Co_x)As_2$, where SC up to 20 K was observed in an extended doping region. SC is reported to be absent in $Ca_{0.85}Ce_{0.15}FeAs_2$[SYO14] but present in $Ca_{0.9}Ce_{0.1}Fe_{0.97}Co_{0.03}As_2$. It is worth noting that concentrations reported are all nominal concentrations in ref. [SYO14]. But

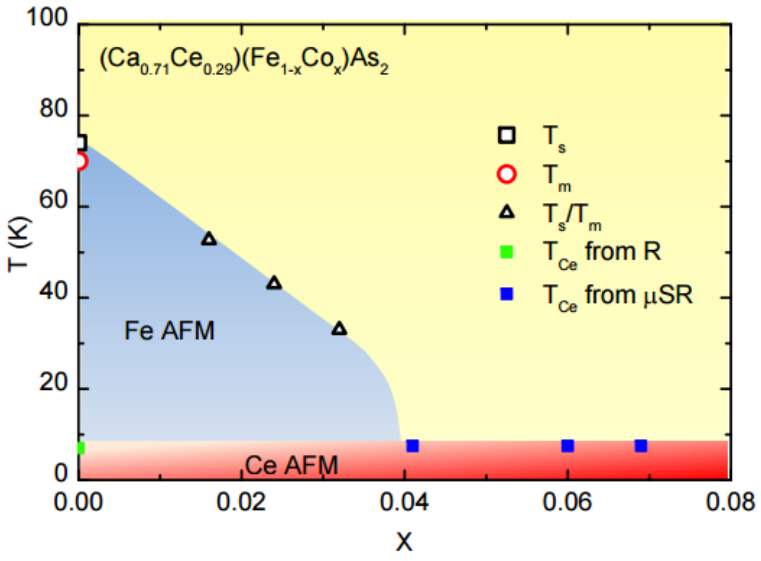

Figure 7.6: The temperature–concentration phase diagram of $Ca_{0.71}Ce_{0.29}(Fe_{1-x}Co_x)As_2$.

this may suggest, to induce bulk SC in CaCe112, less Ce is needed [YOS15a]. Ce plays dual roles in CaCe112. Firstly, it electron-doping the system. Secondly, it brings in large local moment. SC has been observed in RE1111 system, where long range magnetic ordering of RE sublattice coexists with the SC. Therefore, it is unlikely that the Ce local moment will suppress the SC. On the other hand, since our sample has RE concentration as 0.29 which is even higher than the 0.26 in our $Ca_{0.74(1)}La_{0.26(1)}(Fe_{1-x}Co_x)As_2$, the FeAs layer is already electron-overdoped by 0.19/Fe, it is likely further electron doping by Co overshoot the SC window. The other scenario relates the missing of SC to the complicated doping mechanism caused by the Zigzag As chains. Since for CaRE112 systems, during the doping process, both As zigzag chains and the dopant will contribute, it is possible that some subtle difference occurs in $Ca_{0.74(1)}La_{0.26(1)}(Fe_{1-x}Co_x)As_2$ and $Ca_{0.71}Ce_{0.29}(Fe_{1-x}Co_x)As_2$.

7.3 Conclusion

In summary, we systematically studied $Ca_{0.71}RE_{0.29}FeAs_2$ (RE = Ce, Pr, Nd), the parent compound of CaRE112 FPSs. They show robust structural and magnetic phase transitions associated with the FeAs layer around 70 K. Taken $Ca_{0.71}Ce_{0.29}FeAs_2$ as a representative, strong coupling between the Fe and Ce spins is revealed. Two characteristic transition temperatures related to the ordering of the Ce sublattice are observed. With Co doping, the structural/magnetic phase transitions of the FeAs sublattice are suppressed but the ones associated with the Ce sublattice ordering remain with little change. No bulk SC is observed in our doping series $Ca_{0.71}Ce_{0.29}(Fe_{1-x}Co_x)As_2$. This is likely to be the consequence of missing the SC window which only exists if a certain number of electrons are doped into the system.

References

[ACG11] S. Avci, O. Chmaissem, E. A. Goremychkin, S. Rosenkranz, J.-P. Castellan, D. Y. Chung, I. S. Todorov, J. A. Schlueter, H. Claus, M. G. Kanatzidis, A. Daoud-Aladine, D. Khalyavin, and R. Osborn. "Magnetoelastic coupling in the phase diagram of $Ba_{1-x}K_xFe_2As_2$ as seen via neutron diffraction." *Phys. Rev. B*, **83**:172503, May 2011.

[ACM13] M. P. Allan, T-M. Chuang, F. Massee, Yang Xie, Ni Ni, S. L. Bud/'ko, G. S. Boebinger, Q. Wang, D. S. Dessau, P. C. Canfield, M. S. Golden, and J. C. Davis. "Anisotropic impurity states, quasiparticle scattering and nematic transport in underdoped $Ca(Fe_{1-x}Co_x)_2As_2$." *Nat Phys*, **9**(4):220–224, 04 2013.

[10.1038/nphys2544.]

[ATB14] J. M. Allred, K. M. Taddei, D. E. Bugaris, S. Avci, D. Y. Chung, H. Claus, C. dela Cruz, M. G. Kanatzidis, S. Rosenkranz, R. Osborn, and O. Chmaissem. "Coincident structural and magnetic order in $BaFe_2(As_{1-x}P_x)_2$ revealed by high-resolution neutron diffraction." *Phys. Rev. B*, **90**:104513, Sep 2014.

[BCB14] Sergey L. Bud'ko, Duck Young Chung, Daniel Bugaris, Helmut Claus, Mercouri G. Kanatzidis, and Paul C. Canfield. "Heat capacity jump at T_c and pressure derivatives of superconducting transition temperature in the $Ba_{1-x}Na_xFe_2As_2$ ($0.1 \leq x \leq 0.9$) series." *Phys. Rev. B*, **89**:014510, Jan 2014.

[BEA64] CHARLES P. BEAN. "Magnetization of High-Field Superconductors." *Rev. Mod. Phys.*, **36**:31–39, Jan 1964.

[Ber14] Tom Berlijn. "Unfolding the electronic structure of $Ca_{10}(Fe_{1-x}Pt_xAs)_{10}(Pt_nAs_8)$." *Phys. Rev. B*, **89**:104511, Mar 2014.

[BGL92] G. Blatter, V. B. Geshkenbein, and A. I. Larkin. "From isotropic to anisotropic superconductors: A scaling approach." *Phys. Rev. Lett.*, **68**:875–878, Feb 1992.

[BGV12] Marco Bonura, Enrico Giannini, Romain Viennois, and Carmine Senatore. "Temperature and time scaling of the peak-effect vortex configuration in $FeTe_{0.7}Se_{0.3}$." *Phys. Rev. B*, **85**:134532, Apr 2012.

[BM86] J. G. Bednorz and K. A. Müller. "Possible highTc superconductivity in the BaLaCuO system." *Zeitschrift für Physik B Condensed Matter*, **64**(2):189–193, 1986.

[CCG09] C.W. Chu, F. Chen, M. Gooch, A.M. Guloy, B. Lorenz, B. Lv, K. Sasmal, Z.J. Tang, J.H. Tapp, and Y.Y. Xue. "The synthesis and characterization of LiFeAs and NaFeAs." *Physica C: Superconductivity*, **469**(912):326 – 331, 2009. Superconductivity in Iron-Pnictides.

[CCY11] Bryan C. Chakoumakos, Huibo Cao, Feng Ye, Alexandru D. Stoica, Mihai Popovici, Madhan Sundaram, Wenduo Zhou, J. Steve Hicks, Gary W. Lynn, and Richard A. Riedel. "Four-circle single-crystal neutron diffractometer at the High Flux Isotope Reactor." *Journal of Applied Crystallography*, **44**(3):655–658, Jun 2011.

[CF01] Paul C. Canfield and Ian R. Fisher. "High-temperature solution growth of intermetallic single crystals and quasicrystals." *Journal of Crystal Growth*, **225**(24):155 – 161, 2001. Proceedings of the 12th American Conference on Crystal Growth and Epitaxy.

[CHL08] Clarina de la Cruz, Q. Huang, J. W. Lynn, Jiying Li, W. Ratcliff II, J. L. Zarestky, H. A. Mook, G. F. Chen, J. L. Luo, N. L. Wang, and Pengcheng Dai. "Magnetic order close to superconductivity in the iron-based layered $LaO_{1-x}F_xFeAs$ systems." *Nature*, **453**(7197):899–902, 06 2008.

[10.1038/nature07057.]

[CLD08] G. F. Chen, Z. Li, J. Dong, G. Li, W. Z. Hu, X. D. Zhang, X. H. Song, P. Zheng, N. L. Wang, and J. L. Luo. "Transport and anisotropy in single-crystalline $SrFe_2As_2$ and $A_{0.6}K_{0.4}Fe_2As_2$ (A = Sr, Ba) superconductors." *Phys. Rev. B*, **78**:224512, Dec 2008.

[CLW08] G. F. Chen, Z. Li, D. Wu, G. Li, W. Z. Hu, J. Dong, P. Zheng, J. L. Luo, and N. L. Wang. "Superconductivity at 41 K and Its Competition with Spin-Density-Wave Instability in Layered $CeO_{1-x}F_xFeAs$." *Phys. Rev. Lett.*, **100**:247002, Jun 2008.

[CSF16] F. Caglieris, A. Sala, M. Fujioka, F. Hummel, I. Pallecchi, G. Lamura, D. Johrendt, Y. Takano, S. Ishida, A. Iyo, H. Eisaki, H. Ogino, H. Yakita, J. Shimoyama, and M. Putti. "Research Update: Structural and transport properties of (Ca,La)$FeAs_2$ single crystal." *APL Mater.*, **4**(2), 2016.

[CTK12] K. Cho, M. A. Tanatar, H. Kim, W. E. Straszheim, N. Ni, R. J. Cava, and R. Prozorov. "Doping-dependent superconducting gap anisotropy in the two-dimensional pnictide $Ca_{10}(Pt_3As_8)[(Fe_{1-x}Pt_x)_2As_2]_5$." *Phys. Rev. B*, **85**:020504, Jan 2012.

[Dai15] Pengcheng Dai. "Antiferromagnetic order and spin dynamics in iron-based superconductors." *Rev. Mod. Phys.*, **87**:855–896, Aug 2015.

[DD74] D.Dew-Hughes. "Flux pinning mechanisms in type II superconductors." *Philosophical Magazine*, **30**(2):293–305, 1974.

[DFW13] Xiaxin Ding, Delong Fang, Zhenyu Wang, Huan Yang, Jianzhong Liu, Qiang Deng, Guobin Ma, Chong Meng, Yuhui Hu, and Hai-Hu Wen. "Influence of microstructure on superconductivity in $K_xFe_{2-y}Se_2$ and evidence for a new parent phase $K_2Fe_7Se_8$." *Nature Communications*, **4**:1897 EP –, 05 2013.

[DHD12] Pengcheng Dai, Jiangping Hu, and Elbio Dagotto. "Magnetism and its microscopic origin in iron-based high-temperature superconductors." *Nat Phys*, **8**(10):709–718, 10 2012.

[10.1038/nphys2438.]

[DJY15] Xiaoli Dong, Kui Jin, Dongna Yuan, Huaxue Zhou, Jie Yuan, Yulong Huang, Wei Hua, Junliang Sun, Ping Zheng, Wei Hu, Yiyuan Mao, Mingwei Ma, Guangming Zhang, Fang Zhou, and Zhongxian Zhao. "$(Li_{0.84}Fe_{0.16})OHFe_{0.98}Se$ superconductor: Ion-exchange synthesis of large single-crystal and highly two-dimensional electron properties." *Phys. Rev. B*, **92**:064515, Aug 2015.

[DNB09] A. J. Drew, Ch. Niedermayer, P. J. Baker, F. L. Pratt, S. J. Blundell, T. Lancaster, R. H. Liu, G. Wu, X. H. Chen, I. Watanabe, V. K. Malik, A. Dubroka, M. Rossle, K. W. Kim, C. Baines, and C. Bernhard. "Coexistence of static magnetism and superconductivity in $SmFeAsO_{1-x}F_x$ as revealed by muon spin rotation." *Nat Mater*, **8**(4):310–314, 04 2009.

[10.1038/nmat2396.]

[DTS12] Qing-Ping Ding, Yuji Tsuchiya, Yue Sun, Toshihiro Taen, Yasuyuki Nakajima, and Tsuyoshi Tamegai. "Anisotropies and Homogeneities of Superconducting Properties in IronPlatinumArsenide Ca10(Pt3As8)(Fe1.79Pt0.21As2)5." *Journal of the Physical Society of Japan*, **81**(11):114723, 2012.

[DYT12] Chetan Dhital, Z. Yamani, Wei Tian, J. Zeretsky, A. S. Sefat, Ziqiang Wang, R. J. Birgeneau, and Stephen D. Wilson. "Effect of Uniaxial Strain on the Structural and Magnetic Phase Transitions in $BaFe_2As_2$." *Phys. Rev. Lett.*, **108**:087001, Feb 2012.

[DZX08] J. Dong, H. J. Zhang, G. Xu, Z. Li, G. Li, W. Z. Hu, D. Wu, G. F. Chen, X. Dai, J. L. Luo, Z. Fang, and N. L. Wang. "Competing orders and spin-density-wave instability in $La(O_{1-x}F_x)FeAs$." *EPL (Europhysics Letters)*, **83**(2):27006, 2008.

[FDO13] M Fujioka, S J Denholme, T Ozaki, H Okazaki, K Deguchi, S Demura, H Hara, T Watanabe, H Takeya, T Yamaguchi, H Kumakura, and Y Takano. "Phase diagram and superconductivity at 58.1K in α-FeAs-free $SmFeAsO_{1-x}F_x$." *Superconductor Science and Technology*, **26**(8):085023, 2013.

[FKK03] M. Fujita, T. Kubo, S. Kuroshima, T. Uefuji, K. Kawashima, K. Yamada, I. Watanabe, and K. Nagamine. "Magnetic and superconducting phase diagram of electron-doped $Pr_{1-x}LaCe_xCuO_4$." *Phys. Rev. B*, **67**:014514, Jan 2003.

[FPT10] Rafael M. Fernandes, Daniel K. Pratt, Wei Tian, Jerel Zarestky, Andreas Kreyssig, Shibabrata Nandi, Min Gyu Kim, Alex Thaler, Ni Ni, Paul C. Canfield, Robert J. McQueeney, Jörg Schmalian, and Alan I. Goldman. "Unconventional pairing in the iron arsenide superconductors." *Phys. Rev. B*, **81**:140501, Apr 2010.

[Gav73] JR Gavaler. "Superconductivity in Nb-Ge films above 22 K." *Applied Physics Letters*, **23**(8):480–482, 1973.

[GSN14] Peiwen Gao, Liling Sun, Ni Ni, Jing Guo, Qi Wu, Chao Zhang, Dachun Gu, Ke Yang, Aiguo Li, Sheng Jiang, Robert Joseph Cava, and Zhongxian Zhao. "Pressure-Induced Superconductivity and Its Scaling with Doping-Induced Superconductivity in the Iron Pnictide with Skutterudite Intermediary Layers." *Advanced Materials*, **26**(15):2346–2351, 2014.

[HCJ16] J. W. Harter, H. Chu, S. Jiang, N. Ni, and D. Hsieh. "Nonlinear and time-resolved optical study of the 112-type iron-based superconductor parent $Ca_{1-x}La_xFeAs_2$ across its structural phase transition." *Phys. Rev. B*, **93**:104506, Mar 2016.

[HLY08] Fong-Chi Hsu, Jiu-Yong Luo, Kuo-Wei Yeh, Ta-Kun Chen, Tzu-Wen Huang, Phillip M. Wu, Yong-Chi Lee, Yi-Lin Huang, Yan-Yi Chu, Der-Chung Yan, and Maw-Kuen Wu. "Superconductivity in the PbO-type structure α-FeSe." *Proceedings of the National Academy of Sciences*, **105**(38):14262–14264, 2008.

[HMM11] Taku Hanna, Yoshinori Muraba, Satoru Matsuishi, Naoki Igawa, Katsuaki Kodama, Shin-ichi Shamoto, and Hideo Hosono. "Hydrogen in layered iron arsenides: Indirect electron doping to induce superconductivity." *Phys. Rev. B*, **84**:024521, Jul 2011.

[HMS13] Fei Han, Christos D. Malliakas, Constantinos C. Stoumpos, Mihai Sturza, Helmut Claus, Duck Young Chung, and Mercouri G. Kanatzidis. "Superconductivity and strong intrinsic defects in $LaPd_{1-x}Bi_2$." *Phys. Rev. B*, **88**:144511, Oct 2013.

[HR97] T. J. B. Holland and S. A. T. Redfern. "Unit Cell Refinement from Powder Diffraction Data: The Use of Regression Diagnostics." *Mineralogical Magazine*, **61**:65, Feb 1997.

[HUI79] R. S. Hayano, Y. J. Uemura, J. Imazato, N. Nishida, T. Yamazaki, and R. Kubo. "Zero-and low-field spin relaxation studied by positive muons." *Phys. Rev. B*, **20**:850–859, Aug 1979.

[HYL15] Yi-Na Huang, Xiang-Long Yu, Da-Yong Liu, and Liang-Jian Zou. "Magnetism and electronic structures of novel layered $CaFeAs_2$ and $Ca_{0.75}(Pr/La)_{0.25}FeAs_2$." *Journal of Applied Physics*, **117**(17), 2015.

[INL13] S. Ishida, M. Nakajima, T. Liang, K. Kihou, C. H. Lee, A. Iyo, H. Eisaki, T. Kakeshita, Y. Tomioka, T. Ito, and S. Uchida. "Anisotropy of the In-Plane Resistivity of Underdoped $Ba(Fe_{1-x}Co_x)_2As_2$ Superconductors Induced by Impurity Scattering in the Antiferromagnetic Orthorhombic Phase." *Phys. Rev. Lett.*, **110**:207001, May 2013.

[JCF08] Ying Jia, Peng Cheng, Lei Fang, Huiqian Luo, Huan Yang, Cong Ren, Lei Shan, Changzhi Gu, and Hai-Hu Wen. "Critical fields and anisotropy of $NdFeAsO_{0.82}F_{0.18}$ single crystals." *Applied Physics Letters*, **93**(3), 2008.

[JLC16] Shan Jiang, Chang Liu, Huibo Cao, Turan Birol, Jared M. Allred, Wei Tian, Lian Liu, Kyuil Cho, Matthew J. Krogstad, Jie Ma, Keith M. Taddei, Makariy A. Tanatar, Moritz Hoesch, Ruslan Prozorov, Stephan Rosenkranz, Yasutomo J. Uemura, Gabriel Kotliar, and Ni Ni. "Structural and magnetic phase transitions in $Ca_{0.73}La_{0.27}FeAs_2$ with electron-overdoped FeAs layers." *Phys. Rev. B*, **93**:054522, Feb 2016.

[JLS16] Shan Jiang, Lian Liu, Michael Schütt, Alannah M. Hallas, Bing Shen, Wei Tian, Eve Emmanouilidou, Aoshuang Shi, Graeme M. Luke, Yasutomo J. Uemura, Rafael M. Fernandes, and Ni Ni. "Effect of interlayer coupling on the coexistence of antiferromagnetism and superconductivity in Fe pnictide superconductors: A study of $Ca_{0.74(1)}La_{0.26(1)}(Fe_{1-x}Co_x)As_2$ single crystals." *Phys. Rev. B*, **93**:174513, May 2016.

[JMH09] M.-H. Julien, H. Mayaffre, M. Horvati, C. Berthier, X. D. Zhang, W. Wu, G. F. Chen, N. L. Wang, and J. L. Luo. "Homogeneous vs. inhomogeneous coexistence of magnetic order and superconductivity probed by NMR in Co- and K-doped iron pnictides." *EPL (Europhysics Letters)*, **87**(3):37001, 2009.

[KFS12] J. S. Kim, B. D. Faeth, and G. R. Stewart. "Specific-heat discontinuity ΔC vs. T_c in annealed $Ba(Fe_{1-x}Co_x)_2As_2$." *Phys. Rev. B*, **86**:054509, Aug 2012.

[KHY08] Yoichi Kamihara, Masahiro Hirano, Hiroshi Yanagi, Toshio Kamiya, Yuji Saitoh, Eiji Ikenaga, Keisuke Kobayashi, and Hideo Hosono. "Electromagnetic properties and electronic structure of the iron-based layered superconductor LaFePO." *Phys. Rev. B*, **77**:214515, Jun 2008.

[KKF14] Kazutaka Kudo, Yutaka Kitahama, Kazunori Fujimura, Tasuku Mizukami, Hiromi Ota, and Minoru Nohara. "Superconducting Transition Temperatures of up to 47 K from Simultaneous Rare-Earth Element and Antimony Doping of 112-Type $CaFeAs_2$." *Journal of the Physical Society of Japan*, **83**(9):093705, 2014.

[KKN11] Satomi Kakiya, Kazutaka Kudo, Yoshihiro Nishikubo, Kenta Oku, Eiji Nishibori, Hiroshi Sawa, Takahisa Yamamoto, Toshio Nozaka, and Minoru Nohara. "Superconductivity at 38 K in Iron-Based Compound with Platinum-Arsenide Layers $Ca_{10}(Pt_4As_8)(Fe_{2-x}Pt_xAs_2)_5$." *Journal of the Physical Society of Japan*, **80**(9):093704, 2011.

[KKO13] Naoyuki Katayama, Kazutaka Kudo, Seiichiro Onari, Tasuku Mizukami, Kento Sugawara, Yuki Sugiyama, Yutaka Kitahama, Keita Iba, Kazunori Fujimura, Naoki Nishimoto, Minoru Nohara, and Hiroshi Sawa. "Superconductivity in $Ca_{1-x}La_xFeAs_2$: A Novel 112-Type Iron Pnictide with Arsenic Zigzag Bonds." *Journal of the Physical Society of Japan*, **82**(12):123702, 2013.

[KMK14] Kazutaka Kudo, Tasuku Mizukami, Yutaka Kitahama, Daisuke Mitsuoka, Keita Iba, Kazunori Fujimura, Naoki Nishimoto, Yuji Hiraoka, and Minoru Nohara.

"Enhanced Superconductivity up to 43 K by P/Sb Doping of $Ca_{1-x}La_xFeAs_2$." *Journal of the Physical Society of Japan*, **83**(2):025001, 2014.

[KMM15] Shinji Kawasaki, Tomosuke Mabuchi, Satoki Maeda, Tomoki Adachi, Tasuku Mizukami, Kazutaka Kudo, Minoru Nohara, and Guo-qing Zheng. "Doping-enhanced antiferromagnetism in $Ca_{1-x}La_xFeAs_2$." *Phys. Rev. B*, **92**:180508, Nov 2015.

[KSJ13] J S Kim, T Strzer, D Johrendt, and G R Stewart. "The specific heat of the electron-doped La-1038 compound $(Ca_{0.85}La_{0.15})_{10}(FeAs)_{10}(Pt_3As_8)$." *Journal of Physics: Condensed Matter*, **25**(13):135701, 2013.

[KSS14] Naoyuki Katayama, Kento Sugawara, Yuki Sugiyama, Takafumi Higuchi, Kazutaka Kudo, Daisuke Mitsuoka, Takashi Mizokawa, Minoru Nohara, and Hiroshi Sawa. "Synchrotron X-ray Diffraction Study of Structural Phase Transition in $Ca_{10}(Ir_4As_8)(Fe_{2-x}Ir_xAs_2)_5$." *Journal of the Physical Society of Japan*, **83**(11):113707, 2014.

[KWH08] Yoichi Kamihara, Takumi Watanabe, Masahiro Hirano, and Hideo Hosono. "Iron-Based Layered Superconductor $La[O_{1-x}F_x]FeAs$ (x = 0.05-0.12) with Tc = 26 K." *Journal of the American Chemical Society*, **130**(11):3296–3297, 2008. PMID: 18293989.

[KWI11] K. Kodama, S. Wakimoto, N. Igawa, S. Shamoto, H. Mizoguchi, and H. Hosono. "Crystal and magnetic structures of the superconductor $CeNi_{0.8}Bi_2$." *Phys. Rev. B*, **83**:214512, Jun 2011.

[KZK09] J. Karpinski, N.D. Zhigadlo, S. Katrych, Z. Bukowski, P. Moll, S. Weyeneth, H. Keller, R. Puzniak, M. Tortello, D. Daghero, R. Gonnelli, I. Maggio-Aprile, Y. Fasano, . Fischer, K. Rogacki, and B. Batlogg. "Single crystals of $LnFeAsO_{1-x}F_x$ (Ln = La, Pr, Nd, Sm, Gd) and $Ba_{1-x}Rb_xFe_2As_2$: Growth, structure and superconducting properties." *Physica C: Superconductivity*, **469**(912):370 – 380, 2009. Superconductivity in Iron-Pnictides.

[LCH09] Shiliang Li, Clarina de la Cruz, Q. Huang, Y. Chen, J. W. Lynn, Jiangping Hu, Yi-Lin Huang, Fong-Chi Hsu, Kuo-Wei Yeh, Maw-Kuen Wu, and Pengcheng Dai. "First-order magnetic and structural phase transitions in $Fe_{1+y}Se_xTe_{1-x}$." *Phys. Rev. B*, **79**:054503, Feb 2009.

[LGZ13] Xingye Lu, H. Gretarsson, Rui Zhang, Xuerong Liu, Huiqian Luo, Wei Tian, Mark Laver, Z. Yamani, Young-June Kim, A. H. Nevidomskyy, Qimiao Si, and Pengcheng Dai. "Avoided Quantum Criticality and Magnetoelastic Coupling in $BaFe_{2-x}Ni_xAs_2$." *Phys. Rev. Lett.*, **110**:257001, Jun 2013.

[LIE08] Chul-Ho Lee, Akira Iyo, Hiroshi Eisaki, Hijiri Kito, Maria Teresa Fernandez-Diaz, Toshimitsu Ito, Kunihiro Kihou, Hirofumi Matsuhata, Markus Braden, and Kazuyoshi Yamada. "Effect of Structural Parameters on Superconductivity in

Fluorine-Free $LnFeAsO_{1-y}$ (Ln = La, Nd)." *Journal of the Physical Society of Japan*, **77**(8):083704, 2008.

[LKF10] Chang Liu, Takeshi Kondo, Rafael M. Fernandes, Ari D. Palczewski, Eun Deok Mun, Ni Ni, Alexander N. Thaler, Aaron Bostwick, Eli Rotenberg, Jorg Schmalian, Sergey L. Bud/'ko, Paul C. Canfield, and Adam Kaminski. "Evidence for a Lifshitz transition in electron-doped iron arsenic superconductors at the onset of superconductivity." *Nat Phys*, **6**(6):419–423, 06 2010.

[10.1038/nphys1656.]

[LKK09] H. Luetkens, H. H. Klauss, M. Kraken, F. J. Litterst, T. Dellmann, R. Klingeler, C. Hess, R. Khasanov, A. Amato, C. Baines, M. Kosmala, O. J. Schumann, M. Braden, J. Hamann-Borrero, N. Leps, A. Kondrat, G. Behr, J. Werner, and B. Buchner. "The electronic phase diagram of the $LaO_{1-x}F_xFeAs$ superconductor." *Nat Mater*, **8**(4):305–309, 04 2009.

[10.1038/nmat2397.]

[LLW09] L J Li, Y K Luo, Q B Wang, H Chen, Z Ren, Q Tao, Y K Li, X Lin, M He, Z W Zhu, G H Cao, and Z A Xu. "Superconductivity induced by Ni doping in $BaFe_2As_2$ single crystals." *New Journal of Physics*, **11**(2):025008, 2009.

[LLZ15] M. Y. Li, Z. T. Liu, W. Zhou, H. F. Yang, D. W. Shen, W. Li, J. Jiang, X. H. Niu, B. P. Xie, Y. Sun, C. C. Fan, Q. Yao, J. S. Liu, Z. X. Shi, and X. M. Xie. "Significant contribution of As $4p$ orbitals to the low-lying electronic structure of the 112-type iron-based superconductor $Ca_{0.9}La_{0.1}FeAs_2$." *Phys. Rev. B*, **91**:045112, Jan 2015.

[LPZ14] Xingye Lu, J. T. Park, Rui Zhang, Huiqian Luo, Andriy H. Nevidomskyy, Qimiao Si, and Pengcheng Dai. "Nematic spin correlations in the tetragonal state of uniaxial-strained $BaFe_{2-x}Ni_xAs_2$." *Science*, **345**(6197):657–660, 2014.

[LST11] Catrin Lhnert, Tobias Strzer, Marcus Tegel, Rainer Frankovsky, Gina Friederichs, and Dirk Johrendt. "Superconductivity up to 35K in the Iron Platinum Arsenides $(CaFe_{1-x}Pt_xAs)10Pt_{4-y}As_8$ with Layered Structures." *Angewandte Chemie International Edition*, **50**(39):9195–9199, 2011.

[MJD12] Long Ma, G. F. Ji, Jia Dai, X. R. Lu, M. J. Eom, J. S. Kim, B. Normand, and Weiqiang Yu. "Microscopic Coexistence of Superconductivity and Antiferromagnetism in Underdoped $Ba(Fe_{1-x}Ru_x)_2As_2$." *Phys. Rev. Lett.*, **109**:197002, Nov 2012.

[MKD10] P. Marsik, K. W. Kim, A. Dubroka, M. Rössle, V. K. Malik, L. Schulz, C. N. Wang, Ch. Niedermayer, A. J. Drew, M. Willis, T. Wolf, and C. Bernhard. "Coexistence and Competition of Magnetism and Superconductivity on the Nanometer Scale in Underdoped $BaFe_{1.89}Co_{0.11}As_2$." *Phys. Rev. Lett.*, **105**:057001, Jul 2010.

[MLT03] T Masui, S Lee, and S Tajima. "Origin of superconductivity transition broadening in MgB_2." *Physica C: Superconductivity*, **383**(4):299 – 305, 2003.

[MRR14] J.-Z. Ma, A. van Roekeghem, P. Richard, Z.-H. Liu, H. Miao, L.-K. Zeng, N. Xu, M. Shi, C. Cao, J.-B. He, G.-F. Chen, Y.-L. Sun, G.-H. Cao, S.-C. Wang, S. Biermann, T. Qian, and H. Ding. "Correlation-Induced Self-Doping in the Iron-Pnictide Superconductor $Ba_2Ti_2Fe_2As_4O$." *Phys. Rev. Lett.*, **113**:266407, Dec 2014.

[MTM08] Serena Margadonna, Yasuhiro Takabayashi, Martin T. McDonald, Karolina Kasperkiewicz, Yoshikazu Mizuguchi, Yoshihiko Takano, Andrew N. Fitch, Emmanuelle Suard, and Kosmas Prassides. "Crystal structure of the new $FeSe_{1-x}$ superconductor." *Chem. Commun.*, pp. 5607–5609, 2008.

[NAC11] Ni Ni, Jared M. Allred, Benny C. Chan, and Robert Joseph Cava. "High Tc electron doped $Ca_{10}(Pt_3As_8)(Fe_2As_2)_5$ and $Ca_{10}(Pt_4As_8)(Fe_2As_2)_5$ superconductors with skutterudite intermediary layers." *Proceedings of the National Academy of Sciences*, **108**(45):E1019–E1026, 2011.

[NKK10] S. Nandi, M. G. Kim, A. Kreyssig, R. M. Fernandes, D. K. Pratt, A. Thaler, N. Ni, S. L. Bud'ko, P. C. Canfield, J. Schmalian, R. J. McQueeney, and A. I. Goldman. "Anomalous Suppression of the Orthorhombic Lattice Distortion in Superconducting $Ba(Fe_{1-x}Co_x)_2As_2$ Single Crystals." *Phys. Rev. Lett.*, **104**:057006, Feb 2010.

[NLX12] Madhab Neupane, Chang Liu, Su-Yang Xu, Yung-Jui Wang, Ni Ni, J. M. Allred, L. A. Wray, N. Alidoust, Hsin Lin, R. S. Markiewicz, A. Bansil, R. J. Cava, and M. Z. Hasan. "Fermi-surface topology and low-lying electronic structure of the iron-based superconductor $Ca_{10}(Pt_3As_8)(Fe_2As_2)_5$." *Phys. Rev. B*, **85**:094510, Mar 2012.

[NNM15] Yuki Nagai, Hiroki Nakamura, Masahiko Machida, and Kazuhiko Kuroki. "First-Principles Study of Antimony Doping Effects on the Iron-Based Superconductor $CaFe(Sb_xAs_{1-x})_2$." *Journal of the Physical Society of Japan*, **84**(9):093702, 2015.

[NSW13] N. Ni, W. E. Straszheim, D. J. Williams, M. A. Tanatar, R. Prozorov, E. D. Bauer, F. Ronning, J. D. Thompson, and R. J. Cava. "Transport and thermodynamic properties of $(Ca_{1-x}La_x)_{10}(Pt_3As_8)(Fe_2As_2)_5$ superconductors." *Phys. Rev. B*, **87**:060507, Feb 2013.

[NTY08] N. Ni, M. E. Tillman, J.-Q. Yan, A. Kracher, S. T. Hannahs, S. L. Bud'ko, and P. C. Canfield. "Effects of Co substitution on thermodynamic and transport properties and anisotropic H_{c2} in $Ba(Fe_{1-x}Co_x)_2As_2$ single crystals." *Phys. Rev. B*, **78**:214515, Dec 2008.

[Onn11] H Kamerlingh Onnes. "The resistance of pure mercury at helium temperatures." *Commun. Phys. Lab. Univ. Leiden*, **12**(120):1, 1911.

[OOY14] T. Okada, H. Ogino, H. Yakita, A. Yamamoto, K. Kishio, and J. Shimoyama. "Effects of post-annealing and cobalt co-doping on superconducting properties of (Ca,Pr)Fe_2As_2 single crystals." *Physica C: Superconductivity*, **505**:1 – 5, 2014.

[PG10] Johnpierre Paglione and Richard L. Greene. "High-temperature superconductivity in iron-based materials." *Nat Phys*, **6**(9):645–658, 09 2010.

[10.1038/nphys1759.]

[PLW11] Joonbum Park, G. Lee, F. Wolff-Fabris, Y. Y. Koh, M. J. Eom, Y. K. Kim, M. A. Farhan, Y. J. Jo, C. Kim, J. H. Shim, and J. S. Kim. "Anisotropic Dirac Fermions in a Bi Square Net of $SrMnBi_2$." *Phys. Rev. Lett.*, **107**:126402, Sep 2011.

[PMY16] Akiyoshi Park, Akinori Mine, Tatsuhiro Yamada, Fumiaki Ohtake, Hiroki Akiyama, Yue Sun, Sunseng Pyon, Tsuyoshi Tamegai, Yutaka Kitahama, Tasuku Mizukami, Kazutaka Kudo, Minoru Nohara, and Hisashi Kitamura. "Enhancement of critical current density in a$Ca_{0.85}La_{0.15}Fe(As_{0.92}Sb_{0.08})_2$ superconductor with Tc=47 K through 3 MeV proton irradiation." *Superconductor Science and Technology*, **29**(5):055006, 2016.

[PPB09] Dinah R. Parker, Michael J. Pitcher, Peter J. Baker, Isabel Franke, Tom Lancaster, Stephen J. Blundell, and Simon J. Clarke. "Structure, antiferromagnetism and superconductivity of the layered iron arsenide NaFeAs." *Chem. Commun.*, pp. 2189–2191, 2009.

[PPB10] M Putti, I Pallecchi, E Bellingeri, M R Cimberle, M Tropeano, C Ferdeghini, A Palenzona, C Tarantini, A Yamamoto, J Jiang, J Jaroszynski, F Kametani, D Abraimov, A Polyanskii, J D Weiss, E E Hellstrom, A Gurevich, D C Larbalestier, R Jin, B C Sales, A S Sefat, M A McGuire, D Mandrus, P Cheng, Y Jia, H H Wen, S Lee, and C B Eom. "New Fe-based superconductors: properties relevant for applications." *Superconductor Science and Technology*, **23**(3):034003, 2010.

[PTK09] D. K. Pratt, W. Tian, A. Kreyssig, J. L. Zarestky, S. Nandi, N. Ni, S. L. Bud'ko, P. C. Canfield, A. I. Goldman, and R. J. McQueeney. "Coexistence of Competing Antiferromagnetic and Superconducting Phases in the Underdoped $Ba(Fe_{0.953}Co_{0.047})_2As_2$ Compound Using X-ray and Neutron Scattering Techniques." *Phys. Rev. Lett.*, **103**:087001, Aug 2009.

[PVC09] D. Parker, M. G. Vavilov, A. V. Chubukov, and I. I. Mazin. "Coexistence of superconductivity and a spin-density wave in pnictide superconductors: Gap symmetry and nodal lines." *Phys. Rev. B*, **80**:100508, Sep 2009.

[QHB09] M. M. Qazilbash, J. J. Hamlin, R. E. Baumbach, Lijun Zhang, D. J. Singh, M. B. Maple, and D. N. Basov. "Electronic correlations in the iron pnictides." *Nat Phys*, **5**(9):647–650, 09 2009.

[10.1038/nphys1343.]

[RA16] Soumya J. Ray and Lambert Alff. "Superconductivity and Dirac fermions in 112-phase pnictides." *physica status solidi (b)*, pp. n/a–n/a, 2016.

[RAA14] E. P. Rosenthal, E. F. Andrade, C. J. Arguello, R. M. Fernandes, L. Y. Xing, X. C. Wang, C. Q. Jin, A. J. Millis, and A. N. Pasupathy. "Visualization of electron nematicity and unidirectional antiferroic fluctuations at high temperatures in NaFeAs." *Nat Phys*, **10**(3):225–232, 03 2014.

[RBK15] Reiner Retzlaff, Alexander Buckow, Philipp Komissinskiy, Soumya Ray, Stefan Schmidt, Holger Mühlig, Frank Schmidl, Paul Seidel, Jose Kurian, and Lambert Alff. "Superconductivity and role of pnictogen and Fe substitution in 112-$LaPd_xPn_2$ ($Pn = \mathrm{Sb}, \mathrm{Bi}$)." *Phys. Rev. B*, **91**:104519, Mar 2015.

[RCD08] Zhi-An Ren, Guang-Can Che, Xiao-Li Dong, Jie Yang, Wei Lu, Wei Yi, Xiao-Li Shen, Zheng-Cai Li, Li-Ling Sun, Fang Zhou, and Zhong-Xian Zhao. "Superconductivity and phase diagram in iron-based arsenic-oxides $ReFeAsO_\delta$ (Re = rare-earth metal) without fluorine doping." *EPL (Europhysics Letters)*, **83**(1):17002, 2008.

[RGM15] Krishna K. Ramachandran, Clment Genet, and Arthur Mar. "Quaternary rare-earth arsenides $REAg_{1-x}Zn_yAs_2$ (RE=La-Nd, Sm, Gd-Dy) with tetragonal $SrZnBi_2$- and $HfCuSi_2$-type structures." *Journal of Solid State Chemistry*, **231**:204 – 211, 2015.

[RJA15] P F S Rosa, C B R Jesus, C Adriano, Z Fisk, and P G Pagliuso. "The role of Ni vacancies on the physical properties of $CeNi_xBi_{2-y}$ single crystals." *Journal of Physics: Conference Series*, **592**(1):012063, 2015.

[RQL08] S. Raghu, Xiao-Liang Qi, Chao-Xing Liu, D. J. Scalapino, and Shou-Cheng Zhang. "Minimal two-band model of the superconducting iron oxypnictides." *Phys. Rev. B*, **77**:220503, Jun 2008.

[RSS13] E. E. Rodriguez, D. A. Sokolov, C. Stock, M. A. Green, O. Sobolev, Jose A. Rodriguez-Rivera, H. Cao, and A. Daoud-Aladine. "Magnetic and structural properties near the Lifshitz point in $Fe_{1+x}Te$." *Phys. Rev. B*, **88**:165110, Oct 2013.

[RTJ08] Marianne Rotter, Marcus Tegel, and Dirk Johrendt. "Superconductivity at 38 K in the Iron Arsenide $(Ba_{1-x}K_x)Fe_2As_2$." *Phys. Rev. Lett.*, **101**:107006, Sep 2008.

[RYL08a] Z. A. Ren, J. Yang, W. Lu, W. Yi, G. C. Che, X. L. Dong, L. L. Sun, and Z. X. Zhao. "Superconductivity at 52 K in iron based F doped layered quaternary compound $PrO_{1-x}F_xFeAs$." *Materials Research Innovations*, **12**(3):105–106, 2008.

[RYL08b] Zhi-An Ren, Jie Yang, Wei Lu, Wei Yi, Xiao-Li Shen, Zheng-Cai Li, Guang-Can Che, Xiao-Li Dong, Li-Ling Sun, Fang Zhou, and Zhong-Xian Zhao. "Superconductivity in the iron-based F-doped layered quaternary compound $Nd[O_{1-x}F_x]FeAs$." *EPL (Europhysics Letters)*, **82**(5):57002, 2008.

[SAB79] F. Steglich, J. Aarts, C. D. Bredl, W. Lieke, D. Meschede, W. Franz, and H. Schäfer. "Superconductivity in the Presence of Strong Pauli Paramagnetism: $CeCu_2Si_2$." *Phys. Rev. Lett.*, **43**:1892–1896, Dec 1979.

[Sca12] D. J. Scalapino. "A common thread: The pairing interaction for unconventional superconductors." *Rev. Mod. Phys.*, **84**:1383–1417, Oct 2012.

[SCG93] A Schilling, M Cantoni, JD Guo, and HR Ott. "Superconductivity above 130 K in the Hg-Ba-Ca-Cu-O system." *Nature*, **363**(6424):56–58, 1993.

[SCG13a] X. P. Shen, S. D. Chen, Q. Q. Ge, Z. R. Ye, F. Chen, H. C. Xu, S. Y. Tan, X. H. Niu, Q. Fan, B. P. Xie, and D. L. Feng. "Electronic structure of $Ca_{10}(Pt_4As_8)(Fe_{2-x}Pt_xAs_2)_5$ with metallic Pt_4As_8 layers: An angle-resolved photoemission spectroscopy study." *Phys. Rev. B*, **88**:115124, Sep 2013.

[SCG13b] X. P. Shen, S. D. Chen, Q. Q. Ge, Z. R. Ye, F. Chen, H. C. Xu, S. Y. Tan, X. H. Niu, Q. Fan, B. P. Xie, and D. L. Feng. "The unique electronic structure of Ca10(Pt4As8)(Fe2-xPtxAs2)5 with metallic Pt4As8 layers." *Arxiv*, p. 1308.3105, Aug 2013.

[SDB15] Tobias Strzer, Gerald Derondeau, Eva-Maria Bertschler, and Dirk Johrendt. "Superconductivity by rare earth doping in the 1038-type compounds with RE=Y, La-Nd, Sm-Lu." *Solid State Communications*, **201**:36 – 39, 2015.

[SDJ12] Tobias Stürzer, Gerald Derondeau, and Dirk Johrendt. "Role of different negatively charged layers in $Ca_{10}(FeAs)_{10}(Pt_4As_8)$ and superconductivity at 30 K in electron-doped $(Ca_{0.8}La_{0.2})_{10}(FeAs)_{10}(Pt_3As_8)$." *Phys. Rev. B*, **86**:060516, Aug 2012.

[SFC08] C. Senatore, R. Flükiger, M. Cantoni, G. Wu, R. H. Liu, and X. H. Chen. "Upper critical fields well above 100 T for the superconductor $SmFeAsO_{0.85}F_{0.15}$ with $T_c = 46$K." *Phys. Rev. B*, **78**:054514, Aug 2008.

[SFL13] T Strzer, G M Friederichs, H Luetkens, A Amato, H-H Klauss, and Dirk Johrendt. "Structural and magnetic phase transitions in triclinic $Ca_{10}(FeAs)_{10}(Pt_3As_8)$." *Journal of Physics: Condensed Matter*, **25**(12):122203, 2013.

[SH88] Z. Z. Sheng and A. M. Hermann. "Bulk superconductivity at 120 K in the Tl-Ca/Ba-Cu-O system." *Nature*, **332**(6160):138–139, 03 1988.

[10.1038/332138a0.]

[SHK09] J. H. Shim, K. Haule, and G. Kotliar. "Density-functional calculations of the electronic structures and magnetism of the pnictide superconductors $BaFeAs_2$ and $BaFeSb_2$." *Phys. Rev. B*, **79**:060501, Feb 2009.

[SJM08] Athena S. Sefat, Rongying Jin, Michael A. McGuire, Brian C. Sales, David J. Singh, and David Mandrus. "Superconductivity at 22 K in Co-Doped $BaFe_2As_2$ Crystals." *Phys. Rev. Lett.*, **101**:117004, Sep 2008.

[SKB11] Z. Shermadini, A. Krzton-Maziopa, M. Bendele, R. Khasanov, H. Luetkens, K. Conder, E. Pomjakushina, S. Weyeneth, V. Pomjakushin, O. Bossen, and A. Amato. "Coexistence of Magnetism and Superconductivity in the Iron-Based Compound $Cs_{0.8}(FeSe_{0.98})_2$." *Phys. Rev. Lett.*, **106**:117602, Mar 2011.

[SKJ14] Tobias Strzer, Fabian Kessler, and Dirk Johrendt. "Superconductivity by transition metal doping in $Ca_{10}(Fe_{1-x}M_xAs)_{10}(Pt_3As_8)$ (M = Co, Ni, Cu)." *Philosophical Magazine*, **94**(31):3632–3639, 2014.

[SLW12] U. Stockert, N. Leps, L. Wang, G. Behr, S. Wurmehl, B. Büchner, and R. Klingeler. "Pr magnetism and its interplay with the Fe spin-density wave in $PrFeAsO_{1-x}F_x$ (x = 0,0.15)." *Phys. Rev. B*, **86**:144407, Oct 2012.

[SSJ16] Tobias Strzer, Christine Strzer, and Dirk Johrendt. "Iron arsenide superconductors $(CaFeAs)_{10}M_nAs_8$ with metallic interlayers (M=Pt, Pd; n=3, 4)." *physica status solidi (b)*, pp. n/a–n/a, 2016.

[Ste84] G. R. Stewart. "Heavy-fermion systems." *Rev. Mod. Phys.*, **56**:755–787, Oct 1984.

[Ste11] G. R. Stewart. "Superconductivity in iron compounds." *Rev. Mod. Phys.*, **83**:1589–1652, Dec 2011.

[STR14] A. Sapkota, G. S. Tucker, M. Ramazanoglu, W. Tian, N. Ni, R. J. Cava, R. J. McQueeney, A. I. Goldman, and A. Kreyssig. "Lattice distortion and stripelike antiferromagnetic order in $Ca_{10}(Pt_3As_8)(Fe_2As_2)_5$." *Phys. Rev. B*, **90**:100504, Sep 2014.

[SWS10] M Shahbazi, X L Wang, C Shekhar, O N Srivastava, and S X Dou. "Upper critical field, critical current density and thermally activated flux flow in fluorine doped CeFeAsO superconductors." *Superconductor Science and Technology*, **23**(10):105008, 2010.

[SYO14] Alberto Sala, Hiroyuki Yakita, Hiraku Ogino, Tomoyuki Okada, Akiyasu Yamamoto, Kohji Kishio, Shigeyuki Ishida, Akira Iyo, Hiroshi Eisaki, Masaya Fujioka, Yoshihiko Takano, Marina Putti, and Jun ichi Shimoyama. "Synthesis and physical properties of $Ca_{1-x}RE_xFeAs_2$ with RE = La-Gd." *Applied Physics Express*, **7**(7):073102, 2014.

[TBK10] M. A. Tanatar, E. C. Blomberg, A. Kreyssig, M. G. Kim, N. Ni, A. Thaler, S. L. Bud'ko, P. C. Canfield, A. I. Goldman, I. I. Mazin, and R. Prozorov. "Uniaxial-strain mechanical detwinning of $CaFe_2As_2$ and $BaFe_2As_2$ crystals: Optical and transport study." *Phys. Rev. B*, **81**:184508, May 2010.

[TDT13] T. Tamegai, Q.P. Ding, T. Taen, F. Ohtake, H. Inoue, Y. Tsuchiya, S. Mohan, Y. Sun, Y. Nakajima, S. Pyon, and H. Kitamura. "Superconducting properties of ironplatinumarsenides $Ca_{10}(Pt_nAs_8)(Fe_{2-x}Pt_xAs_2)_5$ (n = 3, 4)." *Physica C:*

Superconductivity, **494**:65 – 68, 2013. Proceedings of the 25th International Symposium on Superconductivity (ISS 2012) Advances in Superconductivity {XXV}.

[TIA08a] Hiroki Takahashi, Kazumi Igawa, Kazunobu Arii, Yoichi Kamihara, Masahiro Hirano, and Hideo Hosono. "Superconductivity at 43[thinsp]K in an iron-based layered compound $LaO_{1-x}F_xFeAs$." *Nature*, **453**(7193):376–378, 05 2008.

[10.1038/nature06972.]

[TIA08b] Hiroki Takahashi, Kazumi Igawa, Kazunobu Arii, Yoichi Kamihara, Masahiro Hirano, and Hideo Hosono. "Superconductivity at 43[thinsp]K in an iron-based layered compound $LaO_{1-x}F_xFeAs$." *Nature*, **453**(7193):376–378, 05 2008.

[10.1038/nature06972.]

[TKN09] M. A. Tanatar, A. Kreyssig, S. Nandi, N. Ni, S. L. Bud'ko, P. C. Canfield, A. I. Goldman, and R. Prozorov. "Direct imaging of the structural domains in the iron pnictides AFe_2As_2 ($A = \mathrm{Ca}, \mathrm{Sr}, \mathrm{Ba}$)." *Phys. Rev. B*, **79**:180508, May 2009.

[TNM09] M. A. Tanatar, N. Ni, C. Martin, R. T. Gordon, H. Kim, V. G. Kogan, G. D. Samolyuk, S. L. Bud'ko, P. C. Canfield, and R. Prozorov. "Anisotropy of the iron pnictide superconductor $Ba(Fe_{1-x}Co_x)_2As_2$ ($x = 0.074, T_c = 23\mathrm{K}$)." *Phys. Rev. B*, **79**:094507, Mar 2009.

[TNT11] M. A. Tanatar, N. Ni, A. Thaler, S. L. Bud'ko, P. C. Canfield, and R. Prozorov. "Systematics of the temperature-dependent interplane resistivity in $Ba(Fe_{1-x}M_x)_2As_2$ (M = Co, Rh, Ni, and Pd)." *Phys. Rev. B*, **84**:014519, Jul 2011.

[TSZ13] S. Thirupathaiah, T. Stürzer, V. B. Zabolotnyy, D. Johrendt, B. Büchner, and S. V. Borisenko. "Why T_c of $(CaFeAs)_{10}Pt_{3.58}As_8$ is twice as high as $(CaFe_{0.95}Pt_{0.05}As)_{10}Pt_3As_8$." *Phys. Rev. B*, **88**:140505, Oct 2013.

[TTL08] Joshua H. Tapp, Zhongjia Tang, Bing Lv, Kalyan Sasmal, Bernd Lorenz, Paul C. W. Chu, and Arnold M. Guloy. "LiFeAs: An intrinsic FeAs-based superconductor with $T_c = 18\mathrm{K}$." *Phys. Rev. B*, **78**:060505, Aug 2008.

[TTN09] T. Taen, Y. Tsuchiya, Y. Nakajima, and T. Tamegai. "Superconductivity at $T_c \sim 14\mathrm{K}$ in single-crystalline $FeTe_{0.61}Se_{0.39}$." *Phys. Rev. B*, **80**:092502, Sep 2009.

[Vop15] Melvin M. Vopson. "Fundamentals of Multiferroic Materials and Their Possible Applications." *Critical Reviews in Solid State and Materials Sciences*, **40**(4):223–250, 2015.

[VVC10] A. B. Vorontsov, M. G. Vavilov, and A. V. Chubukov. "Superconductivity and spin-density waves in multiband metals." *Phys. Rev. B*, **81**:174538, May 2010.

[WAT87] Maw-Kuen Wu, Jo R Ashburn, C_J Torng, Ph H Hor, Rl L Meng, Lo Gao, Z J_ Huang, YQ Wang, and aCW Chu. "Superconductivity at 93 K in a new mixed-phase Y-Ba-Cu-O compound system at ambient pressure." *Physical Review Letters*, **58**(9):908, 1987.

[Wen12] Hai-Hu Wen. "Overview on the physics and materials of the new superconductor $K_xFe_{2-y}Se_2$." *Reports on Progress in Physics*, **75**(11):112501, 2012.

[WLC08] Cao Wang, Linjun Li, Shun Chi, Zengwei Zhu, Zhi Ren, Yuke Li, Yuetao Wang, Xiao Lin, Yongkang Luo, Shuai Jiang, Xiangfan Xu, Guanghan Cao, and Zhu'an Xu. "Thorium-dopinginduced superconductivity up to 56K in $Gd_{1-x}Th_x$ FeAsO." *EPL (Europhysics Letters)*, **83**(6):67006, 2008.

[WLL08] X.C. Wang, Q.Q. Liu, Y.X. Lv, W.B. Gao, L.X. Yang, R.C. Yu, F.Y. Li, and C.Q. Jin. "The superconductivity at 18 K in LiFeAs system." *Solid State Communications*, **148**(1112):538 – 540, 2008.

[WLP11] Erwin Wiesenmayer, Hubertus Luetkens, Gwendolyne Pascua, Rustem Khasanov, Alex Amato, Heidi Potts, Benjamin Banusch, Hans-Henning Klauss, and Dirk Johrendt. "Microscopic Coexistence of Superconductivity and Magnetism in $Ba_{1-x}\mathbf{K}_xFe_2As_2$." *Phys. Rev. Lett.*, **107**:237001, Nov 2011.

[WTM15] B.D. White, J.D. Thompson, and M.B. Maple. "Unconventional superconductivity in heavy-fermion compounds." *Physica C: Superconductivity and its Applications*, **514**:246 – 278, 2015. Superconducting Materials: Conventional, Unconventional and Undetermined.

[WYY11] A. F. Wang, J. J. Ying, Y. J. Yan, R. H. Liu, X. G. Luo, Z. Y. Li, X. F. Wang, M. Zhang, G. J. Ye, P. Cheng, Z. J. Xiang, and X. H. Chen. "Superconductivity at 32 K in single-crystalline $Rb_xFe_{2-y}Se_2$." *Phys. Rev. B*, **83**:060512, Feb 2011.

[XLY12] Z. J. Xiang, X. G. Luo, J. J. Ying, X. F. Wang, Y. J. Yan, A. F. Wang, P. Cheng, G. J. Ye, and X. H. Chen. "Transport properties and electronic phase diagram of single-crystalline $\mathbf{Ca_{10}(Pt_3As_8)((Fe_{1-x}Pt_x)_2As_2)_5}$." *Phys. Rev. B*, **85**:224527, Jun 2012.

[XZX15] Xiangzhuo Xing, Wei Zhou, Baozhang Xu, Na Li, Yiran Sun, Yufeng Zhang, and Zhixiang Shi. "Co-co-doping Effect on Superconducting Properties of 112-Type $Ca_{0.8}La_{0.2}FeAs_2$ Single Crystals." *Journal of the Physical Society of Japan*, **84**(7):075001, 2015.

[XZZ16] Xiangzhuo Xing, Wei Zhou, Nan Zhou, Feifei Yuan, Yongqiang Pan, Haijun Zhao, Xiaofeng Xu, and Zhixiang Shi. "Anisotropic GinzburgLandau scaling of H_{c2} and transport properties of 112-type $Ca_{0.8}La_{0.2}Fe_{0.98}Co_{0.02}As_2$ single crystal." *Superconductor Science and Technology*, **29**(5):055005, 2016.

[YLC11] Ming Yi, Donghui Lu, Jiun-Haw Chu, James G. Analytis, Adam P. Sorini, Alexander F. Kemper, Brian Moritz, Sung-Kwan Mo, Rob G. Moore, Makoto Hashimoto, Wei-Sheng Lee, Zahid Hussain, Thomas P. Devereaux, Ian R. Fisher, and Zhi-Xun Shen. "Symmetry-breaking orbital anisotropy observed for detwinned Ba(Fe1-xCox)2As2 above the spin density wave transition." *Proceedings of the National Academy of Sciences*, **108**(17):6878–6883, 2011.

[YOO14] Hiroyuki Yakita, Hiraku Ogino, Tomoyuki Okada, Akiyasu Yamamoto, Kohji Kishio, Tetsuya Tohei, Yuichi Ikuhara, Yoshito Gotoh, Hiroshi Fujihisa, Kunimitsu Kataoka, Hiroshi Eisaki, and Jun-ichi Shimoyama. "A New Layered Iron Arsenide Superconductor: (Ca,Pr)$FeAs_2$." *Journal of the American Chemical Society*, **136**(3):846–849, 2014. PMID: 24387288.

[YOS15a] H. Yakita, H. Ogino, A. Sala, T. Okada, A. Yamamoto, K. Kishio, A. Iyo, H. Eisaki, and J. Shimoyama. "Dependences on {RE} of superconducting properties of transition metal co-doped (Ca, RE)$FeAs_2$ with {RE} = La-Gd." *Physica C: Superconductivity and its Applications*, **518**:14 – 17, 2015. Proceedings of the 27th International Symposium on Superconductivity.

[YOS15b] Hiroyuki Yakita, Hiraku Ogino, Alberto Sala, Tomoyuki Okada, Akiyasu Yamamoto, Kohji Kishio, Akira Iyo, Hiroshi Eisaki, and Jun ichi Shimoyama. "Co and Mn doping effect in polycrystalline (Ca,La) and (Ca,Pr)$FeAs_2$ superconductors." *Superconductor Science and Technology*, **28**(6):065001, 2015.

[YXD16] Run Yang, Bing Xu, Yaomin Dai, Wei Zhang, Jinyun Liu, Ziyang Qiu, and Xianggang Qiu. "Optical study of the antiferromagnetic ordered state in electron-overdoped $Ca_{0.77}Nd_{0.23}FeAs_2$." *Phys. Rev. B*, **93**:245110, Jun 2016.

[YZL14] M. Yi, Y. Zhang, Z. K. Liu, X. Ding, J. H. Chu, A. F. Kemper, N. Plonka, B. Moritz, M. Hashimoto, S. K. Mo, Z. Hussain, T. P. Devereaux, I. R. Fisher, H. H. Wen, Z. X. Shen, and D. H. Lu. "Dynamic competition between spin-density wave order and superconductivity in underdoped $Ba_{1-x}K_xFe_2As_2$." *Nature Communications*, **5**:3711 EP –, 04 2014.

[ZHC08a] Jun Zhao, Q. Huang, Clarina de la Cruz, Shiliang Li, J. W. Lynn, Y. Chen, M. A. Green, G. F. Chen, G. Li, Z. Li, J. L. Luo, N. L. Wang, and Pengcheng Dai. "Structural and magnetic phase diagram of $CeFeAsO_{1-x}F_x$ and its relation to high-temperature superconductivity." *Nat Mater*, **7**(12):953–959, 12 2008.

[10.1038/nmat2315.]

[ZHC08b] Jun Zhao, Q. Huang, Clarina de la Cruz, Shiliang Li, J. W. Lynn, Y. Chen, M. A. Green, G. F. Chen, G. Li, Z. Li, J. L. Luo, N. L. Wang, and Pengcheng Dai. "Structural and magnetic phase diagram of $CeFeAsO_{1-x}F_x$ and its relation to high-temperature superconductivity." *Nat Mater*, **7**(12):953–959, 12 2008.

[10.1038/nmat2315.]

[ZTL13] Qiang Zhang, Wei Tian, Haifeng Li, Jong-Woo Kim, Jiaqiang Yan, R. William McCallum, Thomas A. Lograsso, Jerel L. Zarestky, Sergey L. Bud'ko, Robert J. McQueeney, and David Vaknin. "Magnetic structures and interplay between rare-earth Ce and Fe magnetism in single-crystal CeFeAsO." *Phys. Rev. B*, **88**:174517, Nov 2013.

[ZXZ15] W. Zhou, X. Z. Xing, X. Zhou, M. X. Xu, and Z. X. Shi. "Pressure effect on the superconductivity of $Ca_{1-x}La_xFeAs_2$(x=0.18) single crystal." *EPL (Europhysics Letters)*, **109**(3):37005, 2015.

[ZZY14] Wei Zhou, Jincheng Zhuang, Feifei Yuan, Xiong Li, Xiangzhuo Xing, Yue Sun, and Zhixiang Shi. "Anisotropic superconductivity of $Ca_{1-x}La_xFeAs_2$ (x = 0.18) single crystal." *Applied Physics Express*, **7**(6):063102, 2014.